Methods and tools for the design of RFICs

Tomás Carrasco Carrillo

Tomás Carrasco Carrillo

Methods and tools for the design of RFICs

– A dissertation submitted to the department of Electronics of University of Barcelona in partial fulfillment of the requirements for the degree of doctor of philosophy –

September 22, 2013

Director: Dr. Javier Sieiro Córdoba
Co-Director: Dr. José María López-Villegas

GRAF-Group of Radio Frequency

Universitat de Barcelona

Departament d'Electrònica

Methods and tools for the design of RFICs

Memòria presentada per a optar al títol de Doctor per la Universitat de Barcelona.

Programa de doctorat: Enginyeria de microsistemes, sensors i actuadors
Bienni: 2004-2005

19 de Setembre de 2013

Autor: Tomás Carrasco Carrillo
Director: Dr. Javier Sieiro Córdoba
Co-Director: Dr. José María López-Villegas

En Javier Sieiro i en José M. López-Villegas, professors de la Facultat de Física de la Universitat de Barcelona,

CERTIFIQUEN:

que la memòria "Methods and tools for the design of RFICs", que presenta en Tomás Carrasco Carrillo per optar al grau de Doctor en Enginyeria Electrònica, s'ha realitzat sota la seva direcció.

Dr. Javier Sieiro Córdoba Dr. José María López-Villegas

To my lovely wife Elisabet and my little baby boy Atreyu with all my love

Preface

Radio frequency and microwave technology have reached an unimaginable development and are involved in most of our daily activities. It is a fact that, cell technology holds the fastest grown of any other technology advance ever. To this point, mobility paradigm have been achieved and we have fast internet access from wherever we are in a pocket device. However, there are still milestones ahead.

Most likely, ambient intelligence paradigm is going to focus the next advances in wireless technologies. Beside, developments of information technology never had the explicit goal of changing society, but rather did so as a side effect, the ambient intelligence visions expressly proposes to transform society by fully connecting and computerizing it. Hence, the increasing demand on radio frequency (RF) devices and applications represents, not only a challenge for technological industries to improve its roadmaps, but also for RF engineers to design faster and more robust, low-power, small-size and low-cost devices.

Regarding to communication robustness, in the latest years, differential topologies have acquired an important relevance because of its natural noise and interference immunity. Within this framework, a differential n-port device can still be treated as a *2nx2n* device and classical analysis circuit theory (i.e. quadripole theory) can be applied by means of Z-,Y-, h-parameters or the most suitable S-parameters in the radio frequency field. Despite of it, Bockelman and Eisenstadt introduced the mixed-mode scattering parameters, which more properly express the differential and common-mode behavior of symmetrical devices and make faster the design process of these devices. However, since Bockelman and Eisenstadt introduced the mixed-mode scattering parameters, they have been used with a varying degree of success, as it will be shown, mainly because of a misinterpretation.

Thereby, Part I of this thesis is devoted to extend the theory of mixed-mode scattering parameters and proposes the methodology to analyze such devices. For this proposal, in Chapter 2, the simplest case of a two-port device is developed. By solving this simple case, most of the lacks of the current theory are filled up. As instance, it allows the characterization and comparison of symmetric and spiral inductors, which have remained a controversy point until now. Furthermore, the power dissipated on a two-port device, when it is seen as a symmetric load, is reviewed, showing

interesting properties of this kind of devices. After solving this case, Chapter 3 extends the theory to a n-port device. Thereby, generalized S-parameters are used to obtain a new expression for the input reflection coefficient of a n-port device. Moreover, power match theory is extended to multiple-port devices showing that there exist a duality between standard S-parameters and mixed-mode S-parameters but at the same time, there are important differences that have to be taken into account in a fine design.

Another key point on the fast and inexpensive development of radio frequency devices is the advance on fast CAD tools for the analysis and synthesis of passive devices, specially inductors. These devices frequently appear in radio frequency design because of its versatility. Even though, there have been multiple attempts to replace them with external components or even active circuits, in the case of silicon technologies, planar inductors are the most popular shapes because of its integrability. However, the design of inductors entails a deep experience and acknowledge not only on the behavior of such devices but on the use of electromagnetic (EM) simulators. Unfortunately, the use of EM simulators consumes an important quantity of time and resources. Thus, the synthesis of inductors represents an important drawback. Thereby, Part II of this thesis is devoted to improve some of the aspects that slow down the synthesis process of inductors. Therefore, in Chapter 4, an 'ab initio' technique for the meshing of planar radio frequency and microwave circuits is described. It is based on the analytic study of the current crowding phenomena that takes place inside the component. In such evaluation, it is not required an explicit solution of currents and charges at any part of the circuit. Then, the number of mesh cells assigned to a given metal strip depends on the value initially obtained from the analytic study. The technique presented can evaluate the losses in the component with a high accuracy just in few seconds where an electromagnetic simulator would normally last hours.

Likewise, in Chapter 5 a simple bisection algorithm for the synthesis of compact planar inductors is presented. It is based on a set of heuristic rules obtained from the study of the electromagnetic behavior of these planar devices. Thereby, the number of iterations is kept moderately low. Moreover, in order to speed up analysis at each step, a fast planar electromagnetic solver is used which is based, once again, on the knowledge of the synthesized component.

Additionally, in Chapter 6 the mixed-mode S-parameter methodology proposed and the CAD tools introduced are extensively used in the design of a single-ended to differential low noise amplifier (LNA) in a standard 0.35μm CMOS technology. Low noise amplifier is one of the key components because it tends to dominate the sensitivity and noise figure (NF) of the whole system. Moreover, device performances are directly related to both active and passive components available in a given technology. Thus, the chosen technology and the quality factor of passives will have a high impact on the main figures of merit of the actual circuit.

Gelida, *Tomas Carrasco*
June 2013

Resum

L'enginyeria de radiofreqüència i la tecnologia de microones han assolit un desenvolupament inimaginable i avui en dia formen part de la majoria de les nostres activitats diàries. Probablement, la tecnologia mòbil ha tingut un desenvolupament més ràpid que qualsevol altre avenç tecnològic de l'era digital. Avui en dia, podem dir que el paradigma de la mobilitat s'ha assolit i tenim accés ràpid a internet des de qualsevol lloc on podem estar amb un dispositiu de butxaca. No obstant això, encara hi ha fites per endavant.

Es més que probable que el paradigma de l''ambient intelligence' sigui el centre dels pròxims avenços en les tecnologies sense fils. A diferencia del paradigma de l''ambient intelligence', l'evolució de la tecnologia de la informació mai ha tingut l'objectiu explícit de canviar la societat, sinó que ho van fer com un efecte secundari, en canvi, les visions d''ambient intelligence' proposen expressament el transformar la societat mitjançant la connexió completa i la informatització d'ella. Per tant, l'augment de la demanda de dispositius de ràdio freqüència (RF) i de les seves possibles aplicacions representa, no només un repte per a les indústries tecnològiques per millorar els seus plans de treball, sinó també per als enginyers de RF que hauran de dissenyar dispositius de baixa potència, més robusts, de mida petita i de baix cost.

Quant a la robustesa dels dispositius, en els últims anys, les topologies de tipus diferencial han adquirit una important rellevància per la seva immunitat natural al soroll i resistència a les interferències. Dins d'aquest marc, un dispositiu de n-ports diferencial, encara pot ser tractat com un dispositiu 2nx2n i la teoria clàssica d'anàlisi de circuits (és a dir, la teoria de quadripols) es pot aplicar a través de paràmetres Z, Y, h o els paràmetres S, més adequats en el camp de freqüència de ràdio. Tot i això, Bockelman i Eisenstadt introdueixen els paràmetres S mixtos, que expressen més adequadament el comportament diferencial i en mode comú de dispositius simètrics o asimètrics. Des de llavors, aquests paràmetres s'han utilitzat amb un grau variable d'èxit, com es mostrarà, principalment a causa d'una mala interpretació.

D'aquesta manera, la primera part d'aquesta tesi està dedicada a estendre la teoria dels paràmetres S de mode mixt i proposa la metodologia d'anàlisi d'aquest

tipus de dispositius i circuits. D'aquesta forma, en el Capítol 2, es desenvolupa el cas més simple d'un dispositiu de dos ports. En resoldre aquest cas simple, la major part de les mancances de la teoria actual es posen de relleu. Com a exemple, permet la caracterització i la comparació de bobines simètriques i espiral no simètriques, que han estat un punt de controvèrsia fins ara. Després de resoldre aquest cas, al Capítol 3 s'estén la teoria a un dispositiu de n-ports dels quals un nombre pot ser single-ended i la resta diferencials. És en aquest moment quan la dualitat existent entre els paràmetres S estàndard i de mode mixt es pot veure clarament i es destaca en el seu conjunt. Aquesta teoria permet, tanmateix, estendre la teoria clàssica d'amplificadors quan s'analitzen per mitjà de paràmetres S.

Un altre punt clau en el desenvolupament ràpid i de baix cost dels dispositius de radiofreqüència és l'avenç en les eines CAD ràpides per a l'anàlisi i síntesi dels dispositius passius, en especial dels inductors. Aquests dispositius apareixen tot sovint en el disseny de radio freqüència degut a la seva gran versatilitat. Tot i que hi ha hagut múltiples intents de reemplaçar amb components externs o circuits, fins i tot actius, en el cas de les tecnologies de silici, els inductors planars s'han convertit en les formes més populars per la seva integrabilitat. No obstant això, el disseny d'inductors implica conèixer i posseir una experiència profunda no només en el comportament d'aquests dispositius, però també en l'ús de simuladors electromagnètics (EM). Desafortunadament, l'ús dels simuladors EM consumeix una quantitat important de temps i recursos. Per tant, la síntesi dels inductors representa un important inconvenient actualment. D'aquesta manera, la segona part d'aquesta tesi està dedicada a millorar alguns dels aspectes que frenen el procés de síntesi dels inductors. Per tant, en el Capítol 4, es descriu una tècnica 'ab initio' de generació de la malla per bobines planars en ràdio freqüència i microones. La tècnica es basa en l'estudi analític dels fenòmens d'aglomeració de corrent que tenen lloc a l'interior del component. En aquesta avaluació, no es requereix una solució explícita dels corrents i de les càrregues arreu del circuit. Llavors, el nombre de cel·les de la malla assignades a una tira de metall donada, depèn del valor inicialment obtingut a partir de l'estudi analític. La tècnica presentada pot avaluar les pèrdues en el component amb una gran precisió només en uns pocs segons, quan comparat amb un simulador electromagnètic normalment es necessitaria hores.

De la mateixa manera, en el Capítol 5 es presenta un senzill algoritme de bisecció per a la síntesi d'inductors planars compactes. Es basa en un conjunt de regles heurístiques obtingut a partir de l'estudi del comportament electromagnètic d'aquests dispositius planars. D'aquesta manera, el nombre d'iteracions es manté moderadament baix. D'altra banda, per tal d'accelerar l'anàlisi en cada pas, s'utilitza un simulador ràpid electromagnètic planar, el qual es basa en el coneixement que es té del component sintetitzat.

Finalment, en el Capítol 6, la metodologia de paràmetres S de mode mixt proposada i les eines CAD introduides s'utilitzen àmpliament en el disseny d'un amplificador de baix soroll single-ended a diferencial (LNA), mitjançant una tecnologia estàndard 0.35µm CMOS. L'amplificador de baix soroll és un dels components claus en un sistema de recepció de radio freqüència, ja que tendeix a dominar la sensibilitat i la figura de soroll (NF) de tot el sistema. D'altra banda, les característiques

d'aquest circuit estan directament relacionades amb els components actius i passius disponibles en una tecnologia donada. Per tant, la tecnologia escollida, el factor de qualitat dels passius, i la forma com es caracteritzen tindran un alt impacte en les principals figures de mèrit del circuit real.

Gelida, *Tomas Carrasco*
June 2013

Contents

Chapter 1
Introduction

1.1 Today's wireless world

Since at nineties the information age started, the digital revolution has changed our lives. Whether we work online, study, pay bills or simply stay in touch with friends and family, a fast internet connection is now seen, by most of the population, as an essential utility, as indispensable as electricity, gas or water. Nearly a quarter of the world's 6.8 billion people use the Internet daily[1]. There is not doubt that, the fast development of the radio frequency communication systems in the last years has played an important role in the Internet popularization, mainly through the commercialization of wireless products as 802.11a, 802.11b, 802.11g, or 802.11n, collectively known as WiFi, or 802.11h, 802.11j and WiMax. Today, a fast internet wireless access at home, or public places as libraries, coffee shops or even in our cities' parks and landscapes has become more than a social request, but a right.

Simultaneously to the Internet development, or maybe because of it, cell technology has reached similar impressive numbers. Thus, the GSM Association estimates that global system for mobile (GSM) communications has more than 2 billion users in 213 different countries; that's just over 30 per cent of the world's population[2]. Hence, taking into account that the universal mobile telecommunications system (UMTS) has reached up to 4.1 billion mobile subscriptions, it is estimated that 6 in 10 of the world's population log in either networks daily. Therefore, this worldwide spread of cell network and the improvement of phone capabilities, mainly through the smart phones technology, has lead the digital era to achieve the connectivity and mobility paradigm, a far milestone not too long ago. Unquestionably, the functioning of information society is nowadays unthinkable without the use of the Internet and the wireless technologies; just as the bridges, roads and railways built in the 19th century were the columns of the industrial revolution, that helped to the overall society to achieve a welfare state.

[1] http://www.guardian.co.uk/technology/2009/mar/03/mobile-phones1

[2] Source: http://www.gsmworld.com/

Within this framework, the expectation are that in the closest future, the Internet and radio frequency system merge into a unique system, able to provide access and exchange of higher amount of information, processing and mobility with no roughness. Thus, the latest cell standard, LTE, is anticipated to become the first truly global mobile phone standard able to reach high capacity and speed by using new digital signal processing (DSP) techniques and modulations. In a few numbers, LTE specification provides downlink peak rates of 300 Mbit/s, uplink peak rates of 75 Mbit/s; and Quality of Service (QoS) provisions permitting a transfer latency of less than 5 ms in the radio access network. Moreover, it has the ability to manage fast-moving mobiles and supports multi-cast and broadcast streams by means of supporting scalable carrier bandwidths, from 1.4 MHz to 20 MHz and in both, frequency division duplexing (FDD) and time-division duplexing (TDD) codifications. With such numbers, we will be able to keep a high definition video conference wherever we are, or even watch a high definition movie streamed from the Internet while we are commuting in a high speed train.

However, either WiFi or Cell technology are not the only examples in wireless technology development. Today, the acceptance of Bluetooth in the short-range communications domain (typically between 1 m and 10 m) is more than evident. Data transfer between our desktop or laptop and its peripherals, our cell phone, or our digital camera, are clear examples of the popularization of this technology. Likewise, the emergent ZigBee, Wibree or Ultra Wide Band (UWB) radio, based on the new standards of the IEEE802.15 family, or RuBee in IEEE standard 1902.1, complete and/or complement Bluetooth. Thus, all them conform the current WPANs which are characterized for being low power, small size and low cost; whereas are capable to satisfy the increasing demand of high bit data transfer.

But further of these technical characteristics, devices within those standards have one more important quality: they are mostly out of the portfolio of the biggest chipset companies as Qualcomm, Broadcom or Samsung which are, actually, more focused on cell. The main reason is because of its characteristics which make the design and development of such devices affordable for small companies. As instance, the fact that they have to be low cost, translates in that they might be integrated in low cost platforms, far away from the latest 28 or 22 nm process used in the latest smart phones. Likewise, low-power and small size lead to the simplification of their architectures and either modulation or codification; also doable thanks to their short range capabilities which drive to an specs relaxation. Thereby, as instance, Europe's Imec research group plans to produce before the end of the year a short range RF transceiver ten times more power efficient than today's Bluetooth and Zigbee chips. Imec's prototype is capable of sending 1024 Kbytes/second over five meters while consuming less than one milliwatt. But there are much more examples of companies which are doing well despite the current economy recession as Green Peak or Telegesis for mention some European small companies. Therefore, we could look forward that investment now in the information and communications industries, even in small or middle-size companies, can underpin our emergence from our today reces-

sion to a recovered new enhanced global economy[3]. In fact, the current small-size low-cost devices' market is just the tip of the iceberg of an upwelling huge market. Since, the coexistence and interconnection between WLAN's, WPAN's and the cell network, which configure our present wireless world, is just the first step towards the implementation of the so-called ambient intelligence (AmI), that it is called to be the next milestone in the information era.

1.2 The AmI paradigm and the future's wireless world

At the time of starting this thesis, by the end of 2004, the target milestone in the wireless technology roadmap was the mobility paradigm. At that moment, cell technology was widely extended, but without enough data rate speed and device capabilities to allow internet connection. To be honest, some feature phones were able to have limited web access meanwhile, personal digital assistant (PDA) were the closer device to what we know as a smart phone. In fact, the earlier smart phone simply included PDA performances till became a truly portable-multi-use PC, by adding the functionality of portable media players, low-end compact digital cameras, pocket video cameras, GPS navigation units and so on. Thus, the current status was unimaginable for most of the people. Perhaps, because the first smart phones as the iPhone, BlackBerry or others appeared one or two years before the economic crisis, around 2006 and 2007 (and of course, they had an awesome acceptance), the smart phone development has not struggled with the economic recession. In spite of it, phone market has kept growing, not only in device technology also in multimedia applications and other gadgets associated to them. Such is the impact of smart phone technology that wireless roadmap has been driven towards the growth of connectivity, multimedia capabilities and pursuit of new applications.

The smart phone development contrasts with the ambient intelligence paradigm or its incipient personal or body area networking (BAN). Despite the fact that AmI was originally thought in the late 90s for the time frame 2010-2020, and it was a clear milestone with the special recognition of the European Commission as a research directive for the IST 6th Framework, most of the scenarios which were presented by Eli Zelkha[4] and Brian Epstein (who coined the name 'ambient intelligence') are far of becoming a reality. The reasons for this slower development might be either the crisis and the fast smart phone market's development or the huge number of consideration to be handle which comprehend from technical, technological and computational-related to social and ethics. This statement can be hold by scraping in what a forthcoming AmI's scenario can be and comparing with what we can find today in either WPAN or BANs networks:

---

[3] In Spain, unemployment has raised up to 26%. It is a challenge and a social duty, we do one's utmost as scientists and engineers. http://www.usatoday.com/money/world/2010-04-30-spain-unemployment_N.htm

[4] In 1998 the board of management of Philips commissioned a series of presentations and internal workshops, organized by Eli Zelkha and Brian Epstein of Palo Alto Ventures

Elisabet goes into her car, when the car recognizes her and adjusts the seat and wheel accordingly to her preferences. Also temperature is settle based on her body temperature measured by a device in Elisabet's smart clothes. The radio seeks her preferred programs and volume is loud in based on the road noise. Meanwhile, the best direction is tracked based on intercommunicated network formed by other cars and surveillance cameras which communicate traffic status in real time. The windshield gets dark when it detects sun brightness can impair the driving conditions but only in that zone she looks at thanks to eyes recognition. At the same time she's commuting, at her office everything temperature, light, her computer turn on and every thing gets ready since the sensor network she is surrounded can communicate her direction, position and time in to arrive. All that happens without any interaction in an intelligent and transparent way.

Without doubt, we can recognize some of this technology advances in our daily life. As instance, in automotive field, some cars incorporate collision detectors which can stop the car without mediation if there's any risk of hitting and object at car's rear. Likewise, in domotic market, it is possible to find some examples of intelligent appliances. However, it is more than evident that we are far from the described example, since AmI paradigm is precisely devised to transform the high-volume consumer electronic industry from the current "fragmented with features" world into a homogeneous network. Thereby, in a real AmI world, user-friendly devices have to support *Ubiquitous* information, communication and entertainment; since, we will be surrounded by a huge amount of interconnected embedded systems of different kind, complexity and functionality. Moreover, it will concern to electronic environments which are sensitive and responsive to the presence of people in a *Transparent* way. Thus, technology will disappear into user's surrounding and interfaces will vanish in a new more friendly human-centric computer interaction. Finally, everything is orchestrated *Intelligently* because technology will be adaptive to the user and autonomously acting.

Therefore, AmI is not just only a vision in the future of a new information interchange scenario, it implies a massive consume of electronics, telecommunications and computing. Then, the primary source of information of the AmI world will be associated with low data rate communication systems, combined with sensors of different kind (temperature, pressure, light, speed, vibration). Therefore, the largest demand on technology innovation would be associated to low cost systems affordable for many companies of different sizes and target product (from purely design of wireless devices to sensors, energy harvesting devices, or software development or applications). Thereby, it is most than likely that this massive consume of electronics become one of the mainstays of the future economy.

However, the development of the AmI paradigm requires a massive and integrated research effort. Those consideration comprehend from technical, technological and computational-related to social and ethics. Regarding to the technical attempts, AmI implies challenges in the sensor development field, biometry science, radio frequency engineering, microchip implanting technology, affective computing, nanotechnology and a long list of specialties. Looking into a AmI front-end, they are mainly related to low data rate and short distance communication systems. Moreover, these devices have to be embedded in clothes, appliances, building materials and so on, and have to last for years. Therefore, concerning to RF design,

challenges are ridden to the high integrability by using cheap technologies and low-power, small-size and robust systems. Furthermore, the improvement of the design current tools (i.e. by obtaining faster automatic tools), is expected to have implications by shorting the time-to-market and actually making cheaper the design process. Thereby, the design of RF circuits still have a series of bottlenecks.

1.3 RF design bottleneck

Radio frequency design, in all its parcels, has quickly moved forward since Prof. Razavi, in his well-known referenced book *'RF microelectronics'* published in 1998, pointed out some of the reasons why this discipline was the bottleneck in the design of a complete system. Even though the numerous advances, it still remains as the bottleneck, and the limitations can still be split in the same three points.

Multidisciplinary field. Radio frequency design sill requires a wide understanding of many areas which are not directly related to integrated circuits. To mention a few of them, an RF designer needs to deal with communication theory, microwave theory, wireless standards, IC design, CAD tools, and so on. In the latest years, most of these areas have been growing in complexity; and gathering the demanded acknowledge in one person, within a reasonable time, is honestly very difficult to achieve. Thereby, a design process is commonly carried out by a team where each member is specialized in a design topic. Despite of this fact, a designer still needs to deal with most of the issues, in order to have a good interaction and reduce time-to-market which is getting shorter day after day. Thus, the current multidisciplinarity is, most likely, the responsible that well established methods or theories are incorrectly used, because of some wrong assumptions. As instance, as it will be shown later, some of the aspects of the mixed-mode S-parameter theory are commonly misunderstood; even though, it is seen as a well-establish theory since the early 90s and it is frequently used in radio frequency and microwave design. Thus, part of this thesis is tend to clarify some of these aspects and extend the existing theory of mixed-mode S-parameters. Likewise, some expressions which are directly derived from the existing mixed-mode S-parameters theory, as instance the quality factor (Q), of an inductor needs to be re-defined.

Design tools. Computer-aided tools have reached a good maturity in most of the fields needed for RF design. Thereby, circuit simulators can solve circuits in time, frequency, and mixed time-frequency domain. These circuits can be formed by lumped devices modeled in BSIM, Mextram, or others device models; or even include continuous devices represented, as instance, by an S-parameter matrix obtained from an electromagnetic simulator. Once, circuit performances are optimum, layout parasitics can be added; commonly obtained from partial element equivalent circuits (PEEC) methods. In the case of a system in package (SiP) implementation, it is also possible to add the wire-bonding or ball array and the encapsulate models to the whole block, achieving a very high reliability simulation results. Of course, this

reliability is only possible if the whole process has been previously characterized and simulation have been compared with actual measurements.

Nowadays most of the work in CAD tools is related with improving simulator speed, the integration of all the requested tools in a most friendly environment and the development of templates which speed up the design process in order to achieve time-to-market requirement. Regarding to simulation speed, perhaps the most important bottlenecks comes from inductors synthesis. Inductors frequently appear in RF design where can perform different function such us high frequency signal blocking, impedance matching transformation, or common-mode to differential transformation. Since, in an integrated technology, these components are commonly embedded on the substrate and its design is performed with the aid of planar 2.5D or even full-wave electromagnetic solvers as MoMentum, HFSS or XFDTD, to mention few of the most popular tools. Independently of the used method, simulation time depends on the component size, complexity of the technology description such us number of oxides and metal layers, the mesh of the structure and of course, the number of frequency points; then, a simulation can last from few hours to days. Thereby, it is fundamental to obtain mechanisms in order to reduce the simulation time. Thus, the second part of this thesis deals with this problem and proposes an 'ab initio adaptive meshing' and a synthesis algorithm to obtain planar inductors in a very short time.

RF hexagon. Most of the RF circuits and systems commonly used in radio frequency implies a trade-off between different parameters as noise, power, linearity, frequency, and so on. Razavi represented the relation between these parameters by an hexagon like in Fig. 1.1. Thus, this trade-off makes RF design a discipline where designer's experience and CAD tools capabilities are fundamental in order to obtain the desired performances. Thus, in order to relieve designer work, it is very important to have well establish methods and theories. Once those methods are well establish, design parameters can be re-defined and introduced in CAD tools as templates.

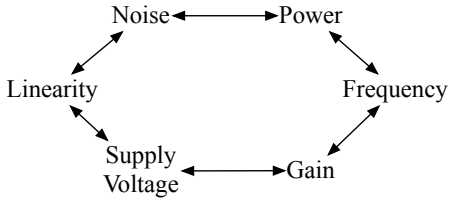

Fig. 1.1 RF design hexagon.

All the exposed bottlenecks are commonly faced by RF designers even in the easiest cases. Thus, in the next point, a low noise amplifier is designed as a demonstrator of all the considerations exposed. A low noise amplifier is one of the basics circuits in a radio frequency system and will be used again in the last chapter.

1.4 Design of a LNA using embedded passives and low-cost substrates

With the increasing speed of digital and mixed-signal circuits, working frequencies have been pushed within the GHz region. The design of devices and circuits in this frequency range entails different challenges which are commonly dismissed at lower frequencies. As instance, high speed propagation leads to large delays, the existence of stationary power waves if strips are not correctly matched, magnetic coupling between strips or considerable substrate losses. Thus, it is necessary to have a deep knowledge of the technology employed and substrate properties (i.e. dielectric constant, loss tangent, substrate and metal conductivity), in order to evaluate the correct signal propagation, coupling or substrate losses. In the case of PCBs technologies, the laminate substrate FR4 is normally the preferred material for being low-cost and a widespread circuit support. However, because FR4 is mainly used for low frequency porpoises, data from manufacturers[5] are commonly provided up to tens of MHz or in the best of the cases up to low hundreds. Thereby, in the last years, there has been an increasing interest on the behavior of FR4 in high frequency applications [1, 2]. As a result, many studies point out the viability of these materials and account the typical relative permittivity ε_r about 4.5, meanwhile $\tan\delta$ can reach 0.02 at 1 GHz. However, these values can vary considerably from different manufacturers, meaning that prior to the design of an RF circuit in FR4, it is necessary to establish a methodology for the correct characterization of the substrate.

Furthermore, a substrate can be more than a bare support; since the integration of a complete RF system on a chip (SoC) is still difficult, the most appealing solution is to integrate part of the system inside the package (SiP)[3]. This implementation allows to embed some of the passive components on the package substrate, and this concept can be translated to a PCB implementation. Thus, the required capacitors, inductors and transformers can be implemented within the PCB layout, allowing a cost reduction in terms of components. However, compared to the traditional hybrid implementation, the designer must also have a very good knowledge on electromagnetic simulators. As if this weren't enough, an RF designer need to embrace a deep handling on circuit theory, electromagnetism, device modeling, advanced circuit simulation tools, signal processing and so on.

At this point, by means of the simple design example detailed in this section, we'll evidence the variate of skills needed in RF design by the description of a whole design process that can be extrapolated to any other technology i.e. ICs technologies, and we will be able to highlight some of the existing problems a designer has to face with. Also, it is useful to state some of the fundamental theory, specifically, in the design of low noise amplifiers which will be used in later chapters. Thus, in this section, we explore the characterization of a FR4 substrate to be used in RF applications and the performance of embedded passives and some of the drawbacks in electromagnetic simulation; through the design, fabrication and measurement of

[5] `http://www.p-m-services.co.uk/fr4_data_sheet.htm`

a low noise amplifier working in the 868 MHz ISM band. The LNA specs has a gain of 9.7 dB and a noise figure of 2.2 dB while driving 2 mA from a 3 V power supply.

1.4.1 Characterization of a FR4 substrate for RF applications

There exist different methods for the characterization of laminate substrates. Those methods are normally based on the indirect measure of a characteristic which depends on the desired substrate physic parameter. As instance, the measure of the resonant modes in a cavity depends on the substrate permittivity[4], likewise, the capacitance of two parallel plates embracing the substrate[5], or the attenuation and delay in a wave-guide[6]. In this work, a transmission line based procedure has been chosen, since the advantage of this method is its simplicity and inexpensiveness. The method is divided in two steps. First, a set of 50Ω transmission line (TL) is fabricated by using the same PCB that one wants to characterize. To synthesis the TLs, the tool Linecalc[6] from Agilent has been used. This tool can synthesize different kinds of TLs as microstrip lines (MLIN), coplanar wave guides (CPW), to mention a couple of them. Since this tool uses equation-based models, one has to introduce an initial relative permittivity, loss tangent and desired delay. The initial parameters can be those provided by the manufacturer, even though they are not valid for such frequencies. By the way, the delay is chosen in order to obtain a feasible line, meanwhile width and gap length is given by the tool in order to match 50Ω. The two transmission lines represented in Fig. 1.2 have been designed following those points and its dimensions are listed in Table 1.1.

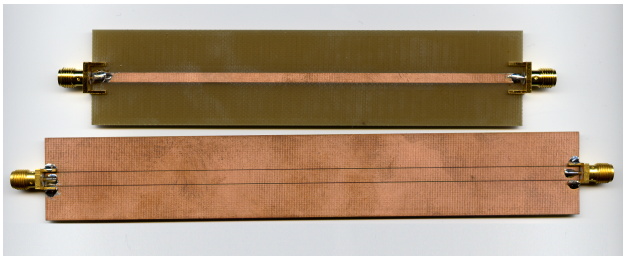

Fig. 1.2 A microstrip line and a coplanar wave guide from top to down, designed on a FR4-PCB.

Second, the TLs are measured with a vector network analyzer. It is important to correctly deembed the extra delay introduced by the connectors. Due to the fact that ε and $tan\delta$ used in the syntheses process, are not the correct for a given frequency, the captured characteristic impedance and phase are different from the synthesized one. Therefore, a validation step is required. In this last step, Linecalc is used as an

[6] Linecalc is a tool incorporated in Advanced Design System (ADS) from Agilent EEsof EDA Design Software.

Table 1.1 Physical dimensions of the implemented TLs.

	Width (mm)	Length (mm)	Gap (mm)
MLIN	2.86	13.45	n.a.
CPW	4.00	16.63	0.23

analysis tool, where permittivity and loss tangent are swept until the attenuation and phase match with the measured data at the same frequency. This process is repeated for each frequency. Fig. 1.3 shows the dependence of the relative permittivity and loss tangent versus frequency in the left and right y-axe, respectively. Notice that the permittivity drops from 4.6 at 100 MHz up to 4.3 at 3 GHz, whereas the loss tangent is quite constant. The results are consistent with the reported in [1].

With the obtained data, a substrate definition file can be set for being used in an electromagnetic simulator as Momentum, also included in ADS. As a verification, the implemented microstrip line is electromagnetically simulated and compared with the previous measurements, Fig. 1.4 shows how simulated phase overlaps the measured around 1 GHz. However, Momentum doesn't allow to introduce frequency dependency in substrate parameters, thus simulation diverges from measures as far frequency rises. Despite this fact, Momentum shows a good agreement with the measurements once the substrate is correctly calibrated. Nevertheless, an accurate description of the substrate is not enough, and it will be shown later that a correct meshing of the simulated structure is equally important.

Similarly, the design on a silicon technology requires an accurate description of the substrate. Therefore, parameters such as thickness, number of layers, permittivity, loss tangent or conductivity has to be precisely introduced in order to assure an accurate result. Fortunately, most of the foundries provide these data. However, the latest silicon technologies are stacked up in too many thin layers; thus, it is very convenient to simplify the number of layers in order to reduce the simulation resources. Therefore, it is a common practice to include some standard structures and passive devices in each tape out to verify the actual results.

As well as in silicon technologies, a FR4 substrate can be used to hold embedded passives as inductors, transformers or capacitors. The synthesis problem is similar in both media, thereby this exercise helps to calibrate the synthesis tool in a fast an cheap way.

1.4.2 Embedded inductors

Inductors are essential components in the implementation of RF circuits. Their frequency response make them useful for different purposes as matching, AC choke or frequency selection. In a hybrid implementation, they are fabricated by means

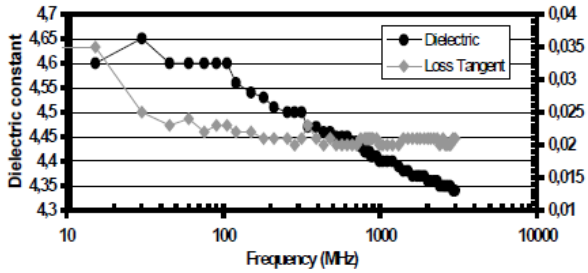

Fig. 1.3 Characterized dielectric constant and loss tangent of a FR4 PCB at high frequency range.

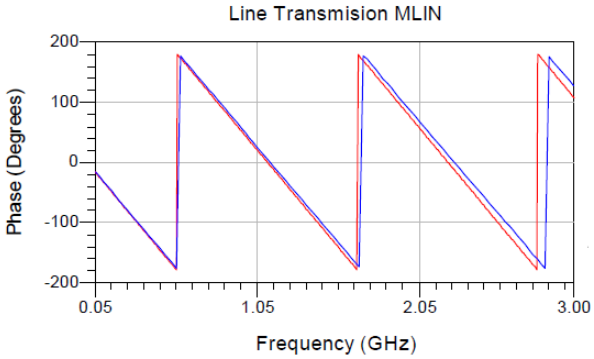

Fig. 1.4 Microstrip TL phase, momentum simulation in blue and VNA measurement in red.

of transmission line sections or by lumped components. Choosing between the two solution depends on the working frequency and the required performance of the system. The main advantages of using discrete components is the reduced size and simplicity. However, the total cost of the solution increases. In a transmission line methodology, a low insertion loss, and a cost reduction in terms of decreasing the amount of discrete components, are the main advantages, but at the expenses of a larger amount of area. In between both approaches, it is also possible to embed square inductors in the substrate as it is extensible done in RFIC circuits. However, this implementation is only possible if the laminate substrate has reasonable RF performances and it is well characterized. Thus, this solution becomes optimum when both a compact size and low cost is required. However, it has an important drawback: there are no scalable models or synthesis tools for such components. Therefore, the design of inductors is commonly done with the aid of electromagnetic simulators.

As it has been already mentioned, the use of electromagnetic simulators requires a good acknowledge in electromagnetism, internal functionality of the tool, and for most of the geometries it requires long simulation time. These facts make the design of inductors a bottleneck in a design process. Thereby, it is worth finding ways to reduce the simulation time. One of the ways is to reduce the meshing size. Most

of the latest versions of EM simulators use an iterative meshing method where, in a first step, the geometry is quasi-static solved. Afterwards, the mesh is iteratively refined by reducing or increasing the number of cells locally, and analyzing the problem again after every iteration[7] . The loop ends when a error function is within the desired range. Assuming an $\mathcal{O}\left(N^2\right)$ solution time for planar solvers, being N the number of cells, the benefits of a meshing reduction are clear. Furthermore, if the mesh is solved without having to analyze the problem in every iteration, the total time reduction, in the use of EM simulators, can be really important. Thus, a new *'ab initio adaptive'* meshing method is introduced in Chapter 4 and it is also used in a new synthesis tool introduce in Chapter 5. Nevertheless, by means of the example treated in this section, it is possible to highlight the importance of the correct definition of the simulation set up. Thereby, with this last aim and the purpose of showing the viability of embedding passive devices in a RF4 substrate, the three inductors shown in Fig. 1.5 have been designed and fabricated.

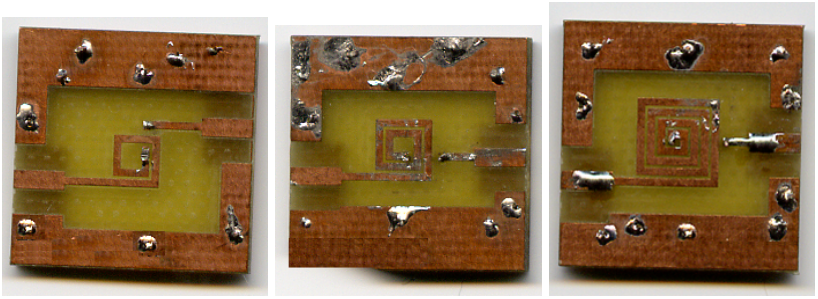

Fig. 1.5 From left to right a 21 nH, 31 nH and 60 nH square inductors silk-screened on a FR4 substrate.

Due to the relative large width of the metal strips compared to the working frequency, a fine mesh is required to compute correctly the losses of the inductor. Fig. 1.6 shows one of the introduced inductors and two different mesh solutions obtained with Momentum. The left hand inductor has been meshed with seven cells/λ; and also, a transmission line approximation has been used to reduce the simulation time. As it can be notice from Fig. 1.6, seven longitudinal cells appear distributed along the device edges. However, the edge mesh option, integrated in Momentum, has not been selected for this case. The quality factor of this inductor is calculated by means of (1.1) and (1.2), when the port on the right side is connected to ground; and the resultant value of Q is represented in magenta in Fig. 1.7. In contrast, the right hand inductor has been meshed with the same number of cells, but selecting the option edge mesh. Therefore, the losses due to eddy currents, in the edges of the metal strips, are more accurately calculated and Q drops about a 20%, as it is repre-

[7] A key benefit of HFSS from Ansys is its automatic adaptive meshing technique. The meshing process uses a highly robust volumetric meshing technique. This technology eliminates the complexity of building and refining a finite element mesh.

sented in turquoise in Fig. 1.7. Additionally, an extreme wrong result is represented in blue, and corresponds to the case when a unique-cell is used to mesh.

One can perceive that, the design of inductors is mostly based on designer ability and skills since, there are no tools that can automatically synthesize an inductor with enough accuracy.

$$Q = \frac{Im\{Z_1\}}{Re\{Z_1\}}, \tag{1.1}$$

$$Z_1 = Z_0 \frac{1+S_{11}}{1-S_{11}}. \tag{1.2}$$

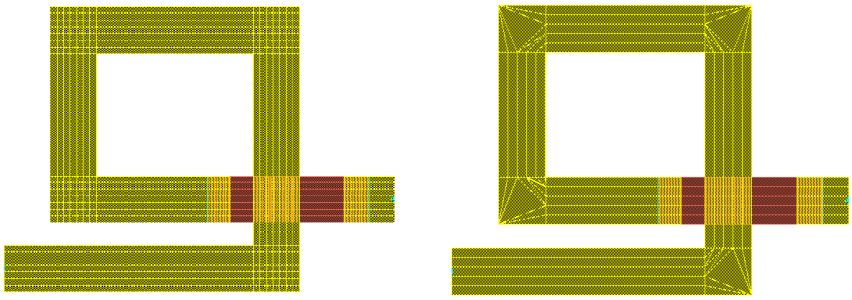

Fig. 1.6 Different meshing of an inductor. Left side, predefined number of cells with transmission line approximation without edge mesh. Right side, automatic mesh with edge mesh.

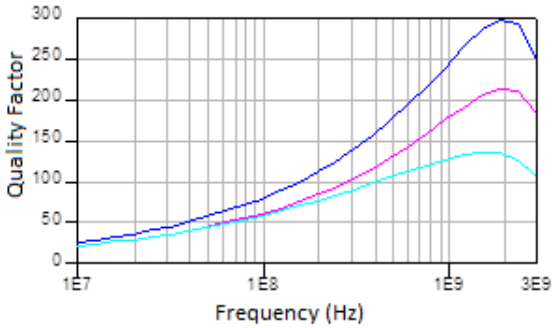

Fig. 1.7 Quality factor of inductor in Fig.1.6 after applying a different mesh. In blue 1 cell/λ , in magenta 7 cell/λ without edge mesh and turquoise 7 cell/λ with edge mesh.

Equally important is to notice that, the value of Q obtained by means of (1.1) and (1.2), depends on which of the port is connected to ground; specially, in this case where square inductors (i.e. asymmetric inductors) are used. Thereby, the methods developed in Chapter 2 allow to represent Q independently of the port connection and moreover, it allows to compare symmetric and asymmetric inductors in an universal way.

As it has been mention in the last section, in addition to a proper mesh, an accurate substrate definition is also needed. Once, both parameters are correctly conjugated, an EM simulator can resolve accurately a given device as it is shown in Table 1.2 for the inductors in Fig. 1.5.

Table 1.2 Comparison between simulated and measured inductance, quality factor and self resonance frequency of the inductors in Fig. 1.5.

	Inductance (nH)		Max. Q		SRF. (GHz)	
	Sim.	Meas.	Sim.	Meas.	Sim.	Meas.
Ind1	21.03	21.08	120	110	1.598	1.600
Ind2	31.39	30.49	98	90	1.190	1.200
Ind3	60.00	58.00	82	81	0.753	0.763

1.4.3 Low noise amplifier design in terms of S-parameters

The low noise amplifier is a key component in a receiver, since it rules the noise figure of the resultant system. The most generalized form of facing the design of a LNA is by mean of S-parameters. Thus, in a very synthesized description, the design of a LNA consists on finding out which are the optimum input and output impedance, which allow to an amplifier to transfer the maximum input power without degrading the input-output signal-noise ratio, also known as noise figure (i.e. $F = \frac{S_{out}}{N_{out}} / \frac{S_{in}}{N_{in}}$). After that, both impedances are synthesized with the proper input and output matching network. Thus, from a design point of view, the matching networks has to accomplish the next goals:

1. A minimum noise figure (NF). By means of the input matching network, the correct input impedance, Z_{opt}, is offered to the input of the amplifier. Thus, Γ_{in} must equal Γ^*_{opt}.
2. Maximum gain power (G_{max}). Since input matching network is intended to achieve a minimum noise figure, commonly a perfect matching gain condition can not be achieved. However, the output matching network still has to be designed to transfer the maximum input power to the load. Therefore, Γ_{out} must equal Γ^*_L.

3. Stability in a wide range of frequencies.
4. Input and output VSWR as closer to unity as possible.
5. As high linearity as possible, through 1-dB compression point or 3^{rd}-order intermodulation product.

Thus, for the amplifier in Fig. 1.8, two separate matching networks adapt the source and load impedance with the desired Z_{opt} and Z_{out}, respectively. As it was shown with the "*RF hexagon*", the many design specifications are all interrelated, and it makes the problem almost unmanageable without some computer optimization strategy. Even though, by means of S-parameters, one can obtain a good physical understanding of these often conflicting requirements, from a study of the stability circles, the constant power-gain circles, the constant impedance-mismatch circles, and the constant noise-figure circles plotted on a Smith chart.

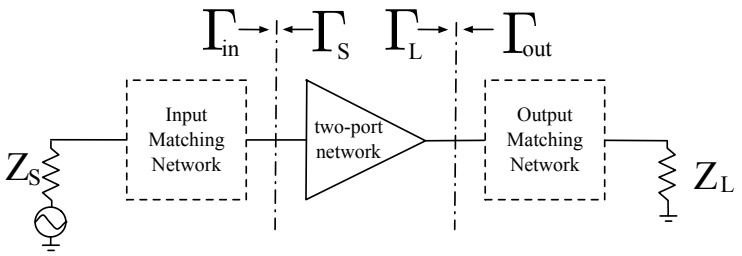

Fig. 1.8 One stage amplifier with input and output matching networks.

Therefore, the design of a LNA consists on keeping the stability constraints, by the need for large power gain, low noise, and low input and output VSWRs. The conditions for amplifier stability is that the reflected power from the amplifier ports need to be smaller than the incident power. This means that the reflection coefficients looking into the amplifier ports, in Fig. 1.8, must have a magnitude less than one for all passive source and load impedance. If a reflection coefficient has a magnitude greater than unity, the amplifier input or output impedance would have a negative real part which is well known a condition for designing an oscillator. Therefore, the condition for stability are as follows

$$\begin{aligned} \Gamma_{in} &= \left| \frac{S_{11} - |S|\Gamma_L}{1 - S_{22}\Gamma_L} \right| < 1 \quad \text{for all } |\Gamma_L| < 1 \\ \Gamma_{out} &= \left| \frac{S_{22} - |S|\Gamma_S}{1 - S_{11}\Gamma_S} \right| < 1 \quad \text{for all } |\Gamma_S| < 1. \end{aligned} \tag{1.3}$$

Commonly, a device can be potentially unstable, and it can happen that $|\Gamma_{in}|$ is lower that one, for only a restricted set of values of Γ_L (i.e. Z_L). Likewise, $|\Gamma_{in}|$ can be lower than one for only a restricted set of values for the source impedance Z_S. In this case the device behaves conditionally stable. Therefore, the condition $|\Gamma_{in}| = 1$

sets the boundary for stability and it can be mapped in the Smith chart as a circle. Moreover, if the load impedance, Z_L, is matched (i.e. $|\Gamma_L|$ equals zero), from (1.3) results that $|S_{11}|$ has to be lower than one. Similarly, if the source impedance, Z_S, is matched (i.e. $|\Gamma_S|$ equals zero), $|\Gamma_{out}|$ is lower than one only if $|S_{11}|$ is lower than one. From the bilinear transformation in (1.3), it can be found the center and radio of such circles with the next expressions

$$\begin{aligned} \Gamma_{LC} &= \frac{S_{11}|S| - S_{22}}{|S|^2 - |S_{22}|^2} \\ R_{LC} &= \frac{|S_{12}S_{21}|}{\left|\left(|S|^2 - |S_{22}|^2\right)\right|}. \end{aligned} \tag{1.4}$$

From the symmetry of expressions in (1.3) the same kind of circles can be plotted for the source impedance but now boundary condition is given by $|\Gamma_{out}|$ equals one. Analyzing all the cases for how circles can be mapped in the Smith chart leads to the next unconditional stability conditions

$$\begin{aligned} K &= \frac{1 - |S_{11}|^2 - |S_{22}|^2 + |S|^2}{2|S_{12}S_{12}|} > 1 \\ &|S_{11}| < 1 \ , \ |S_{22}| < 1 \\ &|S_{12}S_{21}| < 1 - |S_{11}|^2 \ , \ |S_{12}S_{21}| < 1 - |S_{22}|^2 \end{aligned} \tag{1.5}$$

where K is the well known rolling factor. After some algebra it can be demonstrated that whenever $|S| < 1$, $|S_{11}| < 1$ and $|S_{11}| < 1$, then $K > 1$ is sufficient to guarantee absolute stability. That is the reason why K is a popular parameter to analyze amplifier stabilization. In the case of conditional stabilization there are specific cases which can be analyze in low noise amplifier bibliography [7].

Once the device is stable, one can define different gain expressions according the matching conditions

$$\begin{aligned} \text{Power gain}, G_p &= \frac{\text{power delivered to the load}}{\text{input power to the amplifier}} \\ \text{Transducer gain}, G_t &= \frac{\text{power delivered to the load}}{\text{available input power from source}} \\ \text{Available power gain}, G_a &= \frac{\text{available load power}}{\text{available input power from source}}. \end{aligned} \tag{1.6}$$

In the case that perfect matching can be achieved, the next conditions stand $G_p = G_t = G_a = G_{max} =$ maximum gain. The transducer power gain is most frequently used since the available source power is a given and the power in the load is what should be maximized. Thereby, transducer power gain can be written in terms of the

S-parameters of the device and the input(output) reflection coefficient of the source and load as follows

$$G_t = \frac{\left(1-|\Gamma_L|^2\right)\left(1-|\Gamma_S|^2\right)|S_{21}|^2}{|(1-S_{22}\Gamma_L)(1-S_{11}\Gamma_S)-S_{12}S_{21}\Gamma_S\Gamma_L|^2}. \tag{1.7}$$

This expression can be written in terms of $\Gamma_{in}^*\,(\Gamma_{out}^*)$ if $(1-S_{22}\Gamma_L)$ is factorized, thereby

$$G_t = \frac{\left(1-|\Gamma_S|^2\right)}{|1-\Gamma_{in}\Gamma_S|^2}|S_{21}|^2\frac{\left(1-|\Gamma_L|^2\right)}{|1-S_{22}\Gamma_L|^2} \tag{1.8}$$

Notice that (1.7) can be written but factorizing $(1-S_{11}\Gamma_L)$ and a symmetric expression is found

$$G_t = \frac{\left(1-|\Gamma_S|^2\right)}{|1-S_{11}\Gamma_S|^2}|S_{21}|^2\frac{\left(1-|\Gamma_L|^2\right)}{|1-\Gamma_{out}\Gamma_L|^2} \tag{1.9}$$

From (1.8) or (1.9), the gain defined depends on its S-parameters and the input(output) reflection coefficients $\Gamma_{in}^*\,(\Gamma_{out}^*)$. Commonly, in the case when the maximum transference of power is desired, the next equalities apply

$$\Gamma_L^* = \Gamma_{out} = \frac{S_{22}-|S|\,\Gamma_S}{1-S_{11}\Gamma_S} \tag{1.10}$$

$$\Gamma_S^* = \Gamma_{in} = \frac{S_{11}-|S|\,\Gamma_L}{1-S_{22}\Gamma_L}. \tag{1.11}$$

Expression (1.10) can be replaced into (1.11) and solved for Γ_S which reads as follows

$$\Gamma_S = \frac{1}{2B_1}\left[A_1 \pm \left(A_1^2-4\,|B_1|^2\right)^{1/2}\right]. \tag{1.12}$$

Similarly, replacing (1.11) in (1.10), and solving for Γ_L

$$\Gamma_L = \frac{1}{2B_2}\left[A_2 \pm \left(A_2^2-4\,|B_2|^2\right)^{1/2}\right] \tag{1.13}$$

where

$$\begin{aligned} A_1 &= 1+|S_{11}|^2-|S_{22}|^2-|S|^2 \\ A_2 &= 1+|S_{22}|^2-|S_{11}|^2-|S|^2 \\ B_1 &= S_{11}-|S|\,S_{22}^* \\ B_2 &= S_{22}-|S|\,S_{11}^*. \end{aligned} \tag{1.14}$$

With (1.12) and (1.13), one can obtain the optimum input(output) impedance for matching gain. A different value results in a lower gain, thereby from (1.8) or (1.9) a set of gain circles can be mapped as well in Smith chart. The center and the radio of the gain circle are given by the next expressions

$$\begin{aligned} \Gamma_{Lg} &= \frac{\left(S_{22}^{*} - \Delta^{*} S_{11}\right) g_p}{\left(|S_{22}|^2 - |\Delta|^2\right) g_p + 1} \\ R_{Lg} &= \frac{\left(1 - 2K g_p |S_{12}S_{21}| + g_p^{*} |S_{12}S_{21}|^2\right)^{\frac{1}{2}}}{\left|\left(|S_{22}|^2 - |\Delta|^2\right) g_p + 1\right|}. \end{aligned} \tag{1.15}$$

Equation (1.15) is expressed in terms of K and the normalized power gain, g_p, which is the transducer power gain, (1.8), normalized by $|S_{21}|^2$. Writing In terms of the parameter K, the power gain for an absolutely stable device, and using conjugate impedance matching, G_t reads as follows

$$G_t = \left|\frac{S_{21}}{S_{12}}\right| \left(K - \sqrt{K^2 - 1}\right). \tag{1.16}$$

The parameter $|S_{21}/S_{12}|$ is called the "*Figure of Merit*" for the transistor. When $K = 1$, (1.16) gives the maximum stable gain. Nevertheless, for a LNA power matching is not normally desired due to the fact that it is not the best impedance match for noise, thereby it is common practice to plot the normalized constant power-gain circles that correspond to gains 1 dB, 2 dB, 3 dB, etc., less than the maximum normalized power gain $\left(K - \sqrt{K^2 - 1}\right) / |S_{12}S_{21}|$ for an absolutely stable device. For a potentially unstable device, constant power-gain circles for normalized gains 1 dB, 2 dB, etc., less than the normalized "*Figure of Merit*" gain $G = (|S_{21}| / |S_{12}|) = 1/|S_{12}S_{21}|$ are usually plotted.

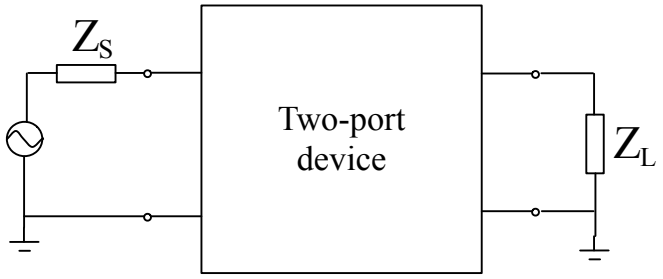

Fig. 1.9 External representation of the noise sources of a two-port device.

A similar development leads to noise circles. Since a two-port device can be represented by the equivalent ideal two-port device and the respective noise source as in Fig. 1.9; in general, the noise figure for a linear two-port has the form

$$F = F_{min} + \frac{r_n}{g_s}\left|Y_s - Y_{s,opt}\right|, \tag{1.17}$$

where r_n is the equivalent input noise resistance of the two-port, Y_s represents the source admittance, meanwhile $Y_{s,opt}$ is the source admittance which results in the minimum noise figure, F_{min}. If Y_s and $Y_{s,opt}$ are expressed in terms of reflection coefficients and are substituted in (1.17), noise figure expression results in a equation that again has the form of a circle

$$F - F_{min} = 4r_n \frac{\left|\Gamma_s - \Gamma_{opt}\right|^2}{\left(1 - |\Gamma_s|^2\right)\left|1 + \Gamma_{opt}\right|^2}. \tag{1.18}$$

Thereby, for a given noise figure, F, the solutions for G_s lies on a circle. The equations for these circles can be found given the parameters Γ_{opt}, F_{min}, and r_n. Unless accurately specified on the data sheet for the device being used, these quantities must be found experimentally. Generally, the source reflection coefficient would be varied by means of a tuner to obtain a minimum noise figure as read on a noise figure meter. F_{min} can then be read off the meter and the source reflection coefficient can be determined on a network analyzer. Likewise, the equivalent noise resistance, r_n, can be found by making one additional noise figure reading with a known source reflection coefficient. If a 50Ω source is used, for example, Γ_s equals zero and the resultant expression from (1.18) can be used to calculate r_n

$$r_n = \left[F_{(\Gamma_s=0)} - F_{min}\right] \frac{\left|1 + \Gamma_{opt}\right|^2}{4\left|\Gamma_{opt}\right|^2}. \tag{1.19}$$

Thereby, noise circles are defined over Γ_S. And from (1.18), if Γ_S equals Γ_{opt}, noise figure equals the minimum noise figure achievable, F_m. Expression resulting for noise figure circles can be simply expressed if the noise figure parameter, N_i, is defined as follows

$$N_i = \frac{\Gamma_s\Gamma_s^* - \Gamma_s\Gamma_{opt}^* - \Gamma_s^*\Gamma_{opt} + \Gamma_{opt}\Gamma_{opt}^*}{1 - \Gamma_s\Gamma_s^*} \tag{1.20}$$

Thereby, the center and radio of noise circles are given by the next expressions

$$\begin{aligned} \Gamma_{Sf} &= \frac{\Gamma_{opt}}{N_i + 1} \\ R_f &= \frac{\sqrt{N_i^2 + N_i\left(1 - \left|\Gamma_{opt}\right|^2\right)}}{1 + N_i}. \end{aligned} \tag{1.21}$$

Noise circles are represented on the Smith chart for the different values of N_i 4 dB, 3 dB, 2 dB, and so on until the minimum noise figure corresponding to F_m.

Introducing the obtained expressions in a circuit simulator as Advanced Design System from Agilent, the design and fabrication of a LNA working at 868 MHz has been carried out. A high performance NPN bipolar transistor, AT32033 from Avago, is used as a common source single transistor configuration. The schematic is shown in Fig. 1.10. This transistor has a minimum noise figure for a 2 mA polarization current as can be obtained from the transistor datasheet. It is well-known that, in common source configuration, the introduction of an inductor in the emitter introduces a new design variable enabling the possibility to modulate the real part of the input impedance. Thanks to this fact, real part of the input impedance can be pushed to 50Ω. However, it is not possible to achieve a simultaneous match for both noise and gain and for Γ_{opt} the maximum gain possible can not be reached. Therefore, designer has to choose an optimum value based on required specification and the configuration of gain and noise circles. In this situation, from the circuit analysis, the minimum noise figure and input impedance are given by the next expressions

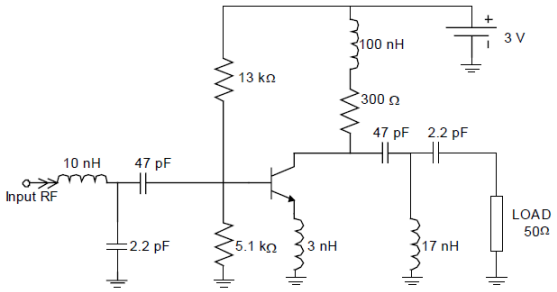

Fig. 1.10 Schematic of a 868 MHz single transistor LNA.

$$Z_{in} = j\omega L_E + \frac{1}{j\omega C_\pi} + \frac{g_m L_E}{C_\pi}, \tag{1.22}$$

$$F_{min} = 1 + \sqrt{\frac{1}{\beta_{DC}} + \frac{\omega^2 L_E^2}{r_\pi^2} - \frac{\omega^4 L_E^4}{r_\pi^2}\frac{(1+\beta_{DC})^2}{\beta_{DC}^2}}, \tag{1.23}$$

where L_E is the inductance at the emitter, ω is the working frequency, β_{DC}, r_π and C_π are the current gain, input resistance and input capacitance of the AT32033 transistor.

Once components in Fig. 1.10 have been properly chosen, following the procedure shown in Sections 1.4.1 and 1.4.2, the different inductors have been designed with the aid of an electromagnetic simulator. For this application, capacitors are SMD components due to the impractical sizes at those frequencies. At this point, it is worth to notice that the influence of the parasitic in the PCB can be taken into

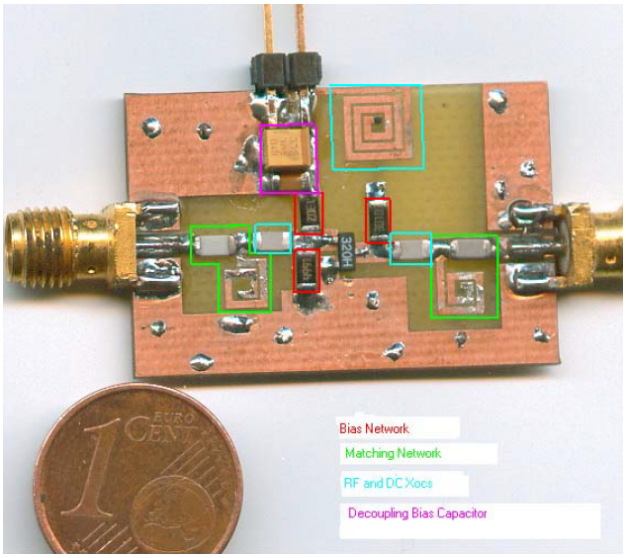

Fig. 1.11 LNA implementation with embedded components.

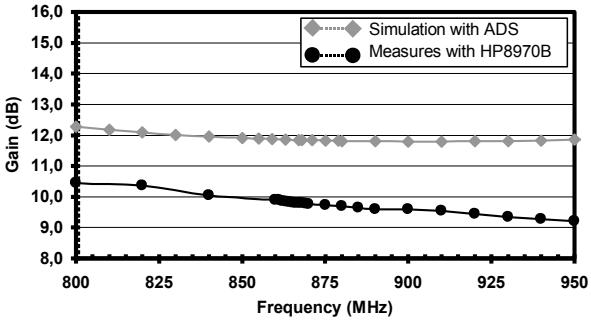

Fig. 1.12 LNA measured and simulated gain.

account with the EM simulator. Thus, the final inductor must take into account the extra added inductance and the stray capacitance through the ground plane up to the reference input port. Following this procedure, the complete layout has been optimized for the operation at 868 MHz. The final implementation is shown in Fig. 1.11. Whereas capacitors and resistors are based on SMD components, all inductors have been printed on the PCB. The dimensions are 2.1 cm x 3.1 cm.

Different tests have been carried out to check the performance of the LNA. First, the gain vs. frequency in small signal configuration has been measured. An HP8753C network analyzer has been used for this set-up. Proper de-embedding procedure has been applied to the measured data. Therefore, the influence of the

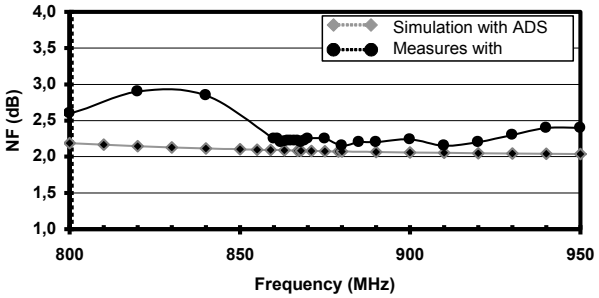

Fig. 1.13 LNA measured and simulated noise figure.

connectors has been removed. Fig. 1.12 shows the obtained transducer gain specs. At 868 MHz, the gain is 9.7 dB. Discrepancies are mainly due to differences in the input and output matching networks.

Second, a noise figure characterization has been done using the HP8970B noise figure meter and a calibrated noise source HP346B. The LNA has been chased in aluminium to reduce the picked-up external interference. Measured and simulated data have been represented in Fig. 1.13. In most of the range both data agrees with in 0.2 dB. At 868 MHz, the measured value of the noise figure is 2.2 dB.

1.5 Conclusion

In one hand, the main considerations in the design of RF circuits has been exposed, at the same time that current bottlenecks and lacks have been highlighted. Thereby, two research lines are remarked in order to improve the design of differential circuits and the synthesis of integrated inductors. In the other hand, this work has demonstrated the feasibility of using a FR4 low-cost substrate for the design of RF hybrid circuits working in the low GHz range where the passives can be embedded. Moreover, a fast method for the characterization of the substrate has been given. In addition, the study of embedding the components in the substrate has shown that reasonable quality factors can be achieved. As a demonstrator, a hybrid LNA has been designed having that fits typical specs of one transistor amplifiers: 9.7 dB of transducer gain, 2.2 dB of noise figure and a 1 dB input compression point of -18.8 dBm.

References

1. A.R. Djordjevic, R.M. Biljie, V.D. Likar-Smiljanic, and Yu Zhang. Wideband frequency-domain characterization of fr-4 and time-domain causality. *Electromagnetic Compatibility, IEEE Transactions on*, 43(4):662–667, Nov.
2. R. W. Rhea. Designing a low-noise VCO on FR4. Technical report, RFdesign, September 1999. www.rfdesign.com.
3. R.R. Tummala and V.K. Madisetti. System on chip or system on package? *Design Test of Computers, IEEE*, 16(2):48–56, Apr-Jun.
4. L.S. Napoli and J.J. Hughes. A simple technique for the accurate determination of the microwave dielectric constant for microwave integrated circuit substrates (correspondence). *Microwave Theory and Techniques, IEEE Transactions on*, 19(7):664–665, Jul.
5. Hewlett Packard. *Permittivity measurements of PC Board and Substrate Materials Using the HP 4291A and HP 16453A*. Application Note 1255-3.
6. S.H.Chao. An uncertainty analysis for the measurement of microwave conductivity and dielectric constant by the short-circuited line method. *IEEE Trans. Instrument Meas.*, IM-35:36–41, Mar. 1986.
7. Robert E. Collin. *Foundations for Microwave Engineering*. Wiley-IEEE Press, 2 edition, December 2000.

Part I
Methods for optimizing the design of differential circuits

Scattering parameter theory represents the cornerstone of radio- and micro-wave frequency theory. They have been used to characterize the physical and electrical behavior of every linear frequency dependent device from the simplest ones such as terminations and attenuators to the more complex antennas, hybrids, filters or amplifiers. Thus, S-parameters have been broadly used in fields like electrical engineering, electronics engineering, and communication systems design, and especially for microwave engineering. Even though, the first descriptions of S-parameters can be found in the thesis of Vitold Belevitch in 1945 [1], and a later work on radars conduced by Robert Henry Dicke in 1947 [2], we owe their current description to Kurokawa's work in [3]. The key point of his work is the definition of the incident and reflected power waves transmitted through a transmission line when these power waves scatter with a change in the media. This effect is more easily quantified by means of power waves than currents and voltages at high frequencies. Thus, Kurokawa finally writes the fundamental equation $b = Sa$, where b represents the reflected normalized power waves, a represents the incident normalized power waves and S is an $n\ x\ n$ matrix which describes the physical behavior of a n-port device. Since then, S-parameters has been broadly used as they were described in Kurokawa's work and pieces of master books has been written as [4]. However, at the same time that electronic circuits and systems have grown in complexity, differential topologies have become more commonly used. Even though, in these cases, the device can still be described as a $2n\ x\ 2n$ matrix where physical ports are referred against a common-ground, it was Bockelman and Eisenstadt in [5] who first introduced the mixed-mode scattering parameters, which more properly express the differential and common-mode behavior of such devices. Since then, mixed-mode S-parameters have been used with varying degree of success. Thereby, differential(common) input reflection coefficient is wrongly assumed to $S_{dd}\,(S_{cc})$; thus, differential(common) input impedance is also wrongly obtained by the bi-linear transformation of $S_{dd}\,(S_{cc})$. This misunderstanding has important consequences, specially when symmetry is not perfectly guarantied. Likewise, it drives to the nonexistence of a well defined impedance transformation and matching theory in terms of mixed-mode S-parameters and consequently to the lack of a design framework for classical high frequency amplifiers in terms of mixed-mode scattering parameters.

Within this framework, the first part of the thesis is devoted to extend the theory of mixed-mode scattering parameters filling up most of the lacks of the current theory. For this proposal, in Chapter 2, the simplest case of a two-port device is developed. As instance, it allows the characterization and comparison of symmetric and spiral inductors, which have remained a controversy point until now. Furthermore, the power dissipated on a two-port device, when it is seen as a symmetric load, is reviewed, showing interesting properties of this kind of devices. After solving this case, Chapter 3 extends the theory to a n-port device. Thereby, generalized S-parameters are used to obtain a new expression for the input reflection coefficient of a n-port device. Moreover, power match theory is extended to multiple-port devices showing that there exist a duality between standard S-parameters and mixed-mode

S-parameters but at the same time, there are important differences that have to be taken into account in a fine design.

References

1. V. Belevitch. Summary of the history of circuit theory. *Proceedings of the IRE*, 50(5):848 –855, may 1962.
2. R. H. Dicke. A computational method applicable to microwave networks. *Journal of Applied Physics*, 18(10):873 –878, oct 1947.
3. K. Kurokawa. Power waves and the scattering matrix. *Microwave Theory and Techniques, IEEE Transactions on*, 13(2):194 – 202, mar 1965.
4. R.E. Collin. *Foundations for Microwave Engineering*. IEEE Press Series on Electromagnetic Wave Theory. John Wiley & Sons, 2001.
5. D.E. Bockelman and W.R. Eisenstadt. Combined differential and common-mode scattering parameters: theory and simulation. *Microwave Theory and Techniques, IEEE Transactions on*, 43(7):1530 –1539, jul 1995.

Chapter 2
Mixed-mode impedance and reflection coefficient of a two-port device

Abstract From the point of view of mixed-mode scattering parameters, S_{mm}, a two-port device can be excited using different driving conditions. Each condition leads to a particular set of input reflection coefficient and input impedance definitions that should be carefully applied depending on the type of excitation and symmetry of the two-port device. Therefore, the aim of this chapter is to explain the general analytic procedure for the evaluation of such reflection coefficients and impedance in terms of mixed-mode scattering parameters. Moreover, the driving of a two-port device as a one-port device is explained as a particular case of a two-port mixed-mode excitation using a given set of mixed-mode loads. The theory is applied to the evaluation of the quality factor, Q, of symmetrical and non-symmetrical inductors.

2.1 Introduction

This chapter is an extension of the paper with the same title, published in the journal *Progress in Electromagnetic Research*[1]. Here, some explanations have been reviewed and two new sections have been added. This first new section treats the subject in terms of Z-parameters, showing that the obtained expressions are consistent and non-dependent of how the two-port is described. The second deals with how power is transferred in to a two-port device when it is used as a termination. Both of them are necessary for further development in the next chapters.

Currently, most of the RFICs are designed to work in differential configuration due to noise immunity. In fact, the majority of the receiver chipsets available in today's market, as well as some of the components that conform them, are fully differential [1, 2]. Obviously, it implies that the figures of merit of these devices are better expressed in terms of mixed-mode scattering parameters (S_{mm}),

[1] C. T. Carrasco, C. J. Sieiro, J. M. López-Villegas, N. Vidal, R. González-Echevarría, and M. E. Roca, "Mixed-mode impedance and reflection coefficient of two-port devices," Progress In Electromagnetics Research, Vol. 130, 411-428, 2012.

which were first introduced by Bockelman and Eisenstadt [3, 4]. In spite of their widespread use in RFIC design, there is still some misunderstanding about how the differential(common)-mode input impedance $Z_d\,(Z_c)$ must be calculated in terms of S_{mm} when a two-port is seen as a one-port device. Thus, it is usually found that the differential reflection coefficient Γ_d of a two-port device is assumed to be S_{dd} [5, 6, 7, 8]. Therefore, the differential input impedance is calculated using the following bilineal impedance transformation

$$Z_{dd} = 2Z_0 \frac{1+S_{dd}}{1-S_{dd}} \tag{2.1}$$

where $2Z_0$ is the differential surge impedance. Certainly, Z_{dd} in (2.1) coincides with the differential term of the mixed-mode Z-parameter matrix of a two-port device; however, as it has been previously mentioned in [9] and [10], a close look to (2.1) reveals that such expression only matches with Z_d (i.e. $Z_d = Z_{dd}$) for fully symmetrical two-port devices. For non-symmetrical devices and taking into account the definition of S_{dd}, (2.1) neglects any conversion to a reflected common-mode power wave. Then, special care must be taken when using (2.1) as an equivalent expression to Z_d. For instance, the evaluation of the quality factor Q using the next definition

$$Q = \frac{Im\{Z_{dd}\}}{Re\{Z_{dd}\}} \tag{2.2}$$

should be only applied to symmetrical topologies. For non-symmetrical inductors, e.g. spiral inductors, (2.2) wrongly estimates Q, due to the fact that the component boundary conditions are wrongly set, thus the common-mode conversion is completely dismissed. A similar misunderstanding can be pointed out when Z_{cc} is directly related to Z_c; in this case, any conversion to differential-mode is not considered.

To avoid the former problem, [10] and [11] transform the description of the two-port device from S-parameters to Z-parameters. Then, a floating current or voltage source is applied between the input ports of the device, instead of normalized power waves. These boundary conditions lead to a different input impedance definition which can be transformed back to S-parameters. Besides, an equivalent solution is found in [12] and [13] by means of applying the same floating signal sources to the two-port, but such boundary conditions are straightly expressed in terms of S-parameters, instead of transforming to Z-parameters. In both cases, the input impedance found shows the non-symmetrical response of the device. However, up to the author's knowledge no procedure expressing $\Gamma_d\,(\Gamma_c)$ or $Z_d\,(Z_c)$ in terms of S_{mm} has been yet proposed. Even more, all previous cases must be understood as particular cases of a general expression based on the definitions of mixed-mode scattering parameters and loads.

Within this framework, the rest of this chapter is devoted to extend the theory of mixed-mode scattering parameters not only to symmetrical devices, but to non-symmetrical or actual devices. For this reason, in Section 2.2, a general expression of $\Gamma_d\,(\Gamma_c)$ will be obtained which resembles the well-known expressions of $\Gamma_{in}\,(\Gamma_{out})$

for a single-ended two-port device. Such definitions will allow to obtain $Z_d\,(Z_c)$ in terms of S_{mm}. In Section 2.3, it is shown that former particular cases of the driving of a two-port device are reduced to the application of a short, open and matched mixed-mode load conditions on the general expression of $\Gamma_d\,(\Gamma_c)$. At this point, two new sections have been added. In Section 2.4, some of the expressions obtained are newly demonstrated in terms of Z-parameters. These parameters are broadly used to describe lineal systems, especially in low-frequency application; thereby, this section faces the former problem from an easier point of view for those who come from low-frequency design. Since, a two-port device can be used as a termination for differential systems, in Section 2.5, the transferred power into a load is obtained in terms of the available power in a differential power source. As a practical case, in Section 2.6 an adequate definition of Q will be obtained, by means of Z_d, that allows the direct comparison between symmetrical and non-symmetrical inductors. Finally, the conclusions of this work are presented in Section 2.7.

2.2 Input reflection coefficient of a two-port device

When attempting to calculate $\Gamma_d\,(\Gamma_c)$, it is useful to keep in mind the definition of the input(output) reflection coefficient $\Gamma_{in}\,(\Gamma_{out})$ of a two-port device. As it can be seen in Fig. 2.1, Γ_{in} is defined as the quotient between the incident power wave a_1 and the reflected power wave b_1 at the input port P_1, when a load Z_L has been connected to the output port.

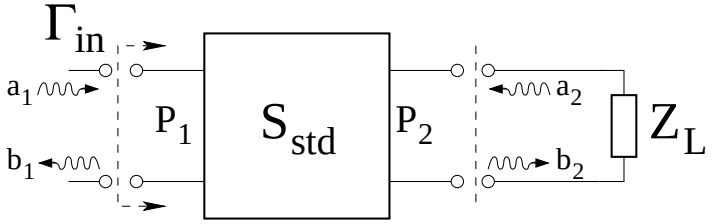

Fig. 2.1 Input reflection coefficient of a two-port device in standard S-parameters.

Besides, Γ_{out} is the reflection coefficient towards the output port P_2, when a source impedance Z_S has been connected to the input port [14, 15]. Due to the fact that there is a linear transformation between S and S_{mm}, i.e. $S = M^{-1}S_{mm}M$ [16], the two-port network in Fig. 2.1 can be represented as a two-port device where the input port and the output port have been substituted by a differential and common-mode ports. At this point, $\Gamma_d\,(\Gamma_c)$ can be correctly defined by analogy to $\Gamma_{in}\,(\Gamma_{out})$. Consequently, $\Gamma_d\,(\Gamma_c)$ is the input reflection coefficient of a two-port device when exciting with a differential(common)-mode power wave meanwhile the two-port device is loaded with a common(differential)-mode load.

2.2.1 Differential-mode input reflection coefficient, Γ_d

Fig. 2.2 shows how a differential power wave a_d is launched towards a two port device meanwhile a common-mode impedance Z_L^c is connected to the common-mode port. S_{mm} relates the incident and reflected differential and common-mode

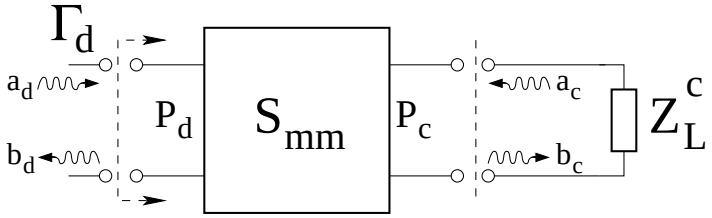

Fig. 2.2 Differential-mode reflection coefficient of a two-port device in mixed-mode S-parameters.

power waves by

$$\begin{pmatrix} b_d \\ b_c \end{pmatrix} = \begin{pmatrix} S_{dd} & S_{dc} \\ S_{cd} & S_{cc} \end{pmatrix} \begin{pmatrix} a_d \\ a_c \end{pmatrix}. \tag{2.3}$$

In this case, the two-port scatters back two power waves b_d and b_c. The common-mode reflected wave b_c reaches the common-mode load Z_L^c, which reflects a common-mode wave a_c. Thereby, it can be written the following relation

$$a_c = \Gamma_L^c b_c \tag{2.4}$$

where Γ_L^c is the reflection coefficient associated with Z_L^c. Replacing (2.4) in (2.3) and after some algebra, Γ_d is expressed as follows

$$\Gamma_d = \frac{S_{dd} - |S|\Gamma_L^c}{1 - S_{cc}\Gamma_L^c}. \tag{2.5}$$

Notice that, whenever a two-port is completely symmetric and balanced (i.e. $S_{11} = S_{22}$ and $S_{12} = S_{21}$, which lead to $S_{dc} = S_{cd} = 0$ and $|S| = S_{dd}S_{cc}$), Γ_d is equal to S_{dd} irrespective of the connected load Z_L^c. In this case, as it has been previously mentioned, Z_d matches Z_{dd}.

It is also interesting to rewrite (2.4) as a function of the incident power wave a_1 and a_2 at each port referred to the common ground. From [3], $a_{d(c)}$ and $b_{d(c)}$ read as

$$\begin{aligned} a_{d(c)} &= \frac{1}{\sqrt{2}}(a_1 \mp a_2) \\ b_{d(c)} &= \frac{1}{\sqrt{2}}(b_1 \mp b_2) \end{aligned} \tag{2.6}$$

where the upper and lower signs hold for the differential and common-mode, respectively. Substituting (2.6) in (2.4), the following relation is obtained

$$a_1 = \text{-}a_2 + \sqrt{2}\Gamma_L^c b_c. \tag{2.7}$$

Note that, even though a differential power wave a_d is launched through the two-port device, a_1 equals -a_2 only in two cases: 1) $\Gamma_L^c = 0$, i.e. the common-mode load is a matched load; 2) $b_c = 0$, i.e. the two-port is purely balanced. For the remaining cases, a_1 differs from -a_2 due to the fact that a common-mode power wave a_c is scattered back by the common-mode load.

Keeping in mind the existing linear transformation between S and S_{mm} parameters, notice the duality of (2.5) when it is compared with the Γ_{in} (Γ_{out}) expression of the single-ended analysis of a two-port device

$$\begin{aligned} \Gamma_{in} &= \frac{S_{11} - |S|\Gamma_L}{1 - S_{22}\Gamma_L} \\ \Gamma_{out} &= \frac{S_{22} - |S|\Gamma_S}{1 - S_{11}\Gamma_S}. \end{aligned} \tag{2.8}$$

By means of this comparison, one realizes that, as in the single-ended case, three standard loads can be defined: a matched load ($\Gamma_L^c = 0$), an open-circuit ($\Gamma_L^c = 1$) and a short-circuit ($\Gamma_L^c = \text{-}1$). Notice that, each of these cases results in a different boundary condition when substituting $\Gamma_L^c = 0, 1, \text{-}1$ in (2.4) as it will be analyzed in Section 2.3.

2.2.2 Common-mode input reflection coefficient, Γ_c

Whenever a common-mode power wave a_c is launched towards a two-port device, as it can be seen in Fig. 2.3, two power waves, b_d and b_c are scattered back. Now, b_d reaches the differential load, Z_L^d, which reflects a differential-mode normalized power wave a_d. The relationship established between a_d and b_d through Z_L^d is

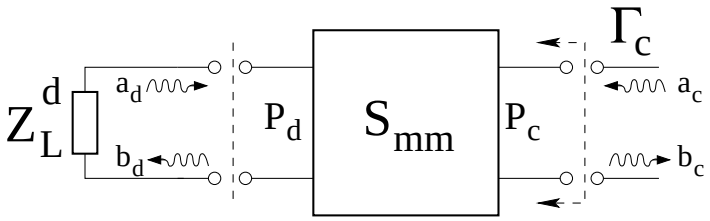

Fig. 2.3 Common-mode reflection coefficient of a two-port device in mixed-mode S-parameters.

$$a_d = \Gamma_L^d b_d \tag{2.9}$$

wherein Γ_L^d is the reflection coefficient of the differential-mode load. A dual expression of (2.5) can be written when substituting (2.9) in (2.3),

$$\Gamma_c = \frac{S_{cc} - |S|\Gamma_L^d}{1 - S_{dd}\Gamma_L^d}. \tag{2.10}$$

Notice that, when the two-port is symmetric and balanced (i.e. $S_{dc} = S_{cd} = 0$ and $|S| = S_{dd}S_{cc}$), Γ_c equals S_{cc} irrespective of the connected load. As it has been previously mentioned, only in this case Z_c matches Z_{cc}.

By replacing (2.6) in (2.9), a_1 relates to a_2 as follows

$$a_1 = a_2 + \sqrt{2}\Gamma_L^d b_d. \tag{2.11}$$

Therefore, even when a common-mode power wave a_c is launched through the two-port device, a_1 equals a_2 only in two cases: 1) $\Gamma_L^d = 0$, i.e. the differential-mode load is a matched load; or 2) $b_d = 0$, i.e. the two port is ideally balanced. Otherwise, a_1 differs from a_2. This is due to the fact that a differential-mode power wave a_d is reflected back by the differential-mode load.

Equation (2.10) represents the dual case of (2.5). Therefore, three differential mixed-mode load conditions can be defined by means of $\Gamma_L^d = 0, 1, \text{-}1$.

2.3 Mixed-mode driving conditions

Three driving conditions can be defined which lead to different boundary conditions for a two-port device and different expressions of $\Gamma_d\,(\Gamma_c)$. In order to explore these driving conditions, it is very illustrative to think about the theoretical realization of a true mixed-mode VNA as the one in Fig. 2.4. Notice that, in contrast to the two-port device in Fig. 2.2 or Fig. 2.3, the device represented in Fig. 2.4 is a physical realization. Therefore, the two-port device represented is formed by two physical single-ended ports and a common-ground. As it is explained in [17] the ground is needed in order to allow the common-mode propagation, in this way the two input ports and the existing common-ground can be associated to either a single-ended or a mixed-mode representation. Actually, the physical realization of a pure-mode VNA (PMVNA) is rather difficult and, even though some works have been conduced toward its consecution [17, 18], current multi-port VNAs implement Bockelman's formulation to display S_{mm}. In fact, a commercial PMVNA is not yet available.

It is also important to notice that the DUT is normally connected to the PMVNA by means of a pair of coupled transmission lines and a ground reference which allows the propagation of differential and common-mode power waves. However, as it has been previously demonstrated in [3], if the even and odd-mode characteristic impedance are chosen to be equal, such reference coupled lines can be considered uncoupled transmission lines. Even more, as it is also mention, there is not restric-

tion for the length of the reference lines, thus zero length transmission lines can be defined and (2.6) still holds on.

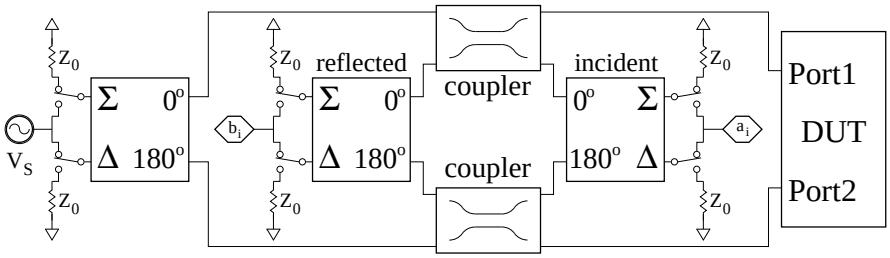

Fig. 2.4 Pure-mode vector network analyzer.

2.3.1 Matched load $\Gamma_L^{d(c)} = 0$

Whenever a power wave is launched from the V_s generator in Fig. 2.4, a switchable 0°/180° hybrid generates either a differential a_d or common-mode a_c power waves. These incident waves can be measured by setting accordingly the 0°/180° input at the incident wave hybrid. When the selected power wave reaches the DUT, the incident power wave is scattered back, as well as an opposite mode wave is generated due to the asymmetry of the two-port device. Both modes can be measured by setting the switchable 0°/180° reflected wave hybrid. It is important to notice that whenever one mode is selected, the opposite mode is connected to its surge impedance $2Z_0$ or $Z_0/2$ through each hybrid, thus non scattered wave from the loads is allowed. This assumption is similar to connect Z_0 at the opposite port with respect to the one that is being measured when the measure of S_{11} or S_{22} is done by means of a classical VNA. Assuming the condition that the incoming wave is a_d, and keeping in mind that $\Gamma_L^c = 0$, from (2.5) Γ_d reads as

$$\Gamma_d = S_{dd}. \tag{2.12}$$

In this case, from (2.4) a_c is equal to zero. Thus, a_1 equals -a_2. Only when the reflected power wave is absorbed in the common-mode load, the normalized power waves ingoing into the two-port device are equal in magnitude and opposite sign, thus they are pure differential signals. Besides, whenever it is assumed that $a_1 =$ -a_2, this condition always leads to $\Gamma_d = S_{dd}$, even though a_c differs actually from zero in an actual measurement setup. Then, it is not surprising that, when attempting to calculate Γ_d by means of a 0°/180° hybrid or an equivalent device which supposedly generates the boundary condition $a_1 =$ -a_2, Γ_d is misunderstood as S_{dd} and any common-mode conversion is directly dismissed.

In order to calculate Z_d, the bilineal transformation (2.1) is valid and Z_d is equal to Z_{dd}.

Likewise, if a_c is launched by the power generator V_s, and $\Gamma_L^d = 0$ is selected at the hybrids, from (2.10) Γ_c reads as

$$\Gamma_c = S_{cc}. \tag{2.13}$$

From (2.9) a_d is equal to zero, thus a_1 equals a_2. Therefore, if the boundary condition $a_1 = a_2$ is assumed, it directly leads to obtain that $\Gamma_c = S_{cc}$, although a_d could actually differ from zero. Then, when Γ_c is calculated by means of a device which supposedly generates $a_1 = a_2$, Γ_c is misunderstood as S_{cc} and any differential-mode conversion is dismissed. In this case, Z_c can be calculated by means of the bilineal transformation

$$Z_c = \frac{Z_0}{2}\frac{1+S_{cc}}{1-S_{cc}} \tag{2.14}$$

where $Z_0/2$ is the surge impedance for the common-mode.

Although the normal operation of a PMVNA is the one previously described, the ports Σ and Δ at the hybrids, where the differential or common-mode load are connected, can be left open or shorted. In these cases, a scattered wave is allowed and $\Gamma_L^{d(c)}$ equals 1 or -1 respectively.

2.3.2 Γ_d when $\Gamma_L^c = 1$

Replacing $\Gamma_L^c = 1$ in (2.5), Γ_d results as follows

$$\Gamma_d = \frac{S_{dd} - |S|}{1 - S_{cc}}. \tag{2.15}$$

As it has been previously mention, if the device is symmetric (i.e. $S_{cd} = S_{dc} = 0$ and $|S| = S_{dd}S_{cc}$), Γ_d equals S_{dd}. It is also interesting to notice that if the device is also floating, as the balanced antenna discussed in [10, 19] (i.e. $S_{cc} = 1$ and $|S| = S_{dd}$), Γ_d calculated by means of (2.15) results in an indetermination. This result was previously mentioned in [20], but now by using (2.5) the indetermination is naturally solved and Γ_d results in S_{dd}.

Once Γ_d has been obtained, Z_d can be easily calculated by means of the bilineal transformation

$$Z_d = 2Z_0\frac{1+\Gamma_d}{1-\Gamma_d}. \tag{2.16}$$

However, it is also very illustrative to obtain Z_d by using circuit theory, i.e. writing the voltage and current signals at each port in terms of mixed-mode S-parameters. Proceeding in this way, both S_{mm} and circuit theory are shown to be mathematically equivalent and, additionally, the goodness of the bilineal impedance transformation is highlighted.

Thus, when $\Gamma_L^c = 1$, (2.7) can be rewritten as

$$a_1 = \text{-}a_2 + \sqrt{2}b_c. \tag{2.17}$$

As it has been previously mentioned, a_1 differs from a_2 except when the two port is purely symmetric. Otherwise, replacing b_c by (2.6) and by means of the following expressions [3]

$$\begin{aligned} V_i &= \sqrt{Z_0}\,(a_i + b_i) \\ I_i &= \frac{1}{\sqrt{Z_0}}(a_i - b_i)\,, \end{aligned} \tag{2.18}$$

(2.17) can be written as $I_1 = \text{-}I_2$. It means that the normalized power waves can be replaced by a floating current source as it is shown in Fig. 2.5 and the result is equivalent to (2.15). Consistently, the condition $I_1 = \text{-}I_2$ implies that there is no common-mode current flowing into the device; thus, from the point of view of the common-mode, it can be seen as an open load, i.e. $\Gamma_L^c = 1$.

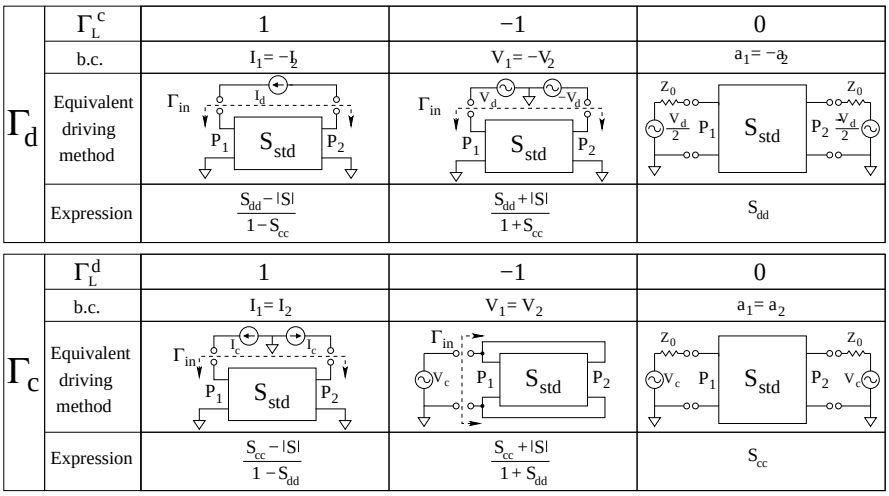

Fig. 2.5 Two-port mixed-mode driving topologies.

In order to calculate Z_d, both currents can be expressed in terms of S-parameters as follows

$$\begin{aligned} I_1 &= \frac{1}{\sqrt{Z_0}}(a_1 - b_1) = \frac{1}{\sqrt{Z_0}}\left[(1 - S_{11})\,a_1 - S_{12}a_2\right] \\ I_2 &= \frac{1}{\sqrt{Z_0}}(a_2 - b_2) = \frac{1}{\sqrt{Z_0}}\left[\text{-}S_{21}a_1 + (1 - S_{22})\,a_2\right]. \end{aligned} \tag{2.19}$$

Thus, a_2 can be written in terms of a_1:

$$a_2 = -\frac{a_1(-1+S_{11}+S_{21})}{-1+S_{22}+S_{12}} = -a_1\frac{S_{cc}+S_{cd}-1}{S_{cc}-S_{cd}-1}. \tag{2.20}$$

Note that for a symmetric and reciprocal two-port device (i.e. $S_{dc} = S_{cd} = 0$), (2.20) results in $a_2 = -a_1$. Otherwise, the ingoing waves are different at each port, and such difference depends on S_{cc} and S_{cd} which convey a common-mode conversion. Now, by means of (2.20), the voltage and currents at each node of the DUT can be rewritten as a function of a_1 as

$$V_i = \sqrt{Z_0}\,a_1\left\{\pm\frac{S_{dd}-S_{cc}+1-|S|}{1-S_{cc}+S_{cd}}+\frac{2S_{cd}}{1-S_{cc}+S_{cd}}\right\} \tag{2.21}$$

$$I_1 = -I_2 = \frac{1}{\sqrt{Z_0}}a_1\frac{S_{dd}-S_{cc}-2S_{cd}+1-|S|}{1-S_{cc}+S_{cd}} \tag{2.22}$$

where in (2.21) the upper and lower signs hold for port 1 and port 2, respectively. As a matter of fact, only when the two-port device is symmetric, (2.21) results in $V_1 = -V_2$.

From (2.21) and (2.22), $V_d = V_1 - V_2$ and $I_d = I_1 = -I_2$ can be calculated and, since Z_d is V_d/I_d, it reads as follows

$$Z_d = Z_0\left(\frac{1+S_{dd}+S_{dc}}{1-S_{dd}-S_{cd}}+\frac{(1+S_{dd}-S_{dc})(1-S_{cc}-S_{cd})}{(1-S_{dd}-S_{cd})(1-S_{cc}+S_{cd})}\right). \tag{2.23}$$

Likewise Γ_d, in some cases, (2.23) can lead to an indetermination if it is directly developed. In order to avoid such indetermination, Z_d can be naturally splitted into two cases: 1) the two-port is ideally symmetric, which means that the second term in (2.23) can be simplified since $S_{cd} = S_{dc} = 0$; 2) otherwise (even when designing the device as a differential component). Therefore, Z_d is expressed as follows

$$Z_d = \begin{cases} 2Z_0\dfrac{1+S_{dd}}{1-S_{dd}} & \text{if } S_{dc} = S_{cd} = 0 \\ \\ 2Z_0\dfrac{S_{dd}-S_{cc}+1-|S|}{1+|S|-S_{dd}-S_{cc}} & \text{Otherwise} \end{cases}. \tag{2.24}$$

As it was expected, Z_d matches Z_{dd} only when the two-port is symmetric. It can be seen that, the same result is obtained by applying the bilineal transformation (2.16) to (2.15). Therefore, the former theory is consistent with circuit theory.

2.3.3 Γ_c when $\Gamma_L^d = 1$

Replacing $\Gamma_L^d = 1$ in (2.10), Γ_c results as follows

$$\Gamma_c = \frac{S_{cc} - |S|}{1 - S_{dd}}. \tag{2.25}$$

Also in this case, when the device is purely balanced and floating (i.e. $S_{dd} = 1$ and $|S| = S_{cc}$), (2.25) results in an indetermination. This indetermination is naturally solved by using (2.10) and Γ_c results in S_{cc}. If the device is simply symmetric and non-mode conversion is allowed, (i.e $S_{dc} = S_{cd} = 0$), Γ_c results in S_{cc}.

Moreover, when $\Gamma_L^d = 1$ and (2.18) are inserted in (2.11), it is obtained that $I_1 = I_2$. Then, the normalized power waves can be replaced by two equivalent current sources connected at both ports as it is shown in Fig. 2.5. This equivalent driving condition is also consistent if one realizes that no differential current is allowed, thus from the point of view of the differential-mode, this boundary condition is seen as an open circuit.

In order to calculate Z_c, (2.25) is substituted in the following bilineal transformation

$$Z_c = \frac{Z_0}{2}\frac{1+\Gamma_c}{1-\Gamma_c}. \tag{2.26}$$

Therefore the common-mode impedance Z_c when $\Gamma_L^d = 1$ results

$$Z_c = \begin{cases} \dfrac{Z_0}{2}\dfrac{1+S_{cc}}{1-S_{cc}} & \text{if } S_{dc} = S_{cd} = 0 \\ \dfrac{Z_0}{2}\dfrac{S_{dd} - S_{cc} - 1 + |S|}{S_{dd} + S_{cc} - 1 - |S|} & \text{Otherwise} \end{cases}. \tag{2.27}$$

As expected, only in the case when the two-port is symmetric Z_c matches with Z_{cc}.

2.3.4 Γ_d when $\Gamma_L^c = -1$

When $\Gamma_L^c = -1$, Γ_d is given by

$$\Gamma_d = \frac{S_{dd} + |S|}{1 + S_{cc}}. \tag{2.28}$$

Again, if the device is purely symmetric (i.e. $S_{dc} = S_{cd} = 0$ and $|S| = S_{dd}S_{cc}$), Γ_d results in S_{dd} as expected. It is also interesting to write (2.7) when $\Gamma_L^c = -1$,

$$a_1 = -a_2 - \sqrt{2}b_c. \tag{2.29}$$

As it has been previously mentioned, a_1 differs from $-a_2$ except when the two port is purely symmetric. Otherwise, replacing b_c by (2.6) and by means of (2.18), $V_1 = -V_2$. Again, the power waves sources can be replaced by single-ended voltage sources as

it is shown in Fig. 2.5. Notice from Fig. 2.5 that the common-mode node between the differential voltage sources is shorted, thus $\Gamma_L^c = $ -1.

Thus, Z_d can be calculated replacing (2.28) in the impedance transformation (2.16),

$$Z_d = \begin{cases} 2Z_0 \dfrac{1+S_{dd}}{1-S_{dd}} & \text{if } S_{dc} = S_{cd} = 0 \\ \\ 2Z_0 \dfrac{S_{dd}+S_{cc}+1+|S|}{1-|S|-S_{dd}+S_{cc}} & \text{Otherwise} \end{cases}. \tag{2.30}$$

2.3.5 Γ_c when $\Gamma_L^d = $ -1

Replacing $\Gamma_L^d = $ -1 in (2.10), Γ_c reads as

$$\Gamma_c = \frac{S_{cc}+|S|}{1+S_{dd}}. \tag{2.31}$$

Likewise in the previous cases, when the device is symmetric (i.e. $S_{dc} = S_{dc} = 0$ and $|S| = S_{dd}S_{cc}$), Γ_c results in S_{cc}. Once more, rewriting (2.11) when $\Gamma_L^d = $ -1,

$$a_1 = a_2 - \sqrt{2}b_d. \tag{2.32}$$

As it has been previously mentioned, a_1 differs from a_2 except when the two port is purely symmetric. Otherwise, replacing b_d by (2.6) and by means of (2.18), $V_1 = V_2$. In this case, the power waves can be replaced by a voltage source connected to both ports as in Fig. 2.5. Therefore, any differential voltage source has been shorted; it implies that from the point of view of the differential-mode, Γ_L^d equals -1.

A new expression for Z_c can be calculated replacing (2.31) in (2.26),

$$Z_c = \begin{cases} \dfrac{Z_0}{2}\dfrac{1+S_{cc}}{1-S_{cc}} & \text{if } S_{dc} = S_{cd} = 0 \\ \\ \dfrac{Z_0}{2}\dfrac{S_{dd}+S_{cc}+1+|S|}{1-|S|+S_{dd}-S_{cc}} & \text{Otherwise} \end{cases}. \tag{2.33}$$

At this point, a set of different expressions for $\Gamma_d(\Gamma_c)$ and $Z_d(Z_c)$ have been obtained through driving a two-port device with different standard mixed-mode loads. As it has been previously shown, these expressions can be applied to non-symmetrical two-port devices. However, it is important to notice that each of these expressions are only valid for a specific boundary conditions which are summarized in Fig. 2.5.

2.4 A Z-parameter approach

In the previous sections, the expressions for the input reflection coefficient $\Gamma_d\,(\Gamma_c)$ and its corresponding impedance $Z_d\,(Z_c)$ were found by using mixed-mode S-parameters. Since voltages and currents are hard to measure in radio frequency's world, S-parameters, in it standard or mixed-mode presentation, are the best instrument to describe any lineal systems. However, other classical representation as ABCD-, Z- or Y-parameters still hold on and, specially for those who come from low frequency world, they still represent the most widespread tool. For this reason, at this point, it is interesting to obtain some of the found expressions in terms of Z-parameters, in order to demonstrate that no matter which representation is used, that the presented theory is perfectly consistent. Thus, from a lumped circuit point of view, Fig. 2.6 shows the actual arrangement for measuring a two-port device. Here, the transmission lines connecting VNA and DUT are of zero length.

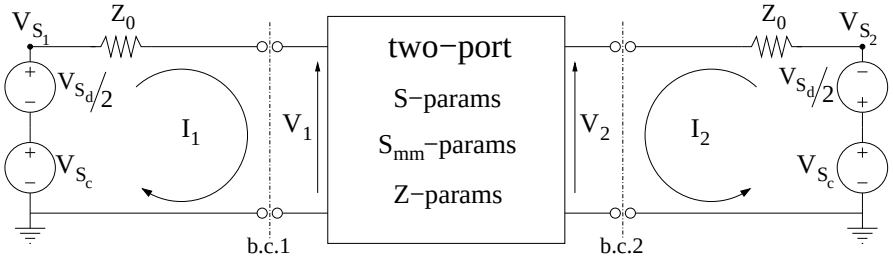

Fig. 2.6 Lumped representation of a two-port VNA.

As far as mixed-mode power waves and signals are concerned, voltage sources V_{S_1} and V_{S_2} have been substituted by their equivalent common-mode $V_{S_c} = \frac{1}{2}\,(V_1 + V_2)$ and differential mode $V_{S_d} = (V_1 - V_2)$ voltage sources. Now, one can define an equivalent differential(common)-mode impedance response by using the superposition principle. Nulling V_{S_c} sources, the differential equivalent impedance Z_d is defined as the following ratio

$$Z_d = \frac{V_d}{I_d} = \frac{V_1 - V_2}{\dfrac{1}{2}(I_1 - I_2)} \tag{2.34}$$

where V_d and I_d have been chosen according to Bockelman's definition [3]. Taking into account that this driving mode sets once again the boundary condition $a_2 = -a_1 = \frac{1}{\sqrt{2}} a_{dm}$, voltages and currents at the input ports can be expressed in terms of S_{mm} as

$$V_i = \sqrt{Z_0}\,(a_i + b_i) = \pm\sqrt{\frac{Z_0}{2}}a_{dm}\,(1 + S_{dd} \pm S_{cd})$$
$$I_i = \frac{1}{\sqrt{Z_0}}(a_i - b_i) = \pm\frac{1}{\sqrt{2Z_0}}a_{dm}\,(1 - S_{dd} \mp S_{cd}) \tag{2.35}$$

where the upper and lower signs hold for port 1 and port 2, respectively. Not surprisingly, replacing (2.35) in (2.34), the value of Z_d is given by (2.1) that agrees with the formalism derived in the previous sections. The same procedure can be used for the evaluation of the common-mode impedance response Z_c defined as

$$Z_c = \frac{V_c}{I_c} = \frac{\frac{1}{2}(V_1 + V_2)}{I_1 + I_2}. \tag{2.36}$$

By nulling both V_{S_d} voltage sources, $a_2 = a_1 = \frac{1}{\sqrt{2}}a_{cm}$ holds; thus, voltages and currents at the input ports, in terms of S_{mm}, are given by

$$V_i = \sqrt{Z_0}\,(a_i + b_i) = \sqrt{\frac{Z_0}{2}}a_{cm}\,(1 + S_{cc} \pm S_{dc})$$
$$I_i = \frac{1}{\sqrt{Z_0}}(a_i - b_i) = \frac{1}{\sqrt{2Z_0}}a_{cm}\,(1 - S_{cc} \mp S_{dc}) \tag{2.37}$$

Replacing (2.37) in (2.36), the value of Z_c is given by 2.26. Clearly, the impedance definitions (2.1) and (2.26) are consistent with the bilinear impedance transformation of S_{dd} and S_{cc}. Hence, Z_d and Z_c calculated are equivalent to Z_{dd} and Z_{cc} of a Z-parameter matrix. Also notice that, a lumped representation rides to equivalent expressions that transmission lines one, whenever electromagnetic length is considered zero.

However, as it has been previously mentioned, the key point is to recognize that none of the described excitation methods can drive the two-port as a one-port device. A one-port is topologically characterized by the existence of two nodes at its interface, i.e. a reference node and an input node, where a single transmission line is connected at. Nonetheless, the topology of the interfaces between the VNA and the DUT, i.e. b.c. 1 and b.c. 2 in Fig. 2.6, is formed by three electrical nodes due to the fact that two uncoupled (or coupled) transmission lines are involved in the propagation of a differential(common)-mode power wave. In order to force the driving as a one-port device, one of the three interface nodes of the two-port must be somehow removed. In doing so, the previous boundary conditions at b.c. 1 and b.c. 2, which are given in Fig. 2.5, do change. As a major consequence, the impedance definitions (2.1) and (2.26) are not consistent with the actual boundary condition that must be applied.

2.4.1 Differential one-port device

A two-port device is driven differentially as a one-port if the power source is applied between both input nodes setting one of them as the reference of the other, i.e. the power source is floating (purely differential). According to this definition, the equivalent electrical circuit shown in Fig. 2.7 can be drawn.

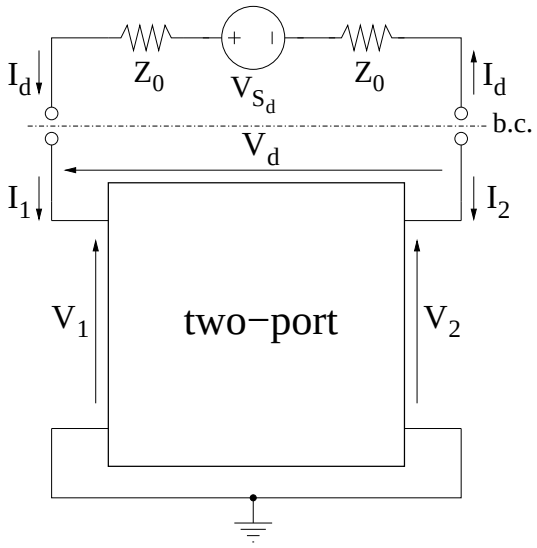

Fig. 2.7 Differential excitation of a two-port device as an one-port.

The voltage dropped across the input ports is V_d, which is the voltage difference $V_1 - V_2$. V_1 and V_2 are measured according to their own reference node that now is an internal node of the DUT. Under this kind of excitation, the associated boundary condition is set by the current I_d flowing from the source into the port, i.e.

$$I_1 = -I_2 = I_d. \tag{2.38}$$

In addition, notice that (2.38) imposes that the common-mode current $I_c = I_1 + I_2$ is always zero. From the point of view of the common-mode, this condition is equivalent to an open circuit $(I_c = 0)$ because there is no impedance connecting the reference of the source with the reference of the device. Once the boundary condition has been fixed, the differential impedance Z_d can be calculated as the ratio of V_d over I_d. Using the Z-parameters description of the two-port

$$\begin{pmatrix} V_1 \\ V_2 \end{pmatrix} = \begin{pmatrix} Z_{11} & Z_{12} \\ Z_{21} & Z_{22} \end{pmatrix} \begin{pmatrix} I_1 \\ I_2 \end{pmatrix} \tag{2.39}$$

and replacing (2.38) in (2.39), it is straight forward to find that $Z_d = \frac{(V_1 - V_2)}{I_d}$ is given by

$$Z_d = Z_{11} + Z_{22} - Z_{12} - Z_{21} \tag{2.40}$$

To compare with, it is interesting to find the value of Z_d defined by (2.34). Taking as a reference the schematic in Fig. 2.6, by nulling V_{s_c}, the mesh equations governing the behavior of the circuit are written as follows

$$\begin{pmatrix} \frac{V_{S_d}}{2} \\ \frac{-V_{S_d}}{2} \end{pmatrix} = \begin{pmatrix} Z_0+Z_{11} & Z_{12} \\ Z_{21} & Z_0+Z_{22} \end{pmatrix} \begin{pmatrix} I_1 \\ I_2 \end{pmatrix}. \tag{2.41}$$

Solving first for I_1 and I_2, their difference $I_1 - I_2$ is

$$I_1 - I_2 = \frac{\frac{V_{S_d}}{2}}{det\overline{Z'}}(2Z_0 + Z_{11} + Z_{22} + Z_{12} + Z_{21}) \tag{2.42}$$

where $det\overline{Z'}$ is the determinant of the mesh matrix in (2.41). The difference $V_1 - V_2$ can be written as

$$V_1 - V_2 = \left(\frac{V_{S_d}}{2} - Z_0 I_1\right) - \left(-\frac{V_{S_d}}{2} - Z_0 I_2\right) =$$

$$= \frac{\frac{V_{S_d}}{2}}{det\overline{Z'}}\left[2det\overline{Z} + Z_0\left(Z_{11} + Z_{22} - Z_{12} - Z_{21}\right)\right] \tag{2.43}$$

where $det\overline{Z}$ is the determinant of the Z parameters matrix of the two-port. Making use of (2.40), the value of Z_d is given by

$$Z_{dd} = \frac{4\ det\overline{Z} + 2Z_0 Z_d}{2Z_0 + Z_{11} + Z_{22} + Z_{12} + Z_{21}}. \tag{2.44}$$

Under symmetry conditions, i.e. $Z_{11} = Z_{22}$ and $Z_{12} = Z_{21}$, (2.44) reduces to (2.40) as expected. However, the definition of Z_d depends on the impedance of the media Z_0, but when the two-port is symmetric. Its range of variation is bounded between a pure differential voltage signal mode excitation ($Z_0 = 0$) and, by using the Norton's equivalent for both sources, a pure differential current signal mode excitation ($Z_0 \to \infty$). For the first bounded value, Z_d reads as

$$Z_{dd}\left(Z_0 = 0\right) = \frac{4det\overline{Z}}{Z_{11} + Z_{22} + Z_{12} + Z_{21}}; \tag{2.45}$$

and, for the second one,

$$Z_{dd}\left(Z_0 \to \infty\right) = Z_d. \tag{2.46}$$

Interestingly, (2.46) matches the definition of Z_d because, under the condition $Z_0 \to \infty$, no common-mode current can flow, forcing the condition $I_1 = -I_2$. At this point, one could be worried about the differences in the impedance definitions given above. As it has been previously stated, the important point is to keep in mind that an impedance is the ratio of a voltage over a current once a boundary condition has been established. Different boundary conditions must lead to different impedance values: Z_d and $Z_{dd}\,(Z_0 \to \infty)$ are related to von Neumann's type; $Z_{dd}\,(Z_0 \to 0)$, to Dirichlet's type; and Z_{dd} is a mixed boundary type.

2.4.2 Common-mode one-port device

For the common-mode case, the two-port is driven as a one-port device when both input nodes are connected to a power source having an output impedance $\frac{Z_0}{2}$. The situation is depicted in Fig. 2.8. Topologically, both input nodes have collapsed into a single node connected to the power source. Now, the boundary condition that sets this driving mode is given by

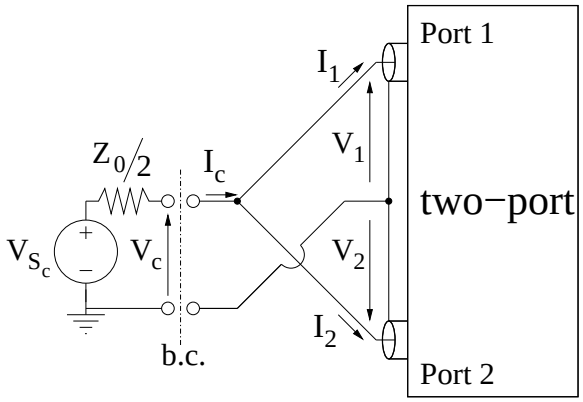

Fig. 2.8 Common-mode excitation of a two-port device as an one-port.

$$V_1 = V_2 = V_c. \tag{2.47}$$

instead of (2.38). Of course, (2.47) imposes $V_d = V_1 - V_2 = 0$, i.e., the differential mode is shorted. The common-mode current that flows from the source is $I_c = I_1 + I_2$.

Looking into the device, a common-mode impedance can be defined as $Z_c = \frac{V_c}{I_c}$ that leads to the next expression in terms of Z parameters

$$Z_c = \frac{det\overline{Z}}{Z_{11} + Z_{22} - Z_{12} - Z_{21}} = \frac{det\overline{Z}}{Z_d}. \tag{2.48}$$

Notice the fact that $det\overline{Z} = Z_c Z_d$. To compare with, the value of the common-mode impedance Z_{cc} is given by

$$Z_{cc} = \frac{Z_c Z_d + \frac{Z_0}{2}(Z_{11} + Z_{22} + Z_{12} + Z_{21})}{2Z_0 + Z_d}. \tag{2.49}$$

If symmetry conditions are applied to (2.49), Z_{cc} and Z_c are equal. As in the case of Z_{dd}, the value of Z_{cc} depends on Z_0 and it is bounded between a pure common-mode voltage excitation $Z_{cc}(Z_0 \to 0)$

$$Z_{cc}(Z_0 = 0) = Z_c \tag{2.50}$$

and a pure common-mode current excitation $Z_{cc}(Z_0 \to \infty)$

$$Z_{cc}(Z_0 \to \infty) = \frac{1}{4}(Z_{11} + Z_{22} + Z_{12} + Z_{21}). \tag{2.51}$$

Not surprisingly, $Z_{cc}(Z_0 \to 0)$ reduces to Z_c because in both (2.47) holds.

2.5 Power delivered in a mixed-mode load

As it has been mentioned earlier in this chapter, most of the current RFICs are designed to work in differential configuration. Differential topologies are more immune to noise coupling and show less source degeneration (ideally zero), thus those benefits make them very desirable. Within this framework, two-port devices play an important role, since they can be considered as terminations. The two-port represented has one physical mixed-mode port (i.e. two single-ended ports and a common-ground reference), which allows the propagation of a differential and a common-mode power wave. Due to this fact, from a topological point of view, and avoiding how the differential signal is generated (either a Wilkinson or any other circuit), when the two-port is tied to a power source, the power source presents a differential and common-mode source impedance to the two-port device. Indeed, this configuration can be drawn as in Fig. 2.9 where the mixed-mode port has been split in a differential and common-mode ports. In this general case, the common-mode source impedance can be any value, as instance, it can map all the driven conditions in Fig. 2.5, from an open impedance to a short or a matching condition. Independently how the source is designed, we want to know the power delivered into the two-port load; thus, let assume the case represented in Fig. 2.9 where a differential source supplies a differential power wave into a two-port termination, meanwhile the source also loads the common-mode port with an impedance Z_s^c. Defining the power delivered in the load in the classical way $P = 1/2(vi^*)$ where voltage and current have already been defined as $v_d = v_1 - v_2$ and $i_d = 1/2(i_1 - i_2)$, power can be written in terms of the incident and reflected mixed-mode power waves as follows

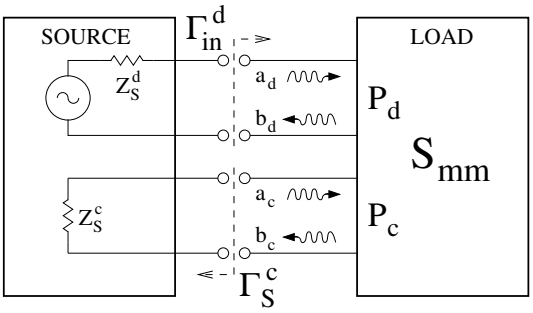

Fig. 2.9 Excitation of a two-port device which is acting as a termination.

$$P_d = \frac{1}{2} v_d i_d^* = \frac{1}{2}\left(|a_d|^2 - |b_d|^2\right) = \frac{1}{2}|a_d|^2\left(1 - |\Gamma_d|^2\right). \tag{2.52}$$

In a general case, some of the power going into the two-port will be transformed in a common-mode reflected power wave, b_c, which will be dissipated, in part, in the common-mode source impedance. This power can be written by means of the common-mode voltage and current which read as $v_c = 1/2\,(v_1 + v_2)$ and $i_c = (i_1 + i_2)$. Thereby, the power dissipated in the common-mode source impedance is given by

$$P_s^c = \frac{1}{2} v_c i_c^* = \frac{1}{2}\left(|b_c|^2 - |a_c|^2\right) = \frac{1}{2}|b_c|^2\left(1 - |\Gamma_s^c|^2\right). \tag{2.53}$$

Consequently, the total power dissipated in the two-port device, P_L^d, is P_d less P_s^c, since this last term is indeed dissipated in the source, and it can not be computed as part of P_L^d. From (2.52) and (2.53), the whole available power in the source, $1/2\,|a_d|^2$, is completely dissipated in the two-port depending on the driving conditions and characteristics of the device. In fact, the next cases can happen

i. If the two-port device is symmetric, Γ^d equals S_{dd} and there is not common-mode generated (i.e. b_c equals zero). As a result, the total delivered power in the load is given by

$$P_L^d = P^d - P_s^c = \frac{1}{2}|a_d|^2\left(1 - |S_{dd}|^2\right), \tag{2.54}$$

which coincides with the available power in the source only if the two-port device is perfectly matched and S_{dd} equals zero. Notice that in this case, the common-mode impedance at the source does not have any implication in the delivered power.

ii. If the two-port device is not symmetric and the common-mode impedance in the source is matched (i.e. Γ_s^c equals zero), part of the delivered power is dissipated at the source and the total power is given by

$$P_L^d = P_d - P_s^c = \frac{1}{2}|a_d|^2\left(1-|\Gamma_d|^2\right) - \frac{1}{2Z_s^c}|b_c|^2. \tag{2.55}$$

Notice that, the only way that the whole power is delivered in the two-port device is again when the device is symmetric and matched. Otherwise, even in the case when Γ_d equals zero, the total power can't coincide with the available power since part is being dissipated at the source. Also note that, if the two-port device is a pure reactance (i.e. no power can be dissipated in it), (2.55) still applies since, in this case, b_c equals zero because of the fact that a pure reactance can only be perfectly symmetric; at the end both terms in (2.55) are zero.

iii. If the two-port device is not symmetric and Γ_s^c equals ± 1 (i.e. the common-mode source impedance is a pure reactance), no power can be dissipated in Z_s^c even though the asymmetry condition. Therefore, the power delivered to the two-port device is given by

$$P_L^d = \frac{1}{2}|a_d|^2\left(1-\left|S_{dd} \pm \frac{S_{dc}S_{cd}}{1\mp S_{cc}}\right|^2\right). \tag{2.56}$$

Notice that, since there cannot be dissipated power in Z_s^c, the delivered power wave is reflected back to the source through the device, and it is dissipated in the differential source impedance, Z_s^d. From Γ_d, the differential reflected power wave, b_d, can be obtained as follows

$$b_d = \left\{S_{dd} \pm \frac{S_{dc}S_{cd}}{1\mp S_{cc}}\right\} a_d. \tag{2.57}$$

The first term in (2.57) is the portion of power from the differential input power that has been reflected back by the two-port itself. Likewise, the second term is the reflected common-mode power wave that has been reflected by Z_s^c and transformed to a differential power wave again by the two-port device. Also notice that, from (2.56), even in the case when S_{dd} equals zero, the delivered power in the two-port device cannot achieve the available power at the source because of the second term in (2.57). At this point, this result should not be surprising: Γ_d can not be mistaken with S_{dd}, thereby, matching condition happens when $\left(\Gamma_s^d\right)^*$ equals Γ_d instead of S_{dd}. In principle, from (2.56), the only way that the whole available power in the source is dissipated in the two-port device is when the device is symmetric and matched.

Indeed, referring to the case from i to iii, the two-port device can be matched through a matching network in order to deliver the maximum power into the load. Thus, Fig. 2.10 shows the differential source and load represented before but connected through a full differential matching network. As it can be seen, the matching network is a four-port device that can be described by means of mixed-mode scattering parameters. Likewise in the single-ended case, the impedance matching is a synthesis problem where a set of different components must be combined for imple-

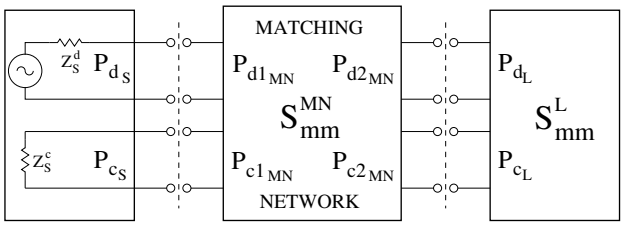

Fig. 2.10 Matching adaptation of a mixed-mode two-port device.

menting an optimized matching network. Those components are arranged in a way that the main objective is to transform the input impedance of the device to obtain the conjugate impedance of the power source or sometimes another impedance of interest.

Thereby, in case i, thanks to two-port device symmetry, independently of what is connected in the common-mode, $\left(\Gamma_s^d\right)^*$ must equal S_{dd}. In this case, maximum power delivered in the load coincides with available power in the source. Likewise, in case iii, the whole available power in the source can be dissipated in the load. However, in this case $\left(\Gamma_s^d\right)^*$ must equal Γ_d meanwhile Γ_s^c equals ± 1. Thus, the second term in (2.56) equals zero and it can be seen that power delivered in the two-port device coincides with available power wave in the source.

Unlike this two last cases, in case ii, available power in the source can not be achieved. Even though, $\left(\Gamma_s^d\right)^*$ equals Γ_d, it can be seen that the second term in (2.55) can not be neglected and part of the available power is dissipated in the common-mode source impedance. Thereby, unlike one might think, impedance matching of all the ports (i.e. differential(common)-mode ports in the case of a two-port device) do not lead to dissipate the available power in the source and some portion is dissipated in the common-mode source impedance. Hence, for a non-symmetric device, the only way to dissipate the available power is by connecting a pure reactance in the common-mode source impedance.

It is important to notice that there can be other restrictions on the optimization of the matching network (minimize area, bandwidth, quality factor or number of components...). Then, this synthesis problem can be approach by solving a set of system of equations which, even in the single-ended case, are difficult to deal with resulting in an unsuitable method. Thereby, facing the problem in this way is overwhelming. However, likewise it is done in the single-ended case, the practical procedure goes through the concatenation of single passive components, step by step, following a path on the impedance(admittance) Smith's chart which drives the impedance transformation to the desired value. Moreover, due to the fact that the matching network is full differential device, other components different from inductors and capacitors can be used, as instance transformers, coupled transmission lines and so on. Since the synthesis of full differential matching networks implies to obtain the input(output) reflection coefficient of a four port device, this topic will be treated in the next chapter, where the S-parameter theory for an n-port device is extended. However, with the expression obtained up to this point, one can solve interesting

misunderstandings, as instance, the characterization of an asymmetric inductor in terms of mixed-mode S-parameters.

2.6 Practical case

An integrated inductor can be considered as a two-port device similar to the one on Fig. 2.2. Thus, the former theory can be applied to the evaluation of the quality factor, Q, of inductors. Q is defined as a ratio of the stored reactive energy over the energy loss evaluated in one cycle. However, this definition is quite subtle because the stored energy is actually dependent on the shape of electromagnetic fields around the component. These fields are related to the geometry, including layout elements nearby; but, most important, to the way in which the inductor is excited in [21, 22, 23]. Noticing the benefit of exciting inductors differentially, Rabjohn introduced the use of symmetrical shapes in the implementation of fully differential RFICs substituting traditional spiral ones [24, 25]. Thus, for any inductor, Q is given by

$$Q = \frac{Im\{Z_d\}}{Re\{Z_d\}}, \tag{2.58}$$

where, as it has been previously demonstrated, for an ideal symmetric inductor Z_d results in Z_{dd}. However, even though a symmetrical shape is used in their implementation, symmetry is not always guaranteed. Indeed, cross-bridges sections or layout asymmetries at the surrounding area of an inductor can break the symmetry of its own electromagnetic fields. Furthermore, there is still many situations in which spiral inductors can be preferred over symmetrical ones, e.g. when one of the terminal of the inductor is grounded, or when area reduction prevails over symmetry [26, 27]. For these cases, the choice between symmetric and spiral topologies is currently set through the comparison of the Q factor when driving the device differentially. Thereby, it is important to find the correct definition of Q for both topologies, i.e. it must be avoided that any inductor shape benefits itself from the definition of the Q factor. To proceed with, the previously developed theory and concepts provide a correct framework for such comparison.

Fig. 2.11 shows two inductors using different topologies, symmetric and spiral, that have been synthesized using layout optimization techniques [28] for a given application in the frequency range of 2.45 GHz using a $0.35\mu m$ CMOS technology. Their geometrical characteristics are summarized in Table 2.1. Notice that both geometries are quite similar, thus a similar Q factor behavior should be expected. Both layouts have been simulated with MoMemtum, a planar solver from Agilent Technologies, obtaining the two-port single-ended S-parameter matrix over a frequency range beyond the Self Resonance Frequency (SRF). The obtained S-parameters are later mathematically converted to mixed-mode S-parameters matrix description [6].

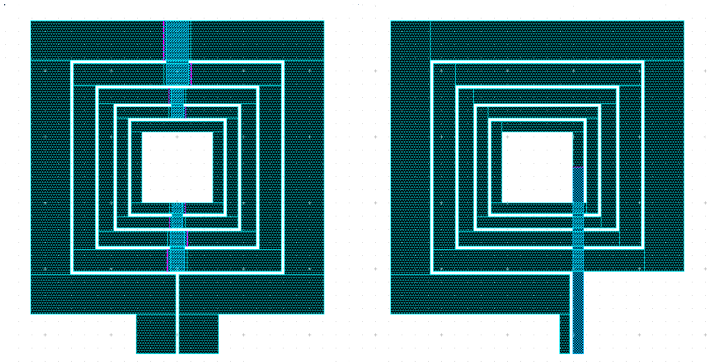

Fig. 2.11 Symmetric and spiral optimazed inductors layout.

Table 2.1 Geometrical characteristics of both inductors.

Number of turns	5
Inner diameter $[\mu m]$	54
Spacing between turns $[\mu m]$	2.5
Width of the first turn (inner turn) $[\mu m]$	7.8
Width of the second turn $[\mu m]$	8.6
Width of the third turn $[\mu m]$	11.1
Width of the fourth turn $[\mu m]$	16.8
Width of the fifth turn (outer turn) $[\mu m]$	30

When exciting symmetric inductors differentially, non reflected common-mode power wave exist which means that the response of the component is independent of the common-mode load Γ_L^c, as it has been previously demonstrated. Then, Z_d equals Z_{dd} and (2.2) and (2.58) are equivalent. Fig. 2.12 shows a plot of the Q factor value for the previous given symmetrical inductor when loaded with $\Gamma_L^c = 0$, 1 and -1. As expected, all the cases give the same Q factor behavior.

On the contrary, the differential excitation of a spiral inductor allows the existence of a common-mode reflected power wave. Therefore, the response of the device is dependent on the value of the common-mode load Γ_L^c. Using the same common-mode load conditions as in the previous symmetrical case (i.e. open, short and match), Fig. 2.13 shows the behavior of Q for the non-symmetric inductor. It is worth noting that differences larger than a 10% can be obtained depending on the boundary condition, i.e. the value of Q can be boosted just because of the definition of Q itself. Therefore, once an inductor is chosen, the main issue is to identify the correct boundary conditions which lead to the adequate value of Q.

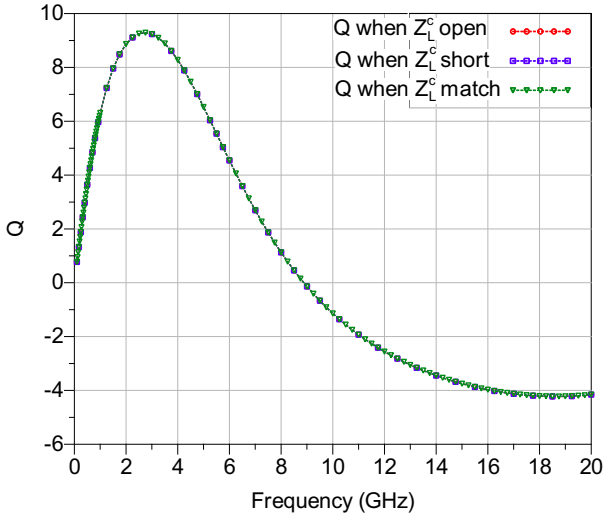

Fig. 2.12 Quality factor vs. frequency for a symmetric inductor using (2.58) when $Z_L^c = Z_0/2$ (match), open, short.

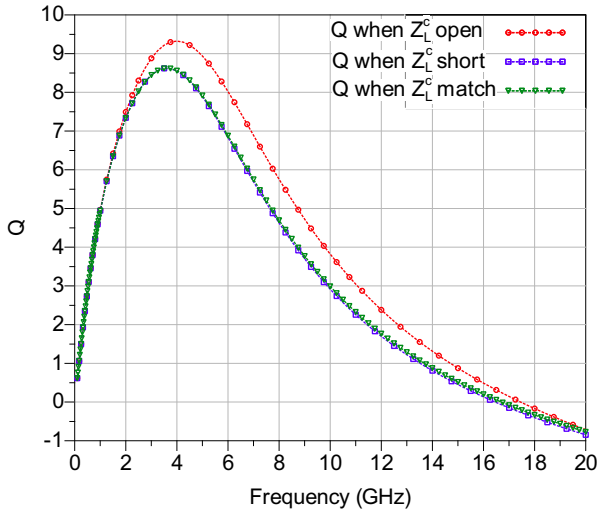

Fig. 2.13 Quality factor vs. frequency for an asymmetric inductor using (2.58) when $Z_L^c = Z_0/2$ (match), open, short.

2.7 Conclusions

The theory of mixed-mode scattering parameters has been extended not only to symmetrical devices, but to non-symmetrical or actual devices, finding a general

expression for $\Gamma_d(\Gamma_c)$ that resembles the well-known expressions of $\Gamma_{in}(\Gamma_{out})$ for a single-ended two-port device. It has also been shown that the former particular cases of the driving of a two-port device are reduced to the application of a short, open and matched mixed-mode load conditions on the general expression of $\Gamma_d(\Gamma_c)$. Moreover, such definitions allow to obtain $Z_d(Z_c)$ in terms of S_{mm}. An analytic connection between scattering-parameters description in both versions, through the use of S-parameters and S_{mm}, and lumped elements description has naturally been used toward the attainment of these expressions. As a practical case, the Q value for symmetrical and non-symmetrical inductors has been obtained using the definition of Z_d, illustrating the differences when considering different boundary conditions.

2.8 Acknowledgements

This work was supported in part by the Spanish Ministry of Innovation and Science (with support from the European Regional Development Fund) under contract TEC2010-14825/MIC and TEC2010-21484; and in part by the Andalusian Regional Council of Innovation, Science and Enterprise under contract TIC-2532 and with the support of the Department of University, Research and society of information of Government of Catalonia. I would like to thank Javier and Jose María for the help and support in the development of this Chapter. Also, I would like to thank Elisenda and Reinier, from the University of Seville, for the "multiple reviews" they had to do and the valuable help in the synthesis of inductors. Finally, I would like to thank Prof. Mohammed Ismail from Ohio State University, for his warm hospitality during his visit to the ElectroScience Laboratory in OSU.

References

1. Y. Amin and H. Tenhunen. Development and analysis of flexible UHF RFID antennas for 'green' electronics. *Progress In Electromagnetics Research*, 130:1–15, 2012.
2. S.-M. Wu, C.-T. Kuo, P.-Y. Lyu, Y. L. Shen, and C.-I. Chien. Miniaturization design of full differential bandpass filter with coupled resonators using embedded passive device technology. *Progress In Electromagnetics Research*, 121:365–379, 2011.
3. D.E. Bockelman and W.R. Eisenstadt. Combined differential and common-mode scattering parameters: theory and simulation. *Microwave Theory and Techniques, IEEE Transactions on*, 43(7):1530 –1539, jul 1995.
4. D.E. Bockelman and W.R. Eisenstadt. Combined differential and common-mode analysis of power splitters and combiners. *Microwave Theory and Techniques, IEEE Transactions on*, 43(11):2627 –2632, nov 1995.
5. Skyworks Application Note. *"Matching Differential Port Device"*. Skyworks Solutions, Inc., October 2009.
6. M. Danesh. Monolithic inductors for silicon radio frequency integrated circuits. M.A.Sc.Thesis, Dept. Elect. Comput. Eng., Univ. Toronto, Toronto, ON, Canada, 1999.
7. M. Danesh and J.R. Long. Differentially driven symmetric microstrip inductors. *Microwave Theory and Techniques, IEEE Transactions on*, 50(1):332–341, jan 2002.

8. S. K. Kuo, S. L. Chen, and C. T. Lin. An accurate method for impedance measurement of RFID tag antenna. *Progress In Electromagnetics Research*, 83:93–106, 2008.
9. Danesh, M. and Long, J.R. Authors' reply. *Microwave Theory and Techniques, IEEE Transactions on*, 55(4):809–810, april 2007.
10. Meys, R. and Janssens, F. Measuring the impedance of balanced antennas by an S-parameter method. *Antennas and Propagation Magazine, IEEE*, 40(6):62–65, dec 1998.
11. Xianming Qing and Zhi Ning Chen. Impedance characterization of RFID tag antennas and application in tag co-design. *Microwave Theory and Techniques, IEEE Transactions on*, 57(5):1268 –1274, may 2009.
12. Lutz Konstroffer. Finding the reflection coefficient of a differential one-port device. *RF Semiconductor*, 1999.
13. Drakaki, M., Hatzopoulos, A.A., and Siskos, A. CMOS inductor performance estimation using Z- and S-parameters. *Circuits and Systems, 2007. ISCAS 2007. IEEE International Symposium on*, pages 2256 – 2259, 2007.
14. Robert E. Collin. *Foundations for Microwave Engineering*. Wiley-IEEE Press, 2 edition, December 2000.
15. C.H. Liang, Y. Shi, and T. Su. S parameters theory of lossless block network. *Progress In Electromagnetics Research*, 104:253–266, 2010.
16. Stephane Wloczysiak. *Match the ports of differential devices*. Microwaves and RF, ed online id22407 edition, February 2010.
17. D.E. Bockelman and W.R. Eisenstadt. Pure-mode network analyzer for on-wafer measurements of mixed-mode S-parameters of differential circuits. *Microwave Theory and Techniques, IEEE Transactions on*, 45(7):1071 –1077, jul 1997.
18. Zwick, T. and Pfeiffer, U.R. Pure-mode network analyzer concept for on-wafer measurements of differential circuits at millimeter-wave frequencies. *Microwave Theory and Techniques, IEEE Transactions on*, 53(3):934 – 937, march 2005.
19. Xianming Qing and Zhi Ning Chen. Comments on "comments on 'measuring the impedance of balanced antennas by an S-parameter method'". *Antennas and Propagation Magazine, IEEE*, 52(1):171 –172, feb. 2010.
20. Kaldjob, E., Geck, B., and Eul, H. Comments on "Measuring the impedance of balanced antennas by an S-parameter method". *Antennas and Propagation Magazine, IEEE*, 50(6):113–114, dec. 2008.
21. S. J. Pan, L. W. Li, and W. Y. Yin. Performance trends of on-chip spiral inductors for RFICs. *Progress In Electromagnetics Research*, 45:123–151, 2004.
22. Tomas Carrasco Carrillo, Jose Gabriel Macias-Montero, Aitor Osorio Marti, Javier Sieiro Cordoba, and Jose Maria Lopez-Villegas. CMOS single-ended-to-differential low-noise amplifier. *Integration, the VLSI Journal*, 42(3):304 – 311, 2009. Special Section on DCIS2006.
23. L. Aluigi, F. Alimenti, and L. Roselli. Automatic design and 3d electromagnetic simulation of sub-nh spiral inductors. *Progress In Electromagnetics Research Symposium Proceedings*, pages 20–23, 2011.
24. G. G. Rabjohn. Monolithic microwave transformers. M.Eng. thesis, Carleton University, Ottawa, ON, Canada, April 1991.
25. Y. Zheng and C. E. Saavedra. Frequency response comparison of two common active inductors. *Progress In Electromagnetics Research Letters*, 13:113–119, 2010.
26. Eroglu Abdullah. Planar inductor design for high power applications. *Progress In Electromagnetics Research B*, 35:53–67, 2011.
27. R. Wang, J. Xu, C.-L. Wei, M.-Y. Wang, and X.-C. Zhang. Improved extraction of coupling matrix and unloaded Q from S-parameters of lossy resonator filters. *Progress In Electromagnetics Research*, 120:67–81, 2011.
28. Jose M. Lopez-Villegas, Josep Samitier, Charles Cane, Pere Losantos, and Joan Bausells. Improvement of the quality factor of RF integrated inductors by layout optimization. *Microwave Theory and Techniques, IEEE Transactions on*, 48(1):76–83, January 2000.

Chapter 3
Power match theory of an n-port device

Abstract An n-port device can be completely characterized by means of the generalized scattering parameters which naturally describe the physical behavior of balanced devices. Therefore, it would be also desirable that the classical power match methodology, as well as the microwave amplifier design's formalism, could be expressed in terms of these parameters as it is classically done in terms of S_{ij} for a two-port device. Thus, in this chapter, the formalism for a n-port device and specially for three- and four-port devices is developed. This formalism is independent of any existing power-mode conversion and leads to obtain power gain, stability and mismatching circles definitions in their most general form.

3.1 Introduction

Radio frequency and microwave circuits are very varied. The large number or different applications, functionality and frequencies lead to the existence of multiple configurations, forms and shapes i.e. most of the time to devices with a varied number of ports. As it is well known, a device with n-ports is completely characterized by its standard *nxn* S-parameters matrix. As instance, in the case of an antenna array, each diagonal term of the corresponding S-parameter matrix provides the input reflection coefficient of the individual antenna whereas, the cross-terms describe the possible coupling between an antenna and the rest of the array. Extending this illustrative example, if one thinks in a practical connection of such device, the multiple ports can be accessible through single-ended lines e.g., in a planar technology, by micro-strip lines. Thereby, for a given frequency and if geometric axes planes are properly chosen, a unique mode of propagation is expected. Furthermore, within the mentioned antenna array, some of the antennas can be differential. As we have discussed in Chapter 2, these devices will be formed by three physical ports and, following the example, it will be accessible e.g. by a two strip coupled transmission line. Unlike the rest of antennas, there will usually exist multiple modes even in static cases. Even though they can be perfectly described by its standard S-

parameters matrix, they are better described in terms of mixed-mode S-parameters. In summary, our antenna array is formed by a matrix which shares standard and mixed-mode S-parameters. The problem can still be more complex if each antenna is designed for a different application and they are referred to a different normalized impedance.

Putting aside the antenna array example, a full differential amplifier represents an example of a four port device. Again, it can be perfectly described by its standard S-parameter matrix. However, for simplicity, the design of this kind of amplifiers is commonly dealt by splitting the amplifier in two branches through its symmetry axis. Then, each branch is considered as a single-ended amplifier and the classical methodology for the design of amplifiers holds, as it was exemplified in Section 1.4.3. Of course, depending on the symmetry of the device, this approach can result in a small error, though it keeps being formally incomplete. In fact, as we have seen in the case of a two-port device, this approach implies to disregard the existence of any common-mode conversion. Thus, if symmetry is not guaranteed, the common-mode is simply dismissed during the design process and it can not be minimized or even simply quantified. As an alternative to the exemplified design methodology, but with the main goal of demonstrating mixed-mode S-parameters formalism, Bockelman re-wrote in [1] the classical two-port power match expressions using a mixed-mode representation. His work starts from an ideally symmetric four port device, i.e. there is no mode conversion and $S_{DC}\,(S_{CD})$ equals zero. As it will be also deduced in this chapter, this assumption allows to split the four-port mixed-mode S-parameter matrix in two separated two-port problems. After this simplification, Bockelman simply re-writes the classical expressions shown in Section 1.4.3 in two sets of equations for each of the existing modes i.e. S_{DD} and S_{CC}. This method and the explained in the previous paragraph suffer from the same problem: if symmetry is not guaranteed, the mode conversion is simply dismissed. Certainly, Bockelman's approach represent one step forward in differential formalism, but it can not be considered as a complete methodology for a real case where mode conversion can exist. Moreover, as it has been mentioned, Bockelman's work only applies for a four-port device where all ports are considered mixed-mode ports and cannot be directly extended to n-port devices.

Within this framework, the aim of this chapter is to describe the theory of power match in electrical and electronics systems composed by an n-port device. Since an n-port device can be formed by single-ended and mixed-mode ports, in Section 3.2 the generalized S-parameters matrix is described based on Ferrero and Pirola work [2]. At this point, it is interesting to compare the use of pseudo-power waves and Kurokawa's power waves for completeness of the theory developed in the previous chapters. Furthermore, respective generalized S-parameters matrices are found for the case of a single-ended to differential and a full-differential device in terms of standard S-parameters. Using this generalized S-parameters definition, a new expression for the input(output) reflection coefficient for a n-port is found in Section 3.3. One can expect that, most of the methodologies and expressions are rather an extension of the existing counterpart for the single-ended case. Following the same path, another interesting analytical system formalism which can be reformu-

lated is the signal flow graphs and Masons' rules [3, 4]. Thereby, Section 3.4 briefly review the well-known Masons' rules but to be used with generalized S-parameters. Once most of the single-ended methodologies have been extended, the port reference impedance transformation is formulated in Section 3.5, as it was first done for standard S-parameters in Kurokawa's work [5]. The new port reference impedance transformation allows to develop the power match theory which is developed in Section 3.6. Unlike Bockelman's formalism, the new theory solves the general problem independently of the actual existing power mode conversion. Even so, in order to validate the developed expressions, they are continuously applied to a four port device and simplified to the symmetric case in order to compare with Bockelman's work. Furthermore, the new formalism also allows to obtain power gain, stability and mismatching circles definitions without any conversion-mode simplification. These concepts will be applied to the design of a single-ended to differential low noise amplifier later in Chapter 6.

3.2 Generalized mixed-mode S-parameters

An n-port device, as the described in the previous examples, can be characterized by a generalized S-parameter matrix, where the number of ports n, can be either even or odd. Furthermore, such S-parameter matrix can have an even number of ports p which are expressed in terms of mixed-mode S-parameter and n-$2p$ ports expressed in terms of standard S-parameters. This description of the device, that was first introduced in [2] by Ferrero and Pirola, allows its best physical representation, since its figures of merit are expressed on terms of those parameters which better describes its comprehension. As instance, a BalUn, which is a 3-port device, can be characterized by a generalized S-parameter matrix. In this case, the single-ended input-port is defined by a standard S-parameter whereas, the output-ports are better expressed by mixed-mode S-parameters because of its symmetrical nature. Thus, the designer can correctly define classical parameters such us the common-mode rejection ratio (CMRR), but in terms of such S-parameters which actually, better represent the behavior of the device. Thereby, Fig. 3.1 shows the representation of a n-port device where ports have been rearranged depending on device's symmetry properties. Notice that, unlike in [2], ports have also been classified as input and output ports in Fig. 3.1. This extra classification does not affect how the n-port device's S-parameter matrix can be arranged; thereby, as it is defined in by Ferrero and Pirola, the matrix reads as follows

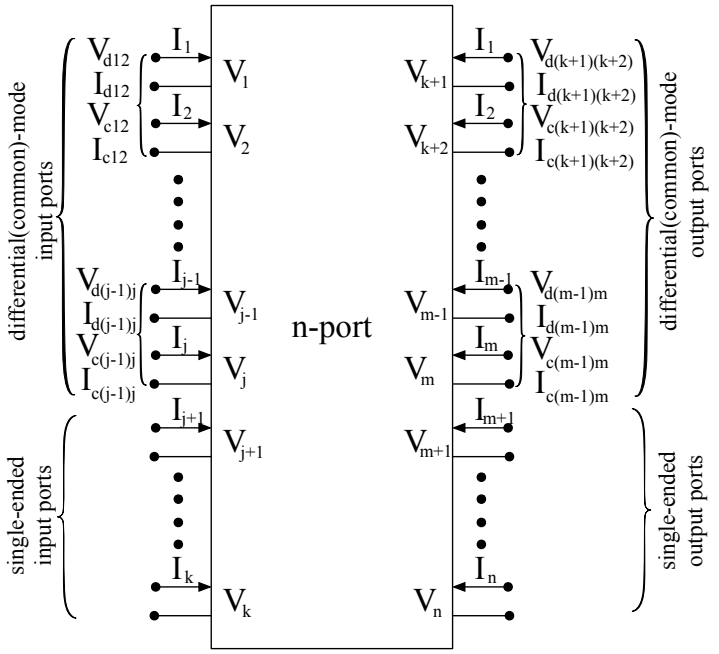

Fig. 3.1 N-port device where ports have been arranged in input(output) single-ended and differential-mode ports.

$$\overset{\circ}{S} = \begin{pmatrix} S_{dd} & S_{dc} & S_{de} \\ [p,p] & [p,p] & [p,n-2p] \\ S_{cd} & S_{cc} & S_{ce} \\ [p,p] & [p,p] & [p,n-2p] \\ S_{ed} & S_{ec} & S_{ee} \\ [n-2p,p] & [n-2p,p] & [n-2p,n-2p] \end{pmatrix}, \tag{3.1}$$

where d, c and e sub-matrix subscripts refer to the differential, common, and single-ended modes, respectively.

The symbol $\overset{\circ}{S}$ is used for the generalized S-parameter matrix i.e., $\overset{\circ}{S}$ is defined by means of pseudo-power waves. It will be shown later, that pseudo-power waves coincide with Kurokawa's power waves when line reference impedances equals Z_0, $2Z_0$ and $Z_0/2$ respectively [6]. Moreover, it can be notice that, in Fig. 3.1, each mixed-mode port has been split in a differential and a common-mode port, even though they belong to the same physical port. This topological representation helps in the mathematical development along the next sections. However, as it has been already mentioned in Chapter 2, one has to keep in mind that both differential and common-mode representations, for a given port, are interrelated; thus, whenever a second device is connected to such port, impedances in both ports get fixed simul-

taneously. Also, it is interesting to notice that (3.1) is naturally arranged in nine sub-matrices which show up the self- and cross-coupling relationship between the p mixed-mode ports and the n-$2p$ single-ended ports.

In order to give the maximum generality to $\overset{\circ}{S}$, Ferrero and Pirola's mathematical derivation is carried out with the most general definition of the S-parameters (i.e. using pseudo-power waves), allowing the use of complex S-parameter reference impedances [2]. Unlike Ferrero and Pirola's work, in Chapter 2, we have done extensible use of Kurokawa's power wave definition through the use of the following expressions

$$\begin{aligned} a_i &= \frac{V_i + Z_i I_i}{2\sqrt{|Re\{Z_i\}|}} \\ b_i &= \frac{V_i - Z_i^* I_i}{2\sqrt{|Re\{Z_i\}|}}. \end{aligned} \tag{3.2}$$

Kurokawa's power waves definition is devised to satisfy the power balance relation $|a_i|^2 - |b_i|^2$, for any value of port impedance, Z_i. This definition of power waves coincides with traveling waves' one when the reference impedance matches the characteristic impedance of a transmission line. Moreover, as it has been used in the previous chapter, reflection coefficient is defined as follows

$$\Gamma = \frac{V - IZ_{ref}^*}{V + IZ_{ref}} = \frac{Z_{load} - Z_{ref}^*}{Z_{load} + Z_{ref}}. \tag{3.3}$$

Notice that in the case of a short circuit V equals zero, thereby (3.3) results as

$$\Gamma = \frac{-Z_{ref}^*}{Z_{ref}}, \tag{3.4}$$

which equals -1 only when Z_{ref} is real. This result can be seen as a problem when one tries to represent the reflection coefficient in the Smith chart. The chart is not able to accommodate the data in this form because Smith chart depends only on the ratio Z_{load}/Z_{ref}. Of course, the problem is easily solved if the reactance part of the reference impedance is added to the load impedance; thus, reference impedance becomes real and the corresponding point on the Smith chart gives the magnitude and the phase of the power wave reflection coefficient. In any case, in the previous chapter the reference impedance has always been defined as real, thereby the definition still applies. In the other hand, since there is a infinite number of lineal transformations of V and I, one can define pseudo-power waves as follows

$$\begin{aligned} a_i &= \sqrt{|Re\{Z_i\}|}\frac{V_i + Z_i I_i}{2|Z_i|} \\ b_i &= \sqrt{|Re\{Z_i\}|}\frac{V_i - Z_i I_i}{2|Z_i|}. \end{aligned} \tag{3.5}$$

Notice that, with this description, a short can be perfectly represented in a Smith chart due to the fact that Γ depends on the quotient Z_{load}/Z_{ref} instead of Z_{load}/Z_{ref}^{*}. Also it is important to notice that, like in the power wave case, (3.5) are equivalent to traveling waves, when Z_{ref} is the characteristic impedance of a TEM transmission line. However, the simple power relation $|a_i|^2 - |b_i|^2$ can not be used and it is given by the next expression

$$P = |a|^2 \left[1 - |\Gamma|^2 - 2Im\{\Gamma\} \frac{Im\{Z_{ref}\}}{Re\{Z_{ref}\}} \right]. \tag{3.6}$$

Again, when Z_{ref} is real, the cross-term in (3.6) disappears and similarly to power waves definition, $|a_i|^2 - |b_i|^2$ is recovered.

Even though pseudo-power waves represent a more general case of Kurokawa's expressions, standard power wave is used, all across this chapter, in order to follow with the previous chapter notation. As it has been mention, Kurokawa's expressions coincides with pseudo-power waves when reference impedance is real which is the case for the purpose of this thesis. In any case, the same arrangement as in $\overset{\circ}{S}$, but using Kurokawa's power waves, allows the definition of a set of input and output normalized power waves defined as follows

$$\mathscr{A} = \begin{pmatrix} a_{d12} \\ a_{d34} \\ \cdot \\ \cdot \\ a_{d(p-1)p} \\ a_{c12} \\ a_{c34} \\ \cdot \\ \cdot \\ a_{c(p-1)p} \\ a_{p+1} \\ \cdot \\ \cdot \\ a_{n-1} \\ a_n \end{pmatrix} \quad \mathscr{B} = \begin{pmatrix} b_{d12} \\ b_{d34} \\ \cdot \\ \cdot \\ b_{d(p-1)p} \\ b_{c12} \\ b_{c34} \\ \cdot \\ \cdot \\ b_{c(p-1)p} \\ b_{p+1} \\ \cdot \\ \cdot \\ b_{n-1} \\ b_n \end{pmatrix}, \tag{3.7}$$

which ride to the well know expression $b = Sa$, but for an n-port device which embrace standard S-parameters and mixed-mode S-parameters

$$\mathscr{B} = \mathscr{S}\mathscr{A}. \tag{3.8}$$

In order to distinguish between Ferrero and Pirola's generalized S-parameters, $\overset{\circ}{S}$, and the one's obtained from (3.2), calligraphic letters are used.

Due to the fact that, $\mathscr{S}$ is a physical representation of the n-port device and that $\mathscr{B} = \mathscr{S}\mathscr{A}$ still holds for this general case, one can expect that there is a lineal

transformation which relates $\mathscr{S}$ with standard S-parameters. Such transformation is obtained in [2] and it will not be developed in this work for the general case. However, for the analysis of future examples, we do need to obtain the generalized S-parameters for a three- and four-port device in terms of standard S-parameters. It is remarkable, that the next mathematical development was published by the author of this thesis in DCIS06[1] [7]. Therefore, the presented work was submitted even before Ferrero and Pirola published their generalized S-parameters theory in [2]. It is significant the fact that the RF community was in a rush for obtaining a way to represent, as well as translate, standard S-parameters to mixed-mode for a general device with both mixed-mode and single-ended S-parameters; thus, regarding to this topic, some other publications appeared almost simultaneously or even later [8, 9, 10].

3.2.1 A three-port device's generalized S-parameter matrix

A three-port device is schematically represented in Fig. 3.2. The single-ended port has been set at the left side of the device and it can be assumed as the input port of the DUT for simplicity. Likewise, the output consists of two single-ended ports which can be arranged together in a mixed-mode port. Again, the device's output is not only formed by two ports; indeed, a common-ground is needed to allow the propagation of a common-mode power wave.

Due to the fact that S-parameters describe lineal systems, irrespective of the chosen representation, there is a lineal transformation between the standard S-parameters and the generalized S-parameters. Such transformation can be obtained by expressing the response and stimulus of standard mode and mixed-mode as in [11]

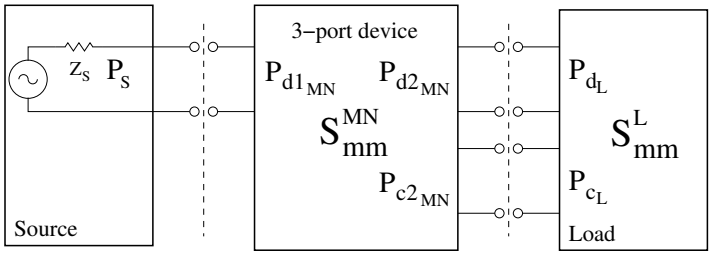

Fig. 3.2 Topology representation of a single-ended to differential device.

$$a_d = \frac{1}{\sqrt{2}}(a_2 - a_3) \tag{3.9}$$

[1] Conference on Design of Circuits and Integrated Systems. Barcelona, 22-24 November 2006

$$b_d = \frac{1}{\sqrt{2}}(b_2 - b_3) \tag{3.10}$$

$$a_c = \frac{1}{\sqrt{2}}(a_2 + a_3) \tag{3.11}$$

$$b_c = \frac{1}{\sqrt{2}}(b_2 + b_3)\,. \tag{3.12}$$

Thereby, port 1 remains referred to a common-ground, thus stimulus and reflected normalized power waves are represented by a_1 and b_1, respectively. Arranging (3.9)-(3.12), in matrix form

$$\begin{pmatrix} a_1 \\ a_d \\ a_c \end{pmatrix} = \begin{pmatrix} 1 & 0 & 0 \\ 0 & \frac{1}{\sqrt{2}} & -\frac{1}{\sqrt{2}} \\ 0 & \frac{1}{\sqrt{2}} & \frac{1}{\sqrt{2}} \end{pmatrix} \begin{pmatrix} a_1 \\ a_2 \\ a_3 \end{pmatrix}, \tag{3.13}$$

the equivalent lineal transformation applies for the normalized reflected power waves i.e. $\mathscr{B} = \mathscr{M} b$, where $\mathscr{M}$ represent the transformation matrix in (3.13). Once $\mathscr{M}$ is known, the transformation between standard S-parameters and generalized S-parameters is given by $\mathscr{S} = \mathscr{M} S \mathscr{M}^{-1}$. Thus, the generalized S-parameter matrix for a three port device is represented by

$$\mathscr{S} = \begin{pmatrix} S_{11} & S_{1d} & S_{1c} \\ S_{d1} & S_{dd} & S_{dc} \\ S_{c1} & S_{cd} & S_{cc} \end{pmatrix}. \tag{3.14}$$

From the definition in (3.14) and $\mathscr{S} = \mathscr{M} S \mathscr{M}^{-1}$, one can finally write the next set of equations

$$\mathscr{S} = \begin{pmatrix} S_{11} & \frac{1}{\sqrt{2}}(S_{12} - S_{13}) & \frac{1}{\sqrt{2}}(S_{12} + S_{13}) \\ \frac{1}{\sqrt{2}}(S_{21} - S_{31}) & \frac{1}{2}(S_{22} - S_{23} - S_{32} + S_{33}) & \frac{1}{2}(S_{22} + S_{23} - S_{32} - S_{33}) \\ \frac{1}{\sqrt{2}}(S_{21} + S_{31}) & \frac{1}{2}(S_{22} - S_{23} + S_{32} - S_{33}) & \frac{1}{2}(S_{22} + S_{23} + S_{32} + S_{33}) \end{pmatrix}. \tag{3.15}$$

As it has been already mentioned, most of the current VNAs actually measure standard S-parameters. Later, mixed-mode S-parameters are obtained by means of expression (3.15) for a three-port device.

3.2.2 A four-port device's generalized S-parameters matrix

Unlike a three-port device, the mixed-mode S-parameter representation for a four-port device was well established in Bockelman and Eisenstadt work[1]. Thereby, the matrix transformation did appear in the same work. Since, the formalism to obtain the generalized S-parameter matrix is similar to the one followed in the last subsection and it has been deduced in several papers [8, 12], we will not go through the complete development. Thus, the generalized S-parameter matrix of a four-port device is arranged as follows

$$\mathscr{S} = \begin{pmatrix} S_{dd11} & S_{dd12} & S_{dc11} & S_{dc12} \\ S_{dd21} & S_{dd22} & S_{dc21} & S_{dc22} \\ S_{cd11} & S_{cd12} & S_{cc11} & S_{cc12} \\ S_{cd21} & S_{cd22} & S_{cc21} & S_{cc22} \end{pmatrix}, \tag{3.16}$$

where *dd* and *cc* subscripts identify pure differential and common-mode driving conditions and can be identified as a sub-matrix S_{DD} and S_{CC} respectively. Meanwhile, subscripts *dc* identifies common-mode driven with differential port measurements, and subscript *cd* identifies differential driven with common-mode port measurement. Likewise, these cross-terms can be identified as the sub-matrices S_{DC} and S_{CD}, respectively. Subscripts *1* and *2* identify between the input and output port, respectively. Proceeding as in Section 3.2.1, the next set of expression can be easily obtained

$$S_{DD} = \frac{1}{2}\begin{pmatrix} S_{11}-S_{13}-S_{31}+S_{33} & S_{12}-S_{14}-S_{32}+S_{34} \\ S_{21}-S_{23}-S_{41}+S_{43} & S_{22}-S_{24}-S_{42}+S_{44} \end{pmatrix}, \tag{3.17}$$

$$S_{CC} = \frac{1}{2}\begin{pmatrix} S_{11}+S_{13}+S_{31}+S_{33} & S_{12}+S_{14}+S_{32}+S_{34} \\ S_{21}+S_{23}+S_{41}+S_{43} & S_{22}+S_{24}+S_{42}+S_{44} \end{pmatrix}, \tag{3.18}$$

$$S_{DC} = \frac{1}{2}\begin{pmatrix} S_{11}+S_{13}-S_{31}-S_{33} & S_{12}+S_{14}-S_{32}-S_{34} \\ S_{21}+S_{23}-S_{41}-S_{43} & S_{22}+S_{24}-S_{42}-S_{44} \end{pmatrix}, \tag{3.19}$$

$$S_{DC} = \frac{1}{2}\begin{pmatrix} S_{11} - S_{13} + S_{31} - S_{33} & S_{12} - S_{14} + S_{32} - S_{34} \\ S_{21} - S_{23} + S_{41} - S_{43} & S_{22} - S_{24} + S_{42} - S_{44} \end{pmatrix}. \tag{3.20}$$

At this point, mixed-mode S-parameters must not be missed understand with the input(output) reflection coefficient of the device. In fact, from Chapter 2 and the existing duality principle that it has been already mentioned in the same chapter, one can expect that both expressions match whenever the device is perfectly adapted or the device is perfectly even(odd)-symmetric. For the rest of cases, the assumption that $S_{DD}\,(S_{CC})$ is equivalent to $\Gamma_d\,(\Gamma_c)$ neglects the common(differential)-mode conversion and, in some cases, it can represent a rough approximation for designer purposes. However, in order to demonstrate this statement, the input(output) reflection coefficient of a n-port device has to be obtained in terms of generalized S-parameters.

3.3 Input reflection coefficient of a n-port device

Similarly as it was done in Chapter 2, when attempting to calculate Γ_i looking at port i in Fig. 3.1, it is useful to keep in mind the definition of the input(output) reflection coefficient $\Gamma_{in}\,(\Gamma_{out})$ of a two-port device. Notice that, port i can be either a differential(common)-mode or even a single-ended port, thereby we will define Γ_i as the quotient between the generalized incident power wave $\mathscr{A}_i$ and the reflected power wave $\mathscr{B}_i$ at i-port, when a set of loads Z_L are connected to the rest of ports. Non special symbols are introduced for Γ_i or Z_L and indeed, their single-ended or differential(common)-mode nature will be simple emphasized by means of lack of superscript for the single-ended case or the superscripts $d(c)$ for the differential(common)-mode case, when needed. Therefore, in the next development, we can keep a standard notation where S-parameters indexed as ij can easily be identified afterwards and replaced with its corresponding single-ended or mixed-mode S-parameters.

For a device which is characterized by the next S-parameters matrix

$$\mathscr{S} = \begin{pmatrix} S_{11} & S_{12} & \cdots & S_{1i} & \cdots & S_{1n} \\ S_{21} & S_{22} & \cdots & S_{2i} & \cdots & S_{2n} \\ \vdots & \vdots & \ddots & \vdots & & \vdots \\ S_{i1} & S_{i2} & \cdots & S_{ij} & \cdots & S_{in} \\ \vdots & \vdots & & \vdots & \ddots & \vdots \\ S_{n1} & S_{n2} & \cdots & S_{ni} & \cdots & S_{nn} \end{pmatrix}, \tag{3.21}$$

Γ_i is defined as the reflection coefficient when respective single-ended or mixed-mode loads are connected to the corresponding *n-1* ports. Thus, for each *j*-port, one can write the next condition $\Gamma_j = \frac{a_j}{b_j}$ which can be rewritten as follows

$$b_j = a_j \lambda_j, \tag{3.22}$$

where λ_j equals Γ_j^{-1}. Notice that a and b waves at each load are reversed with respect its connected port. Then, the system of equations reads

$$\begin{pmatrix} a_1\lambda_1 \\ a_2\lambda_2 \\ \vdots \\ b_i \\ \vdots \\ a_n\lambda_n \end{pmatrix} = \begin{pmatrix} S_{11} & S_{12} & \cdots & S_{1i} & \cdots & S_{1n} \\ S_{21} & S_{22} & \cdots & S_{2i} & \cdots & S_{2n} \\ \vdots & \vdots & \ddots & \vdots & & \vdots \\ S_{i1} & S_{i2} & \cdots & S_{ij} & \cdots & S_{in} \\ \vdots & \vdots & & \vdots & \ddots & \vdots \\ S_{n1} & S_{n2} & \cdots & S_{ni} & \cdots & S_{nn} \end{pmatrix} \begin{pmatrix} a_1 \\ a_2 \\ \vdots \\ a_i \\ \vdots \\ a_n \end{pmatrix}. \tag{3.23}$$

Dividing each term of i-row in (3.23) by a_i, Γ_i reads as follows

$$\Gamma_i = S_{ii} + \sum_{k,k\neq i}^{n} S_{ik} \frac{a_k}{a_i}. \tag{3.24}$$

Notice from (3.23) that the terms $\frac{a_k}{a_i}$ can be obtained from the rest of rows in (3.23). Arranging each of the *n-1* rows and dividing by a_i, we can write a set of n-1 equations represented as follows

$$-S_{ki} = (S_{kk} - \lambda_k) \frac{a_k}{a_i} + \sum_{j,j\neq k}^{n} S_{kj} \frac{a_j}{a_i}, \tag{3.25}$$

where index k goes from 1 to n but $k \neq i$. Notice that (3.25) can be easily written in a matrix form by defining some new terms. Thus, the terms S_{ki} can be easily arranged as a column-vector $\mathbf{S}^i$, formed by the terms of the i-column of the matrix $\mathscr{S}$. Superscript i shows up that the term S_{ii} in $\mathscr{S}$ has to be rejected. Similarly, λ_k can also be arranged as a column-vector $\boldsymbol{\lambda}^i$. By means of this definitions, (3.25) can be written as follows

$$-\mathbf{S}^i = (\mathscr{S} - \boldsymbol{\lambda} I)^i \frac{\mathscr{A}}{a_i}, \tag{3.26}$$

where $(\mathscr{S} - \boldsymbol{\lambda} I)^i$ is formed by the matrix $(\mathscr{S} - \boldsymbol{\lambda} I)$ after removing its i-column and i-row of term. Solving (3.26) formally,

$$\frac{\mathscr{A}}{a_i} = -\left[(\mathscr{S} - \boldsymbol{\lambda} I)^i\right]^{-1} \mathbf{S}^i. \tag{3.27}$$

Thus, replacing (3.27) in (3.24)

$$\Gamma_i = S_{ii} - \sum_{k,k\neq i}^{n} S_{ik} \left[(\mathscr{S} - \boldsymbol{\lambda} I)^i\right]^{-1} \mathbf{S}^i, \tag{3.28}$$

where now S_{ik} can be expressed as a row-vector formed by the terms of the i-row of $\mathscr{S}$. Therefore, (3.28) reads as follows

$$\Gamma_i = S_{ii} - \mathbf{S}_i \left[(\mathscr{S} - \boldsymbol{\lambda} I)^i \right]^{-1} \mathbf{S}^i. \tag{3.29}$$

Equation (3.29) is the input reflection coefficient in port i when the *n-1* rest of ports are loaded with an impedance Z_L which can be different at each port. As it has been previously mention, Γ_i is indeed valid either for a n-port device which is characterized by its standard S-parameters matrix or for a n-port device which behavior is characterized by generalized S-parameter matrix, thus the terms S_{ij} in (3.29) can simply be identified and replaced by standard S-parameters or mixed-mode, S_{mm}, parameters. In order to verify (3.29) let calculate the expressions obtained in Chapter 2. Once expression (3.29) is checked up, we will also obtain, in the next subsections, the different Γ_i cases of a three- and four-port device.

3.3.1 Input reflection coefficient of a two-port device

Using the general expression introduced by (3.29), $\Gamma_d\,(\Gamma_c)$ can be easily obtained for a two-port device described in terms of its mixed-mode S-parameters matrix

$$S_{mm} = \begin{pmatrix} S_{dd} & S_{dc} \\ S_{cd} & S_{cc} \end{pmatrix}. \tag{3.30}$$

For the case of Γ_d, $\mathbf{S}^i$ equals S_{cd}, since it is formed by the first column of (3.30) but removing the subscribed d-term. Likewise, $\mathbf{S}_i$ equals S_{dc}, since it is formed by the first row in (3.30) after removing the first element. The matrix $(\mathscr{S} - \boldsymbol{\lambda} I)^i$ simple becomes $S_{cc} - \lambda_c$ where λ_c is $1/\Gamma_L^c$. After replacing each term in (3.29), Γ_d is given by

$$\Gamma_d = S_{dd} - \frac{S_{dc} S_{cd}}{S_{cc} - 1/\Gamma_L^c}, \tag{3.31}$$

that can be arranged as follows

$$\Gamma_d = \frac{S_{dd} - |S|\,\Gamma_L^c}{1 - S_{cc}\Gamma_L^c}. \tag{3.32}$$

Equation (3.32) matches with the expression (2.5) obtained in Chapter 2.

Similarly, for Γ_c, $\mathbf{S}^i$ equals S_{dc}, since it is formed by the second column of (3.30) but removing the subscribed c-term. Likewise, $\mathbf{S}_i$ equals S_{cd}, since it is formed by the second row in (3.30) after removing the second element. The matrix $(\mathscr{S} - \boldsymbol{\lambda} I)^i$ becomes $S_{dd} - \lambda_d$ where now, λ_d is $1/\Gamma_L^d$. After replacing each term and doing some calculations, Γ_d reads as (2.10). Thus, (3.29) has correctly solved the basic case of a two-port device and will be used to obtain Γ_i of a three- and four-port device.

3.3.2 Input reflection coefficient of a three-port device

For a three port device, we have already seen that $\mathscr{S}$ can be written as

$$\mathscr{S} = \begin{pmatrix} S_{11} & S_{1d} & S_{1c} \\ S_{d1} & S_{dd} & S_{dc} \\ S_{c1} & S_{cd} & S_{cc} \end{pmatrix}. \tag{3.33}$$

Starting with the input reflection coefficient, Γ_1, seen from *port 1*, $\mathbf{S}^1$ is formed by the first column but removing the first element, thus

$$\mathbf{S}^1 = \begin{pmatrix} S_{d1} \\ S_{c1} \end{pmatrix}. \tag{3.34}$$

Likewise, $\mathbf{S}_1$ is form by the first row but removing the first component

$$\mathbf{S}_1 = \begin{pmatrix} S_{1d} & S_{1c} \end{pmatrix}. \tag{3.35}$$

The matrix $(\mathscr{S} - \boldsymbol{\lambda} I)^i$ is obtained by removing the first column and row to the next matrix

$$(\mathscr{S} - \boldsymbol{\lambda} I) = \begin{pmatrix} S_{11} - \lambda_1 & S_{1d} & S_{1c} \\ S_{d1} & S_{dd} - \lambda_d & S_{dc} \\ S_{c1} & S_{cd} & S_{cc} - \lambda_c \end{pmatrix} \tag{3.36}$$

Therefore, after inverting $(\mathscr{S} - \boldsymbol{\lambda} I)^i$ and solving the matrix and vector product and extra algebra, Γ_1 reads as

$$\Gamma_1 = \frac{S_{11} - |S_{1-d}|\Gamma_L^d - |S_{1-c}|\Gamma_L^c + |S|\Gamma_L^d\Gamma_L^c}{1 - S_{dd}\Gamma_L^d - S_{cc}\Gamma_L^c + |S_{mm}|\Gamma_L^d\Gamma_L^c}, \tag{3.37}$$

where $|S_{1-d}|$, $|S_{1-c}|$, $|S_{mm}|$ and $|S|$ correspond to the determinants of the next matrices

$$\begin{aligned} |S_{1-d}| &= det\left|\begin{pmatrix} S_{11} & S_{1d} \\ S_{d1} & S_{dd} \end{pmatrix}\right|, \quad |S_{mm}| = det\left|\begin{pmatrix} S_{dd} & S_{dc} \\ S_{cd} & S_{cc} \end{pmatrix}\right| \\ |S_{1-c}| &= det\left|\begin{pmatrix} S_{11} & S_{1c} \\ S_{c1} & S_{cc} \end{pmatrix}\right|, \quad |S| = det\left|\begin{pmatrix} S_{11} & S_{1d} & S_{1c} \\ S_{d1} & S_{dd} & S_{dc} \\ S_{c1} & S_{cd} & S_{cc} \end{pmatrix}\right|. \end{aligned} \tag{3.38}$$

Looking at the three-port device from the output, two more input reflection coefficients can be defined Γ_d and Γ_c. Notice that the subscript d and c are chosen to show up that output port is described in terms of mixed-mode S-parameters. Also, it is important to remember that those ports are defined as the differential(common)-mode input reflection coefficient when a single ended load Z_L^1 is connected at the input port, and a common(differential) load Z_L^c $\left(Z_L^d\right)$ at the complementary output

port, respectively. By using (3.29) and the definitions in (3.38), Γ_d and Γ_c read as follows

$$\Gamma_d = \frac{S_{dd} - |S_{1-d}|\Gamma_L^1 - |S_{mm}|\Gamma_L^c + |S|\Gamma_L^1\Gamma_L^c}{1 - S_{11}\Gamma_L^1 - S_{cc}\Gamma_L^c + |S_{1-c}|\Gamma_L^1\Gamma_L^c} \tag{3.39}$$

$$\Gamma_c = \frac{S_{cc} - |S_{1-c}|\Gamma_L^1 - |S_{mm}|\Gamma_L^d + |S|\Gamma_L^1\Gamma_L^d}{1 - S_{11}\Gamma_L^1 - S_{dd}\Gamma_L^d + |S_{1-d}|\Gamma_L^1\Gamma_L^d} \tag{3.40}$$

At this point, from (3.37), (3.39) and (3.40), one can elucidate some important properties. To start with,

i. From (3.37), (3.39) and (3.40), only in the case when the component is completely matched (i.e. Γ_L^1, Γ_L^d and Γ_L^c are zero), Γ_1, Γ_d and Γ_c equals S_{11}, S_{dd} and S_{cc} respectively. Otherwise, the assumption is an approximation which can become rough depending on the matching condition and the application.
ii. For a symmetric device (i.e., in the case of a three-port device, only one symmetry axis exists which allows even or odd symmetry against *port 2* and *port 3*); Γ_1, Γ_d and Γ_c can not be assumed as S_{11}, S_{dd} and S_{cc} respectively. Notice that on the contrary the assumption would be against of (i). However, let's assume an odd-symmetry device. The generalized S-parameter matrix for this device is given by

$$\mathscr{S} = \begin{pmatrix} S_{11} & 0 & S_{1c} \\ 0 & S_{dd} & 0 \\ S_{c1} & 0 & S_{cc} \end{pmatrix}. \tag{3.41}$$

For this case, the determinants in (3.38) reads as follows: $|S_{1-d}|$ equals $S_{11}S_{dd}$, $|S_{mm}|$ equals $S_{dd}S_{cc}$, and $|S|$ can be kept as a function of $|S_{1-c}|$, thus $|S|$ equals $S_{dd}\,|S_{1-c}|$. Replacing these expressions in (3.37), (3.39) and (3.40), the input reflection coefficient for each port in the case of an even-symmetry device is given by

$$\Gamma_1 = \frac{S_{11} - |S_{1-c}|\Gamma_L^c}{1 - S_{cc}\Gamma_L^c} \tag{3.42}$$

$$\Gamma_d = S_{dd} \tag{3.43}$$

$$\Gamma_c = \frac{S_{cc} - |S_{1-c}|\Gamma_L^1}{1 - S_{11}\Gamma_L^1} \tag{3.44}$$

Notice how symmetry has reduced input reflection coefficient of the three-port device from three to a two dimensional problem (i.e. (3.42) and (3.44) are equivalent to the two-port device problem solved in Chapter 2). Indeed, this results is a consequence of well-known physical law which is the base of the Hamiltonian mechanics: if an n-dimensional system is restricted to a set of k boundary conditions, as instance a system symmetry, the really effective

degrees of freedom will not match the physical ones, and it can be studied with k less parameters.

iii. Considering for simplicity that, for a three-port device, the single-ended port corresponds to the input and the mixed-mode port is the output, the transducer power gain can not be associated to the term S_{1d} or S_{1c}. As in the case of a two-port device, transducer power gain will depend on the input reflection coefficient of the source and load connected to the device as it will be shown in the next sections.

For completeness, for an even-symmetric device, as instance a single-ended to differential amplifier; the generalized S-parameter matrix for this device is given by

$$\mathscr{S} = \begin{pmatrix} S_{11} & S_{1d} & 0 \\ S_{d1} & S_{dd} & 0 \\ 0 & 0 & S_{cc} \end{pmatrix}. \tag{3.45}$$

For this case, the determinants in (3.38) reads as follows: $|S_{1-c}|$ equals $S_{11}S_{cc}$, $|S_{mm}|$ equals $S_{dd}S_{cc}$, and $|S|$ can be kept as a function of $|S_{1-d}|$, thus $|S|$ equals $S_{cc}\,|S_{1-d}|$. Replacing these expressions in (3.37), (3.39) and (3.40), the input reflection coefficient for each port in the case of a odd-symmetric device is given by

$$\Gamma_1 = \frac{S_{11} - |S_{1-d}|\,\Gamma_L^d}{1 - S_{dd}\Gamma_L^d} \tag{3.46}$$

$$\Gamma_d = \frac{S_{dd} - |S_{1-d}|\,\Gamma_L^1}{1 - S_{11}\Gamma_L^1} \tag{3.47}$$

$$\Gamma_c = S_{cc} \tag{3.48}$$

The duality law would have allowed to write (3.46), (3.47) and (3.48) straightforward. Notice again how symmetry has reduced the problem in one-dimension, and it is equivalent to the solution of a two-port device. In fact, the nature of the problem has driven to describe the device by the matrix (3.45) which can be split in two different boxes. This fact can be easily translated into the device if one thinks of its topological representation. The symmetry has split the device and can be solved as two isolated devices where one of them corresponds to a two-port device and the other one corresponds to a one-port device. This physical law was hidden in the odd-symmetry case. However, notice that (3.41) can be re-arranged as

$$\begin{pmatrix} b_{1d} \\ b_{11} \\ b_{1c} \end{pmatrix} = \begin{pmatrix} S_{dd} & 0 & 0 \\ 0 & S_{11} & S_{1c} \\ 0 & S_{c1} & S_{cc} \end{pmatrix} \begin{pmatrix} a_{1d} \\ a_{11} \\ a_{1c} \end{pmatrix}. \tag{3.49}$$

Now, the matrix is split in boxes showing up the symmetric nature of the problem. From a topological point of view, this device can be separated in two devices.

In the general case, (3.37), (3.39) and (3.40) can be written as follows

$$\Gamma_d = S_{dd} + \xi_d$$

$$\xi_d = \frac{S_{1d}S_{d1}\Gamma_L^1\left(1 - S_{cc}\Gamma_L^c\right) + S_{dc}S_{cd}\Gamma_L^c\left(1 - S_{11}\Gamma_L^1\right) + \left(S_{1d}S_{dc}S_{c1} + S_{d1}S_{cd}S_{1c}\right)\Gamma_L^1\Gamma_L^c}{\left(1 - S_{cc}\Gamma_L^c\right)\left(1 - S_{11}\Gamma_L^1\right) - S_{1c}S_{c1}\Gamma_L^1\Gamma_L^c} \tag{3.50}$$

$$\Gamma_c = S_{cc} + \xi_c$$

$$\xi_c = \frac{S_{1c}S_{c1}\Gamma_L^1\left(1 - S_{dd}\Gamma_L^d\right) + S_{dc}S_{cd}\Gamma_L^d\left(1 - S_{11}\Gamma_L^1\right) + \left(S_{1d}S_{dc}S_{c1} + S_{d1}S_{cd}S_{1c}\right)\Gamma_L^1\Gamma_L^d}{\left(1 - S_{dd}\Gamma_L^d\right)\left(1 - S_{cc}\Gamma_L^c\right) - S_{1d}S_{d1}\Gamma_L^1\Gamma_L^d} \tag{3.51}$$

$$\Gamma_1 = S_{11} + \xi_1$$

$$\xi_1 = \frac{S_{1c}S_{c1}\Gamma_L^c\left(1 - S_{dd}\Gamma_L^d\right) + S_{1d}S_{d1}\Gamma_L^d\left(1 - S_{cc}\Gamma_L^c\right) + \left(S_{1d}S_{dc}S_{c1} + S_{d1}S_{cd}S_{1c}\right)\Gamma_L^d\Gamma_L^c}{\left(1 - S_{dd}\Gamma_L^d\right)\left(1 - S_{cc}\Gamma_L^c\right) - S_{dc}S_{cd}\Gamma_L^d\Gamma_L^c} \tag{3.52}$$

where ξ is the error committed when input reflection coefficient is mistaken for $\mathscr{S}_{ii}$. Thereby, these expressions can previously be used to estimate error when symmetry is assumed.

3.3.3 Input reflection coefficient of a four-port device

For a four-port device, we have already seen that $\mathscr{S}$ can be written as

$$\mathscr{S} = \begin{pmatrix} S_{dd11} & S_{dd12} & S_{dc11} & S_{dc12} \\ S_{dd21} & S_{dd22} & S_{dc21} & S_{dc22} \\ S_{cd11} & S_{cd12} & S_{cc11} & S_{cc12} \\ S_{cd21} & S_{cd22} & S_{cc21} & S_{cc22} \end{pmatrix}. \tag{3.53}$$

By means of the general expression (3.29), four input reflection coefficient can be obtained: Γ_{d1}, Γ_{c1}, Γ_{d2} and Γ_{c2}. Each of them are defined as the quotient between the incident and reflected normalized power waves after connecting three of the loads Z_L^{d1}, Z_L^{c1}, Z_L^{d2} and Z_L^{c2} conveniently depending on the case. Thereby the next expressions can be demonstrated

$$\Gamma_{d1} = \frac{S_{dd11} - |B_{cc11,cc22}|\,\Gamma_L^{d2} - \left|B_{dd22,cc22}\right|\Gamma_L^{c1} - \left|B_{dd22,cc11}\right|\Gamma_L^{c2} + \ldots}{1 - S_{dd22}\Gamma_L^{d2} - S_{cc11}\Gamma_L^{c1} - S_{cc22}\Gamma_L^{c2} + \left|B_{dd11,cc11}\right|\Gamma_L^{d2}\Gamma_L^{c2} + \ldots}$$

$$\frac{\ldots + |A_{dd22}|\,\Gamma_L^{c1}\Gamma_L^{c2} + |A_{cc11}|\,\Gamma_L^{d2}\Gamma_L^{c2} + |A_{cc22}|\,\Gamma_L^{d2}\Gamma_L^{c1} - |S|\,\Gamma_L^{d2}\Gamma_L^{c1}\Gamma_L^{c2}}{\ldots + \left|B_{dd11,cc22}\right|\Gamma_L^{d2}\Gamma_L^{c1} + \left|B_{dd11,dd22}\right|\Gamma_L^{c1}\Gamma_L^{c2} - |A_{dd11}|\,\Gamma_L^{d2}\Gamma_L^{c1}\Gamma_L^{c2}} \quad (3.54)$$

$$\Gamma_{c1} = \frac{S_{cc11} - \left|B_{dd22,cc22}\right|\Gamma_L^{d1} - \left|B_{dd11,cc22}\right|\Gamma_L^{d2} - \left|B_{dd11,dd22}\right|\Gamma_L^{c2} + \ldots}{1 - S_{dd11}\Gamma_L^{d1} - S_{dd22}\Gamma_L^{d2} - S_{cc22}\Gamma_L^{c2} + |B_{cc11,cc22}|\,\Gamma_L^{d1}\Gamma_L^{d2} + \ldots}$$

$$\frac{\ldots + |A_{dd22}|\,\Gamma_L^{d1}\Gamma_L^{c2} + |A_{cc22}|\,\Gamma_L^{d1}\Gamma_L^{d2} + |A_{dd11}|\,\Gamma_L^{d2}\Gamma_L^{c2} - |S|\,\Gamma_L^{d1}\Gamma_L^{d2}\Gamma_L^{c2}}{\ldots + \left|B_{cc11,dd22}\right|\Gamma_L^{d1}\Gamma_L^{c2} + \left|B_{cc11,dd11}\right|\Gamma_L^{d2}\Gamma_L^{c2} - |A_{cc11}|\,\Gamma_L^{d1}\Gamma_L^{d2}\Gamma_L^{c2}} \quad (3.55)$$

$$\Gamma_{d2} = \frac{S_{dd22} - |B_{cc11,cc22}|\,\Gamma_L^{d1} - \left|B_{dd11,cc22}\right|\Gamma_L^{c1} - \left|B_{dd11,cc11}\right|\Gamma_L^{c2} + \ldots}{1 - S_{dd11}\Gamma_L^{d1} - S_{cc11}\Gamma_L^{c1} - S_{cc22}\Gamma_L^{c2} + \left|B_{dd22,cc22}\right|\Gamma_L^{d1}\Gamma_L^{c1} + \ldots}$$

$$\frac{\ldots + |A_{cc22}|\,\Gamma_L^{d1}\Gamma_L^{c1} + |A_{cc11}|\,\Gamma_L^{d1}\Gamma_L^{c2} + |A_{dd11}|\,\Gamma_L^{c1}\Gamma_L^{c2} - |S|\,\Gamma_L^{d1}\Gamma_L^{c1}\Gamma_L^{c2}}{\ldots + \left|B_{dd22,cc11}\right|\Gamma_L^{d1}\Gamma_L^{c2} + \left|B_{dd22,dd11}\right|\Gamma_L^{c1}\Gamma_L^{c2} - |A_{dd22}|\,\Gamma_L^{d1}\Gamma_L^{c1}\Gamma_L^{c2}} \quad (3.56)$$

$$\Gamma_{c2} = \frac{S_{cc22} - \left|B_{cc11,dd22}\right|\Gamma_L^{d1} - \left|B_{dd11,cc11}\right|\Gamma_L^{d2} - \left|B_{cc11,dd22}\right|\Gamma_L^{d1} + \ldots}{1 - S_{dd11}\Gamma_L^{d1} - S_{dd22}\Gamma_L^{d2} - S_{cc11}\Gamma_L^{c1} + |B_{cc11,cc22}|\,\Gamma_L^{d1}\Gamma_L^{d2} + \ldots}$$

$$\frac{\ldots + |A_{dd22}|\,\Gamma_L^{d1}\Gamma_L^{c1} + |A_{cc11}|\,\Gamma_L^{d1}\Gamma_L^{d2} + |A_{dd11}|\,\Gamma_L^{d2}\Gamma_L^{c1} - |S|\,\Gamma_L^{d1}\Gamma_L^{d2}\Gamma_L^{c1}}{\ldots + \left|B_{cc22,dd22}\right|\Gamma_L^{d1}\Gamma_L^{c1} + \left|B_{cc22,dd11}\right|\Gamma_L^{d2}\Gamma_L^{c1} - |A_{cc22}|\,\Gamma_L^{d1}\Gamma_L^{d2}\Gamma_L^{c1}}, \quad (3.57)$$

where the terms $\left|B_{ii,jj}\right|$ are the determinant of $|\mathscr{S}|$ where the rows and columns of the elements $\mathscr{S}_{ii}$ and $\mathscr{S}_{jj}$ have been removed. Likewise, the terms $|A_{ii}|$ correspond to the determinant of the matrix $|\mathscr{S}|$ where the row and columns of the term S_{ii} have been removed.

Similarly as in the three-port device, equivalent implications can be pointed out. Only in the case where the device is perfectly matched, i.e. Γ_L^{d1}, Γ_L^{c1}, Γ_L^{d2} and Γ_L^{c2} equal zero, the expressions (3.54)-(3.57) equal S_{dd11}, S_{dd22}, S_{cc11} and S_{cc22} respectively. Also, if a boundary condition is applied, as a defined symmetry, the order of the problem can be reduced. As instance let suppose a fully differential amplifier where, in terms of standard S-parameters, the next set of conditions apply

$$\begin{array}{l} S_{11}=S_{33},\ S_{22}=S_{44},\ S_{12}=S_{34},\\ S_{13}=S_{31},\ S_{24}=S_{42},\ S_{12}=\text{-}S_{14},\\ S_{34}=\text{-}S_{32},\ S_{21}=S_{43},\ S_{21}=\text{-}S_{23},\\ S_{43}=\text{-}S_{41},\ S_{14}=S_{32},\ S_{23}=S_{41}, \end{array} \rightarrow \begin{pmatrix} S_{dd11} & S_{dd12} & 0 & 0 \\ S_{dd21} & S_{dd22} & 0 & 0 \\ 0 & 0 & S_{cc11} & S_{cc12} \\ 0 & 0 & S_{cc21} & S_{cc22} \end{pmatrix} \tag{3.58}$$

The symmetric nature of the device splits the matrix in two different boxes; thus, from a topological point of view, the device can be represented by two isolated two-port devices. Notice that, thanks to this fact, the set of input reflection coefficients reduces to two independent two-port expressions as follows

$$\begin{array}{ll} \Gamma_{d1}=\dfrac{S_{dd11}-|S_{DD}|\Gamma_L^{d2}}{1-S_{dd22}\Gamma_L^{d2}} & \Gamma_{d2}=\dfrac{S_{dd22}-|S_{DD}|\Gamma_L^{d1}}{1-S_{dd11}\Gamma_L^{d1}} \\ \Gamma_{c1}=\dfrac{S_{cc11}-|S_{CC}|\Gamma_L^{c2}}{1-S_{cc22}\Gamma_L^{c2}} & \Gamma_{c2}=\dfrac{S_{cc22}-|S_{CC}|\Gamma_L^{c1}}{1-S_{cc11}\Gamma_L^{c1}} \end{array} \tag{3.59}$$

Even or odd-symmetry are hidden in the term $|S_{DD}|$ and $|S_{CC}|$. One realize how symmetry can really simplify the problem to the well-know two-port device problem.

Notice that at this point, from the different expressions obtained for the reflection coefficients of a two-port, three-port and four-port device, and the principle of induction, it is possible to write Γ_i for a n-port device as follows

$$\Gamma_i=\frac{\begin{array}{l} S_{ii}-\sum\limits_{\substack{j=1\\ j\neq i}}^{n}\left|S_{ij}^{2x2}\right|\Gamma_L^j+\sum\limits_{\substack{j=1\\ k=j\\ j\neq k\neq i}}^{n}\left|S_{ijk}^{3x3}\right|\Gamma_L^j\Gamma_L^k-\sum\limits_{\substack{j=1\\ k=j\\ l=k\\ j\neq k\neq l\neq i}}^{n}\left|S_{ijkl}^{4x4}\right|\Gamma_L^j\Gamma_L^k\Gamma_L^l+\ldots \\ \ldots(-1)^{n-1}\left|S^{nxn}\right|\Gamma_L^j\Gamma_L^k\Gamma_L^l\ldots\Gamma_L^n \end{array}}{\begin{array}{l} 1-\sum\limits_{\substack{j=1\\ j\neq i}}^{n}S_{jj}\Gamma_L^j+\sum\limits_{\substack{j=1\\ k=j\\ j\neq k\neq i}}^{n}\left|S_{jk}^{2x2}\right|\Gamma_L^j\Gamma_L^k-\sum\limits_{\substack{j=1\\ k=j\\ l=k\\ j\neq k\neq l\neq i}}^{n}\left|S_{jkl}^{3x3}\right|\Gamma_L^j\Gamma_L^k\Gamma_L^l+\ldots \\ \ldots(-1)^{n-1}\left|S_{jkl\ldots n}^{(n-1)x(n-1)}\right|\Gamma_L^j\Gamma_L^k\Gamma_L^l\ldots\Gamma_L^n \end{array}} \tag{3.60}$$

where, as instance, the term $\left|S_{jkl\ldots n}^{(n-1)x(n-1)}\right|$ is the determinant of the $(n-1)x(n-1)$-submatrix of $\mathscr{S}$ after removing i-row and i-column. Of course, this representation is more difficult to deal with when it is compared with the matrix representation (3.28). However, in next sections, it will be seen that it still can be useful for our purposes.

3.4 Signal flow graphs and Mason's rules

Signal flow graph (SFG) is a technique commonly used to represent the signal flow in physical systems. As instance, the description of control systems, digital filters or digital state machines and, of course, it is commonly used in the resolution of lineal electronic circuits. In a given graph, the system is described by nodes and branches. Nodes represent the variables of the system and branches the existing gain between an independent and a dependent variable. Thereby, a system is described by connecting nodes by means of branches by following the system description. Therefore, a SFG can only represent multiplications and additions since it has a one-to-one relationship with a system of linear equations. Once a system is described by its signal flow graph, any transfer function between its nodes can be obtained by the Mason's gain formula (MGF)[3, 4, 13]. For a general case, the transfer function T_{ij}, between the independent variable x_i (input) and the dependent variable (output) x_j, is given by Mason's gain formula

$$T_{ij} = \frac{x_j}{x_i} = \frac{\sum_k P_{ijk}\Delta_{ijk}}{\Delta}, \tag{3.61}$$

where P_{ijk} is the k_{th} complete gain path from x_i to x_j, Δ_{ijk} is the co-factor of Δ of the path P_{ijk}. The expression of Δ is the determinant of the whole graph given by

$$\Delta = 1 - \sum_n L_n + \sum_{m,q} L_m L_q - \sum L_r L_s L_t + \ldots, \tag{3.62}$$

where L_n is the loop gain of each closed loop in the system, $L_m L_q$ is the product of any two non-touching loops (i.e. closed loops which do not share any common node), and so on.

Often in the simplest cases, Mason's gain formula, (3.61), can be determined by inspection of the signal flow graph becoming a powerful analysis method. In general, the method can easily handle SFGs with many variables and loops including loops with inner loops; however, in those cases, Mason's gain formula becomes cumbersome and an automatic solving tool is required [14, 15]. Even though, in difficult cases, the direct use of automatic solvers leads to a lack of interpretation which sometimes ends in slow calculations or poor interpretations.

As it has been already mentioned, SFGs and MGF can perfectly be used to solve electronic systems. In fact, they have been commonly used in RF, but when single-ended topologies are used and described by standard S-parameters. Likewise single-ended cases, devices or systems represented by generalized S-parameters, $\mathscr{S}$, represent linear systems; thereby, signal flow graphs and the Mason's gain formula is a technique that can be extended to solve such systems. It is expected that parameters as the reflection coefficient and other expressions as voltage gain or transducer power gain can be obtained. To the author acknowledge, it is the first time this technique is used to solve n-port devices described by generalized S-parameters. Thereby, as an instance, the input reflection coefficient of a single-ended to differential device represented in Fig. 3.3 can be calculated by this method. As it was seen

in Section 3.3.3, such device is defined by the S-parameter matrix (3.33). Then, Fig. 3.4 represents Fig. 3.3 connection.

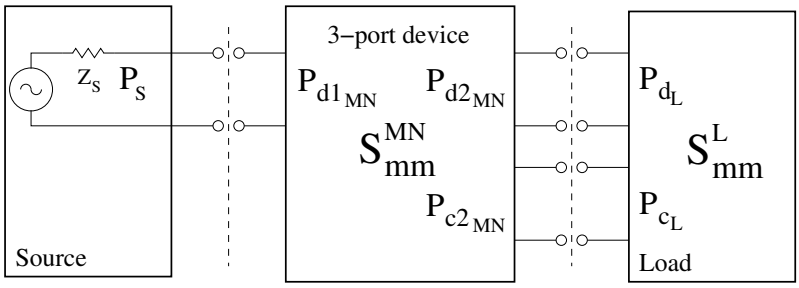

Fig. 3.3 Topological connection of a three-port device.

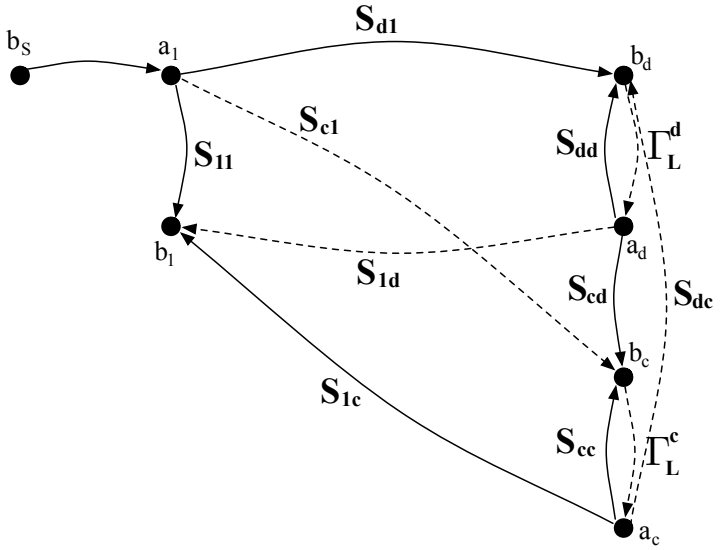

Fig. 3.4 Signal flow graph for a 3-port device in mixed-mode S-parameters to obtain the input reflection coefficient Γ_1.

From the inspection of Fig. 3.4, it is possible to identify the different terms of Maison's gain formula in (3.61), which are summarized in Table 3.1. As instance, path numbered 5th connects a_1 with b_1 following the dashed line in Fig. 3.4. It is easy to identify that, effectively, this path has a total gain $S_{c1}\Gamma_L^c S_{dc}\Gamma_L^d S_{1d}$. Likewise, a simple look at the SFG shows that there are three possible closed loops. And only one two-non-touching loops. Terms in Table 3.1 can be replaced in (3.61), and Γ_1 reads as follows

Table 3.1 Mason's rules' parameters for the calculation of Γ_{in} of a single-ended to differential device.

P_{ijk}, complete gain paths	$P_1 = S_{11}$ $P_2 = S_{d1}\Gamma_L^d S_{1d}$ $P_3 = S_{c1}\Gamma_L^c S_{1c}$ $P_4 = S_{d1}\Gamma_L^d S_{cd}\Gamma_L^c S_{1c}$ $P_5 = S_{c1}\Gamma_L^c S_{dc}\Gamma_L^d S_{1d}$
L_n, loop gain of each closed loop	$L_1 = \Gamma_L^d S_{dd}$ $L_2 = \Gamma_L^c S_{cc}$ $L_3 = \Gamma_L^d S_{cd}\Gamma_L^c S_{dc}$
$L_m L_q$, product of any two non-touching loops	$L_1 L_2 = \Gamma_L^d S_{dd}\Gamma_L^c S_{cc}$
Δ	$1 - L_1 - L_2 - L_3 + L_1 L_2$
Δ_{ijk}	$\Delta_1 = \Delta$, $\Delta_2 = 1 - L_2$, $\Delta_3 = 1 - L_1$, $\Delta_4 = 1$, $\Delta_5 = 1$

$$\Gamma_1 = \frac{S_{11}\left(1 - S_{dd}\Gamma_L^d - S_{cc}\Gamma_L^c - S_{cd}S_{dc}\Gamma_L^d\Gamma_L^c + S_{dd}S_{cc}\Gamma_L^d\Gamma_L^c\right)}{1 - S_{dd}\Gamma_L^d - S_{cc}\Gamma_L^c - S_{cd}S_{dc}\Gamma_L^d\Gamma_L^c + S_{dd}S_{cc}\Gamma_L^d\Gamma_L^c} +$$

$$+ \frac{S_{d1}S_{1d}\left(1 - S_{cc}\Gamma_L^c\right) + S_{c1}S_{1c}\left(1 - S_{dd}\Gamma_L^d\right) + S_{d1}S_{cd}S_{1c}\Gamma_L^d\Gamma_L^c + S_{c1}S_{dc}S_{1d}\Gamma_L^d\Gamma_L^c}{1 - S_{dd}\Gamma_L^d - S_{cc}\Gamma_L^c - S_{cd}S_{dc}\Gamma_L^d\Gamma_L^c + S_{dd}S_{cc}\Gamma_L^d\Gamma_L^c} \tag{3.63}$$

After some algebra, it can be seen that (3.63) coincides with (3.37) and with (3.60) when n equals 3. From all of them, it is clear that the number of terms in T_{ij} grows exponentially with the number of ports, thus an automatic solver is in general needed. For the case of Γ_i, the matrix expression (3.29) or (3.60) represents an easier programmable expression, since it only involves the calculation of different determinants and, only in the case of (3.29), a matrix inversion. However, SFGs can be used to calculate different parameters further than Γ_i.

Thus, another interesting example of the utilization of SFGs is the evaluation of the available power in a source. This simple case is represented in Fig. 3.5. Thus, a signal source with an impedance Z_s (i.e. reflection coefficient is given by Γ_s) launches a signal to an load impedance Z_L (i.e. reflection coefficient is given by Γ_L).

The signal in nodes b_d and a_d can be easily found by simply inspection and by means of (3.61).

$$\frac{b_d}{b_s} = \frac{1}{1 - \Gamma_L\Gamma_S} \tag{3.64}$$

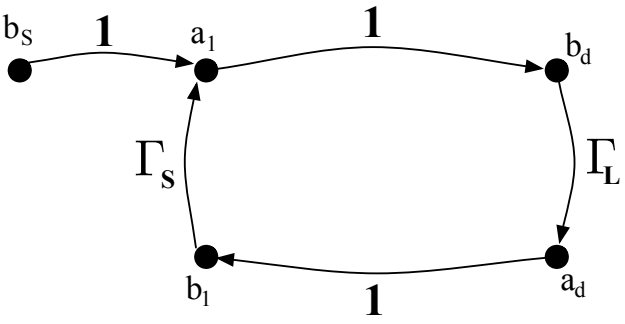

Fig. 3.5 Signal flow graph of a source loaded with a load.

$$\frac{a_d}{b_s} = \frac{\Gamma_L}{1-\Gamma_L\Gamma_S}. \tag{3.65}$$

Once b_d and a_d are found, it is possible to calculate the power delivered into the load as

$$P = |b_d|^2 - |a_d|^2 = \frac{|b_s|^2\left(1-|\Gamma_L|^2\right)}{|1-\Gamma_L\Gamma_S|^2}. \tag{3.66}$$

If Γ_L equals Γ_S^*, the power delivered P is given by

$$P_{ava} = \frac{|b_s|^2}{\left(1-|\Gamma_S|^2\right)}, \tag{3.67}$$

which is the available power in the source.

Most of the techniques to describe the power match of an n-port device has been extended to the use of generalized S-parameters. However, there is a fundamental point which is still missed: the methods to perform the actual transformation from a given generalized port description to another generalized port description with a different set of reference impedance. This part is actually the key point for defining power gain, stability circles and mismatch circles for a n-port device.

3.5 Port impedance transformation: general power matching

Ferrero and Pirola's innovative approach extended the S-parameter definition to multiport networks having conventional single-ended and differential ports. However, this formalism lacks for actual two practical important points. First, how to translate single-ended voltages and impedances V_i and Z_i at a single-ended port -i to the generalized voltage and impedance $\mathscr{V}_i$ and $\mathscr{Z}_i$. This point is not too much important from a mathematical point of view; however, it shows up important $\mathscr{S}$ proper-

ties. As instance, for a reciprocal device, it is well-known that $\mathscr{Z}$ must equal $\mathscr{Z}^t$, where the superscript t indicates the transposed matrix. Thereby, by means of this relation one can demonstrate that for a reciprocal device $\mathscr{S}_{ij}$ equals $\mathscr{S}_{ji}$. Equally important, such relation leads to the second point which Ferrero and Pirola's left out, the methods to perform the actual transformation from a given generalized port description to another generalized port description with a different set of reference impedances. This part is actually the key point for defining power gain, stability circles and mismatch circles for a n-port device. In order to obtain the relation between generalized S-parameter matrix within impedance reference system $\mathscr{S}$, and the respective $\mathscr{S}'$, in a second impedance reference system, the expression of $\mathscr{Z}$ in terms of $\mathscr{S}$ needs to be found. Thereby, using the definition (3.2) and the generalized arrangement $\mathscr{A}$ and $\mathscr{B}$, the next relations can be written

$$\begin{aligned} \mathscr{A} &= F\left(\mathscr{V} + G\mathscr{I}\right) \\ \mathscr{B} &= F\left(\mathscr{V} - G^{\dagger}\mathscr{I}\right), \end{aligned} \tag{3.68}$$

where the superscript † describes the complex conjugate transposed matrix. Moreover, F and G are diagonal matrices which reads as follows

$$F = \begin{pmatrix} \frac{1}{2\sqrt{R_{d_{12}}}} & & & & & & & & \\ & \frac{1}{2\sqrt{R_{d_{34}}}} & & & & & & & \\ & & \frac{1}{2\sqrt{R_{d_{(p-1)p}}}} & & & & & & \\ & & & \frac{1}{2\sqrt{R_{c_{12}}}} & & & & & \\ & & & & \ddots & & & & \\ & & & & & \frac{1}{2\sqrt{R_{c_{(p-1)p}}}} & & & \\ & & & & & & \frac{1}{2\sqrt{R_{p+1}}} & & \\ & & & & & & & \ddots & \\ & & & & & & & & \frac{1}{2\sqrt{R_n}} \end{pmatrix}, \tag{3.69}$$

$$G = \begin{pmatrix} Z_{d_{12}} & & & & & & & & \\ & Z_{d_{34}} & & & & & & & \\ & & \ddots & & & & & & \\ & & & Z_{d_{(p-1)p}} & & & & & \\ & & & & Z_{c_{12}} & & & & \\ & & & & & \ddots & & & \\ & & & & & & Z_{c_{(p-1)p}} & & \\ & & & & & & & Z_{p+1} & \\ & & & & & & & & \ddots \\ & & & & & & & & & Z_n \end{pmatrix}. \tag{3.70}$$

The relation between $\mathscr{A}$ and $\mathscr{B}$ is given by $\mathscr{S}$ in (3.8). Therefore, using the former matrix definition in (3.8)

$$F\left(\mathscr{V} - G^{\dagger}\mathscr{I}\right) = \mathscr{S}F\left(\mathscr{V} + G\mathscr{I}\right). \tag{3.71}$$

Likewise, the relation between $\mathscr{V}$ and $\mathscr{I}$ is given by the Ohm law $\mathscr{V} = \mathscr{Z}\mathscr{I}$, that can be replaced in (3.71)

$$F\left(\mathscr{Z}\mathscr{I} - G^{\dagger}\mathscr{I}\right) = \mathscr{S}F\left(\mathscr{Z}\mathscr{I} + G\mathscr{I}\right). \tag{3.72}$$

After some algebra, (3.72) reads as follows

$$F\left(\mathscr{Z} - G^{\dagger}\right) = \mathscr{S}F\left(\mathscr{Z} + G\right). \tag{3.73}$$

Finally, $\mathscr{S}$ can be obtained from (3.73)

$$\mathscr{S} = F\left(\mathscr{Z} - G^{\dagger}\right)\left(\mathscr{Z} + G\right)^{-1}F^{-1}. \tag{3.74}$$

Likewise, $\mathscr{Z}$ can be expressed in terms of $\mathscr{S}$ after inverting (3.74)

$$\mathscr{Z} = F^{-1}\left(1 - \mathscr{S}\right)^{-1}\left(\mathscr{S}G + G^{\dagger}\right)F. \tag{3.75}$$

It can be notice that the mention duality between standard and mixed-mode S-parameters leads to (3.75) which is the equivalent expression found by Kurokawa for standard S-parameters in [5], but now it can be used with generalized S-parameters. In fact, (3.75) can be also used with $\overset{\circ}{S}$ (i.e. pseudo power waves) if F and G are defined accordingly.

Expression (3.75) can be checked with a simple case. For a two-port device expressed in mixed-mode S-parameters, where R_d and R_c equals $2R_0$ and $R_0/2$ respectively, F and G are given by

$$F = \frac{\sqrt{2R_0}}{2R_0}\begin{pmatrix} \frac{1}{2} & 0 \\ 0 & 1 \end{pmatrix} \quad G = G^{\dagger} = R_0\begin{pmatrix} 2 & 0 \\ 0 & \frac{1}{2} \end{pmatrix} \tag{3.76}$$

Substituting (3.76) in (3.75), $\mathscr{Z}$ reads as follows

$$\mathscr{Z} = \frac{2R_0}{(1\text{-}S_{dd}\text{-}S_{cc} + |S|)} \begin{pmatrix} 1 & 0 \\ 0 & \frac{1}{2} \end{pmatrix} \begin{pmatrix} 1\text{-}S_{cc} & -S_{dc} \\ -S_{cd} & 1\text{-}S_{dd} \end{pmatrix} \begin{pmatrix} 1\text{+}S_{dd} & S_{dc} \\ S_{cd} & 1\text{+}S_{cc} \end{pmatrix} \begin{pmatrix} 1 & 0 \\ 0 & \frac{1}{2} \end{pmatrix}. \quad (3.77)$$

Thereby, solving the matrix product, $\mathscr{Z}$ is finally given by

$$\mathscr{Z} = \frac{2R_0}{(1\text{-}S_{dd}\text{-}S_{cc}\text{+}|S|)} \begin{pmatrix} (1\text{-}S_{cc})(1\text{+}S_{dd})\text{-}S_{dc}S_{cd} & \dfrac{(1\text{-}S_{cc})S_{dc}\text{-}(1\text{+}S_{cc})S_{dc}}{2} \\ \dfrac{(1\text{-}S_{dd})S_{cd}\text{-}(1\text{+}S_{dd})S_{cd}}{2} & \dfrac{(1\text{+}S_{cc})(1\text{-}S_{dd})\text{-}S_{dc}S_{cd}}{4} \end{pmatrix}. \quad (3.78)$$

As it is expected, (3.78) matches with the classical S- to Z-parameters transformation for the given case. For an even- or odd-symmetric device where S_{dc} and S_{cd} equals zero, impedance matrix $\mathscr{Z}$ simplifies as follows

$$\mathscr{Z} = \begin{pmatrix} 2R_0 \dfrac{1+S_{dd}}{1-S_{dd}} & 0 \\ 0 & \dfrac{R_0}{2}\dfrac{1+S_{cc}}{1-S_{cc}} \end{pmatrix}, \quad (3.79)$$

and, (3.79) matches the bilineal transformation of the S-parameter matrix as would be expected.

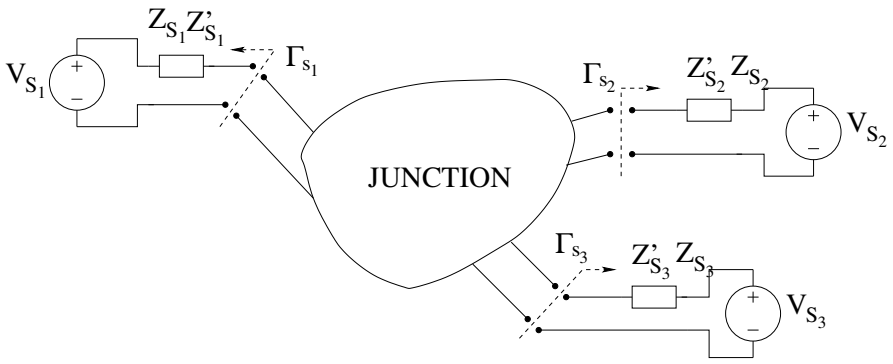

Fig. 3.6 Reference impedance change of an n-port device.

As it is well known, the S-parameter takes into account the power relationship between sources and loads connected through an n-port junction. Thus, if reference impedance in Fig. 3.6 changes, the S-parameter matrix $\mathscr{S}$ for a n-port device, changes. Thereby, it is important to find such relation. Furthermore, finding the re-

lation between two different matrices $\mathscr{S}$ and $\mathscr{S}'$, over two different impedance references, leads to power gain, stability circles and mismatch circles. Such impedance transformation can be found by using the transformations (3.74) and (3.75), since both systems has the same $\mathscr{Z}$ description.

In the new reference system, we have that

$$\mathscr{S}' = F' \left(\mathscr{Z} - G'^{\dagger}\right) \left(\mathscr{Z} + G'\right)^{-1} F'^{-1}. \tag{3.80}$$

Substituting (3.75) in (3.80) gives the next relationship between $\mathscr{S}'$ and $\mathscr{S}$

$$\begin{array}{c} \mathscr{S}' = F' \left(F^{-1} \left(1 - \mathscr{S}\right)^{-1} \left(\mathscr{S} G + G^{\dagger}\right) F - G'^{\dagger}\right) \cdot \\ \cdot \left(F^{-1} \left(1 - \mathscr{S}\right)^{-1} \left(\mathscr{S} G + G^{\dagger}\right) F + G'\right)^{-1} F'^{-1} \end{array}. \tag{3.81}$$

Because F, G and $G^{\dagger}$ are diagonal the next equality applies $F^{-1}GF = FGF^{-1} = G$. Then,

$$\begin{array}{c} \mathscr{S}' = F'F^{-1} \left(\left(1 - \mathscr{S}\right)^{-1} \left(\mathscr{S} G + G^{\dagger}\right) - G'^{\dagger}\right) \cdot \\ \cdot \left(\left(\mathscr{S} G + G^{\dagger}\right) \left(1 - \mathscr{S}\right) + G'^{-1}\right) F F'^{-1} \end{array}. \tag{3.82}$$

The first factor in (3.82) can be simplified by factorizing $\left(1 - \mathscr{S}\right)^{-1}$ and defining $\Gamma = \left(G' - G\right) \left(G' + G^{\dagger}\right)^{-1}$. Thus, it can be written as follows

$$\left(1 - \mathscr{S}\right)^{-1} \left(\mathscr{S} - \Gamma^{\dagger}\right) \left(G + G'^{\dagger}\right). \tag{3.83}$$

Likewise, the second term in (3.82) can be simplified in a similar way, resulting

$$\left(G + G'\right)^{-1} \left(1 - \mathscr{S}\Gamma\right)^{-1} \left(1 - \mathscr{S}\right). \tag{3.84}$$

Replacing (3.83) and (3.84) in (3.82), $\mathscr{S}'$ leads to

$$\begin{array}{c} \mathscr{S}' = F'F^{-1} \left(1 - \mathscr{S}\right)^{-1} \left(\mathscr{S} - \Gamma^{\dagger}\right) \left(G + G'^{\dagger}\right) \cdot \\ \cdot \left(G^{\dagger} + G'\right) \left(1 - \mathscr{S}\Gamma\right)^{-1} \left(1 - \mathscr{S}\right) F F'^{-1} \end{array}. \tag{3.85}$$

Besides, it is possible to demonstrate that the next relations apply

$$\begin{array}{c} \left(1 - \Gamma^{\dagger}\right)^{-1} = \left(G'^{\dagger} + G\right) \left(G + G^{\dagger}\right)^{-1} \\ 1 - \Gamma = \left(G^{\dagger} + G\right) \left(G' + G^{\dagger}\right)^{-1} \end{array}. \tag{3.86}$$

Therefore, (3.85) can be simplified and by means of the relation (3.86) and by using the next matrices properties

$$\begin{array}{c} \left(1 - B\right)^{-1} \left(B - C\right) \left(1 - C\right)^{-1} = \left(1 - C\right)^{-1} \left(B - C\right) \left(1 - B\right)^{-1} \\ \left(1 - C\right) \left(1 - BC\right)^{-1} \left(1 - B\right) = \left(1 - B\right) \left(1 - CB\right)^{-1} \left(1 - C\right). \end{array} \tag{3.87}$$

Thereby, $\mathscr{S}$ results as follows

$$\mathscr{S} = F'F^{-1}\left(1-\Gamma^{\dagger}\right)^{-1}\left(\mathscr{S}-\Gamma^{\dagger}\right)\left(1-\Gamma\mathscr{S}\right)^{-1}\left(1-\Gamma\right)FF'^{-1}. \tag{3.88}$$

Finally, (3.88) can be simplified as follows

$$\mathscr{S}' = A^{-1}\left(\mathscr{S}-\Gamma^{\dagger}\right)\left(1-\Gamma\mathscr{S}\right)^{-1}A^{\dagger}, \tag{3.89}$$

where A is defined as $A = \left(1-\Gamma\right)FF'^{-1}$.

Newly, it is interesting to apply (3.89) to the two-port case when it is expressed with mixed-mode s-parameters. Thereby, substituting each of the terms in (3.89), it is found that

$$\mathscr{S}' = A^{-1}\begin{pmatrix} S_{dd}-\left(\Gamma^{d}\right)^{*} & S_{dc} \\ S_{cd} & S_{cc}-\left(\Gamma^{c}\right)^{*} \end{pmatrix}\begin{pmatrix} 1-\Gamma^{c}S_{cc} & \Gamma^{d}S_{dc} \\ \Gamma^{c}S_{cd} & 1-\Gamma^{d}S_{dd} \end{pmatrix}\frac{A}{|1-\Gamma S|}. \tag{3.90}$$

The reflection coefficients Γ^{d} and Γ^{c} represent the reflection coefficients looking at the reference impedance. This is the reason why scripts d and c are kept as superscripts in order to distinguish them from differential(common)-mode reflection coefficient Γ_d and Γ_c where d and c appear as subscripts.

After calculating the matrix product and omitting the proportional factors which are not important for the next development, (3.90) reads as

$$\mathscr{S}' \propto \begin{pmatrix} \left(S_{dd}\text{-}\left(\Gamma^{d}\right)^{*}\right)\left(1\text{-}\Gamma^{c}S_{cc}\right)+\Gamma^{c}S_{cd}S_{dc} & \left(1\text{-}\Gamma^{d}S_{dd}\right)S_{dc}+\left(S_{dd}\text{-}\left(\Gamma^{d}\right)^{*}\right)S_{dc}\Gamma^{d} \\ \left(1\text{-}\Gamma^{c}S_{cc}\right)S_{cd}+\left(S_{cc}\text{-}\left(\Gamma^{c}\right)^{*}\right)S_{cd}\Gamma^{c} & \left(S_{cc}\text{-}\left(\Gamma^{c}\right)^{*}\right)\left(1\text{-}\Gamma^{d}S_{dd}\right)+\Gamma^{d}S_{dc}S_{cd} \end{pmatrix}. \tag{3.91}$$

Once, the conversion between $\mathscr{S}$ and $\mathscr{S}'$ is found, one can solve the power match problem. The problem is to find the value of source and load impedances that makes possible the maximum power transfer from source to load. Thereby, following with the two-port example, in the case that a differential signal is launched, power match condition is given if $\mathscr{S}'_{dd}$ equals zero and there is not differential power wave reflected back to the source. Thus, the next condition is obtained

$$\left(\Gamma_s^{d}\right)^{*} = \Gamma_d = S_{dd} + \frac{S_{dc}S_{cd}\Gamma_L^{c}}{1-S_{cc}\Gamma_L^{c}}. \tag{3.92}$$

A similar expression can be found if a common-mode power wave is launched but, in this case, $\mathscr{S}'_{cc}$ equals zero for power match condition

$$\left(\Gamma_s^{c}\right)^{*} = \Gamma_c = S_{cc} + \frac{S_{dc}S_{cd}\Gamma_L^{d}}{1-S_{dd}\Gamma_L^{d}}. \tag{3.93}$$

Conditions (3.92) and (3.93) are equivalent to the single-ended power match conditions for a two-port device obtained by (1.10) and (1.11). Thus, the complex conjugate of the reflection coefficient of the source impedance must equal the input reflection coefficient of the device. Of course, this statement is equivalent if it is stated in terms of impedance. However, it is well know that, in the single-ended case, both conditions have to happen simultaneously. Now, it can be shown that conditions (3.92) and (3.93) are independent and maximum power is delivered to the load when the opposite mode is purely reactive. Actually, a value which $|\Gamma|$ equals one is desired, thus an open or short are also possible. Thus, as we saw in Section 2.5, when the differential power wave in Fig. 3.7 is launched, the power going in a differential load is given by $1/2\,|a_d|^2\left(1-|\Gamma_d|^2\right)$. But, some of the power going into the two-port is transformed in a common-mode reflected power wave, and it is dissipated in the common-mode source impedance. Consequently, the total power dissipated in the two-port device is $1/2\,|a_d|^2\left(1-|\Gamma_d|^2\right)-1/2\,|b_c|^2\left(1-|\Gamma_s^c|^2\right)$. Thereby, if the two-port is symmetric i.e. S_{dc} and S_{cd} equal zero, from (3.92), Γ_s^{d*} equals S_{dd} and power match is irrespective of what could be connected in the common-mode.

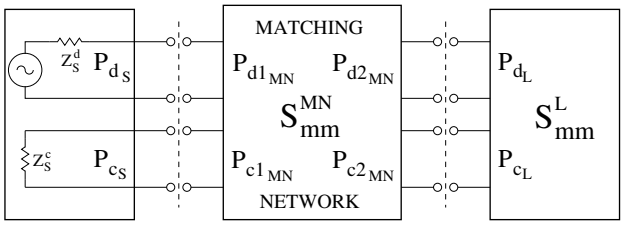

Fig. 3.7 Excitation of a two-port device which is acting as a termination.

In the other hand, if the two-port device is not symmetric, as it was seen in Section 2.5, in order to not dissipate power in the common-mode impedance, Γ_s^c must equal ± 1 (i.e. the common-mode source impedance is a pure reactance), no power can be dissipated in Z_s^c even though the asymmetry condition. Therefore, the power delivered to the two-port device is given by

$$P_L^d = \frac{1}{2}|a_d|^2\left(1-\left|S_{dd}\pm\frac{S_{dc}S_{cd}}{1\mp S_{cc}}\right|^2\right),$$

and matching condition happens when

$$\left(\Gamma_s^d\right)^* = S_{dd}\pm\frac{S_{dc}S_{cd}}{1\mp S_{cc}}. \tag{3.94}$$

Once power match condition is found, a matching network can be synthesized which adapt the source impedance to the required impedance for power match. Un-

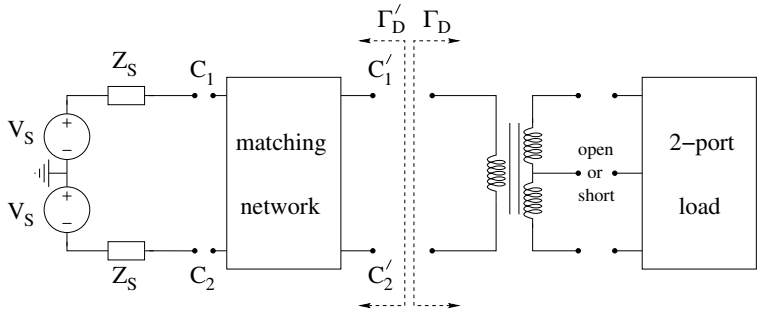

Fig. 3.8 Power match problem for a two-port device which is working as a termination.

like single-ended case, matching network has to provide simultaneously the optimum differential and common-mode impedances. As instance, Fig. 3.8 shows a possible adaptation scheme for a differential case. Thus, common-mode impedance is provided by a the center tap of a transformer which can either form part of the matching network if primary and secondary inductance, and ratio is properly chosen. If the desired impedance is not achieved with the transformer, a matching network can be synthesized in a similar way as for the single-ended case, by connecting serie and parallel components. Table 3.2 summarizes how matching network components are chosen in comparison with the well-known single-ended case. There are some application notes which explain the synthesis of differential matching networks [16, 17]; however, as it has been previously mentioned, all of them misunderstand $\Gamma_d\,(\Gamma_c)$ with $S_{dd}\,(S_{cc})$.

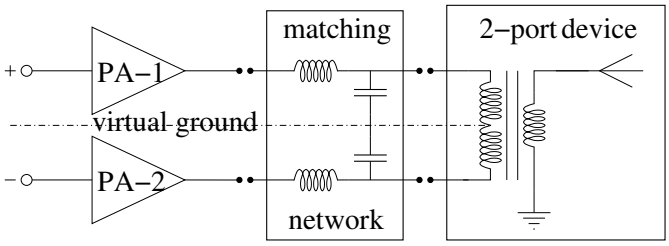

Fig. 3.9 Output scheme of a differential Power Amplifier.

In order to see the error that can be committed and as an example of application of the exposed theory for a two-port device, Fig. 3.9 shows the loadline adaptation of a differential power amplifier. The PA is split in two separated devices and combined by means of a BalUn. Thereby, the differential signal is converted to single-ended in order to attack an antenna. Notice that, even though, the BalUn can be performed by a symmetric transformer, the fact that the ports of the secondary spiral are connected to a different impedance (i.e. port 2 and port 4 are connected to a 75 Ω antenna and a short respectively) makes the BalUn an asymmetric device. Therefore, if the BalUn

Table 3.2 Comparative schemes for the matching network syntheses of single-ended and differential devices.

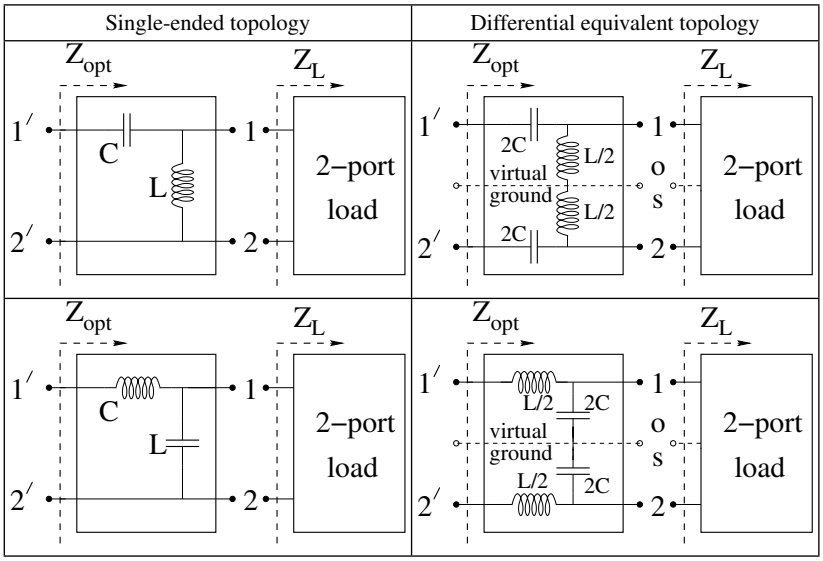

and the antenna are grouped in a two-port termination and the power radiated by the antenna is not externally perturbed, they can be as a two-port termination. In order to obtain the maximum power from the PA, this termination has to be adapted to the optimum loadline impedance value.

For an specific transformer and a 75 Ω antenna, the transformer and antenna block S-parameters are collected in the next table

Table 3.3 Transformer and antenna characteristics seen as a two-port device.

Standard S-parameters	mag$\angle$(degrees)	Mixed-mode S-parameters	mag$\angle$(degrees)
S_{11}	$0.39\angle -11.04°$	S_{dd}	$0.46\angle +104.06°$
S_{12}	$0.64\angle -40.16°$	S_{dc}	$0.008\angle -0.11°$
S_{21}	$0.64\angle -40.16°$	S_{cd}	$0.008\angle -0.11°$
S_{22}	$0.39\angle +21.40°$	S_{cc}	$0.87\angle -0.38°$

From the values in Table 3.3, Γ_d equals $0.5\angle 104.9°$ when common-mode is open. For the given case, a matching network is generated to match S_{dd} to a loadline impedance of 4 Ω. Even though, the apparent small difference between S_{dd} and Γ_d, when the same matching network is used to adapt Γ_d instead of S_{dd}, it leads

to a loadline impedance of 4.4 Ω. It represents a percentage difference of the 9%, simply because the wrong expression is used. Moreover, if a voltage supply of 3.3 V is assumed, and the simple expression of the output power of a PA is calculated by means of $\frac{V_{CC}^2}{2R_L}$, the error in the output power is about 9.5%, which again is a large error just for using a wrong expression.

As it has been shown, (3.89) can be used to find the power match condition for the case of a n-port device. However, depending on the device's characteristics and the application, one has to set load conditions different than the classical $\Gamma_{in} = \Gamma_S^*$. As instance, in the developed case of a differential two-port device, a purely reactive common-mode impedance leads to a higher output power than the conventional simultaneous power-match of differential and common-mode ports. In this way, in the general case represented in Fig 3.1, the power match of an n-port device can be completely solved with the next expression

$$\mathscr{S}' = A^{-1}\left(\mathscr{S} - \Gamma^{\dagger}\right)\left(1 - \mathscr{S}\Gamma\right)^{-1} A^{\dagger}, \tag{3.95}$$

and a set of conditions which involve the device's characteristics, and the application. Thus, a condition has to be establish for each port as follows

$$\begin{gathered}
Port\,(1):\ \Gamma_{d_{12}} = \left(\Gamma^d_{S_{12}}\right)^*,\ \Gamma^c_{S_{12}} = e^{j\alpha^c_{12}} \\
\vdots \\
Port\,(j-1):\ \Gamma^d_{S_{(j-1)j}} = e^{j\alpha^d_{(j-1)j}},\ \Gamma_{c_{(j-1)j}} = \left(\Gamma^c_{S_{(j-1)j}}\right)^* \\
Port\,(j):\ \Gamma_{j+1} = \Gamma^*_{S(j+1)} \\
\vdots \\
Port\,(k):\ \Gamma_k = \Gamma^*_{S(k)} \\
Port\,(k+1):\ \Gamma^d_{S_{(k+1)(k+2)}} = e^{j\alpha^d_{(k+1)(k+2)}},\ \Gamma_{c_{(k+1)(k+2)}} = \left(\Gamma^c_{S_{(k+1)(k+2)}}\right)^* \\
\vdots \\
Port\,(m-1):\ \Gamma^d_{L_{(m-1)m}} = e^{j\alpha^d_{(m-1)m}},\ \Gamma_{c_{(m-1)m}} = \left(\Gamma^c_{L_{(m-1)m}}\right)^* \\
Port\,(m+1):\ \Gamma_{m+1} = \Gamma^*_{L(m+1)} \\
\vdots \\
Port\,(n):\ \Gamma_n = \Gamma^*_{L(n)}
\end{gathered} \tag{3.96}$$

Of course, conditions in (3.96) can change depending on the application. At the end of the day, after applying conditions (3.96) in (3.95), cross-terms of $\mathscr{S}'$ correspond to the maximum power gain between two different ports. Also, it is important to notice that only the use of generalized S-parameters has allowed to achieve

these conditions. A treatment in terms of standard S-parameters leads to the classical power match criteria [5], even when demonstration is conduced in terms of EM fields [18].

By combining the results obtained in this section and by means of signal flow graphs, it is possible to obtain a more suitable solution for (3.95).

3.6 Power gain of an n-port device

As we have mentioned in the introduction, an n-port device is a very varied component. Thus, a device can be formed by multiple input(output) single-ended or mixed-mode S-parameters. Meanwhile, it can completely represent a whole device or multiple devices which are described by an unique S-parameter matrix for pure convenience or for the computation of device cross talk. Then, in the most general case, an n-port can be represented as in Fig. 3.1. Thereby, for this device, power matching consists on finding out those impedances which maximize the transducer power gain between two different ports. As it has been stated in last section, this condition does not have to coincide with impedance conjugate match for all the ports.

As an instance of an n-port, let's represent the SFG of a four-port as in Fig. 3.10. A graph of this kind can represent a full-differential amplifier, a hybrid and so on. If the device is described by means of mixed-mode S-parameters, it has a differential(common)-mode input topological port and a differential(common)-mode output port. Likewise, components connected to the device have a differential (common)-mode behavior which are described by means of $\Gamma_S^d\left(\Gamma_S^c\right)$ and $\Gamma_L^d\left(\Gamma_L^c\right)$. Moreover, in the represented case, a differential signal is launched by means of the source represented by the node b_s^d and the corresponding source impedance Z_S. Notice that, ports can simply be labeled by a number and later be classified as differential or common-mode ports. Thus, even though in the next, transducer power gain is obtained for the case that a differential signal is launched, a common-mode expression can be easily obtained because of the duality principle.

In general, an n-port device, that is described by means of (3.1), has a signal flow graph similar to the represented for the four-port device. Nodes are all related by means of the terms in (3.1); whereas, each of the n-ports, as instance the represented by b_q and a_q, is also related by means of $\Gamma_{S(L)}^q$. Thereby, it is possible to find the transfer function between nodes b_q and a_q over b_s as follows

$$\frac{b_q}{b_s} = T_{1q} = \frac{\sum_k P_{1qk}\Delta_{1qk}}{\Delta}, \tag{3.97}$$

$$\frac{a_q}{b_s} = T'_{1q} = \frac{\sum_k P'_{1qk}\Delta'_{1qk}}{\Delta}. \tag{3.98}$$

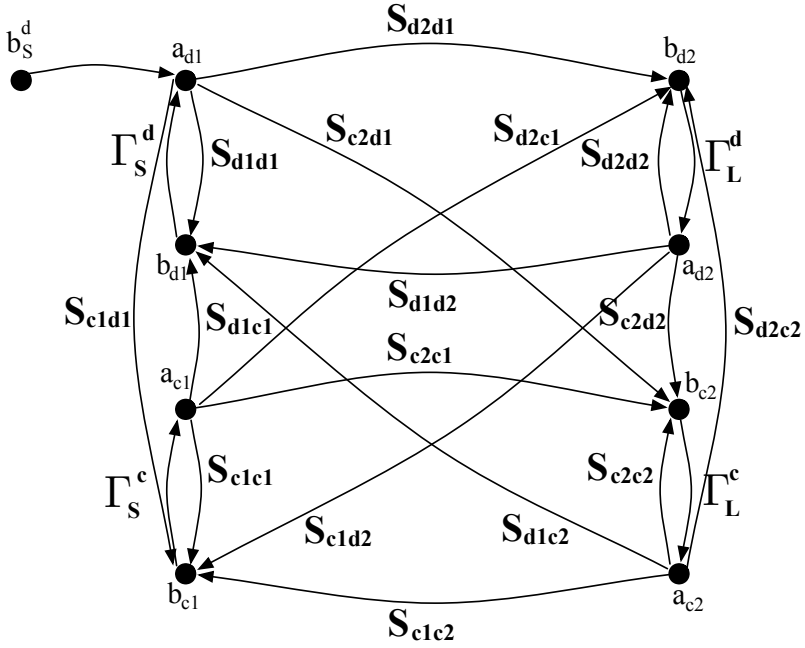

Fig. 3.10 Signal flow graph for a 4-port device in mixed-mode S-parameters.

From Fig. 3.10, it can be notice that for any couple of nodes b_q and a_q, any path up to a_q goes through b_q and Γ_L^q (consider for simplicity that port q is connected to a load which reflection coefficient is Γ_L^q). Thus, any path to a_q (i.e. P'_{1qk} in (3.98)), is given by $P_{1qk}\Gamma_L^q$. Also by inspection, any co-factor Δ'_{1qk} is equal to Δ_{1qk}, since b_q and a_q are consecutive nodes. Moreover, Δ is the same in both expressions (3.97) and (3.98) or even, any other transfer function that could be calculated, since it represents the graph flow determinant which is an invariable of the system. Therefore, the power delivered in port q is given by $\left|b_q\right|^2 - \left|a_q\right|^2$ and reads as follows

$$P_{del} = \frac{\left(\left|\sum_k P_{1qk}\Delta_{1qk}\right|^2 - \left|\sum_k P_{1qk}\Delta_{1qk}\Gamma_L^q\right|^2\right)|b_s|^2}{|\Delta|^2} = \frac{\left|\sum_k P_{1qk}\Delta_{1qk}\right|^2 \left(1 - |\Gamma_L^q|^2\right)|b_s|^2}{|\Delta|^2}. \tag{3.99}$$

From (3.99) and the available power in the source, that was obtained in (3.67), it is possible to write the transducer power gain G_t for a n-port device when a signal is launched at port i

$$G_t = \frac{P_{del}}{P_{ava}} = \frac{\left(1-\left|\Gamma_S^i\right|^2\right)\left|\sum_k P_{1qk}\Delta_{1qk}\right|^2\left(1-\left|\Gamma_L^q\right|^2\right)}{|\Delta|^2}. \tag{3.100}$$

As it has been mentioned in Section 3.4, SFGs are very useful to obtain the transfer function of a system. However, the entropy of the solution is in general high and at the end, it is difficult to deal with them. As a fact, a solution expressed as in (3.60) has a lower entropy. Thus, it is desirable to express the terms in (3.100) in a similar way that in (3.60). To start with, in order to properly write Δ, consider the SFG represented in Fig. (3.11). This representation is equivalent to the SFG in Fig. 3.10, but the device has been replaced with the equivalent Γ_i for port i, that can be calculated by means of (3.60). Since in Fig. (3.11), any transfer function shares the same Δ, let's calculate Γ as the quotient of b_1 over a_1. Also remember that Γ is related with Γ_i, as it was obtained in Section 3.4. Then, the next relation can be written

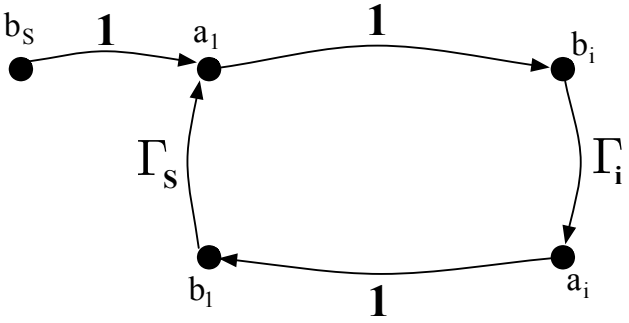

Fig. 3.11 Signal flow graph of a source loaded with a load Γ_i.

$$\Gamma = \frac{\Gamma_i}{1-\Gamma_i\Gamma_S^i} = \frac{\sum_k P_{sik}\Delta_{sik}}{\Delta_i\left(1-\Gamma_i\Gamma_S^i\right)} = \frac{\sum_k P_{sik}\Delta_{sik}}{\Delta}. \tag{3.101}$$

Therefore, from(3.101) it can be written

$$\Delta = \Delta_i\left(1-\Gamma_i\Gamma_S^i\right), \tag{3.102}$$

where Γ_i is given by (3.60) and Δ_i is the determinant of Γ_i and reads as follows

$$\begin{aligned}\Delta_i = 1 - \sum_{\substack{j=1\\ j\neq i}}^{n} S_{jj}\Gamma_L^j + \sum_{\substack{j=1\\ k=j\\ j\neq k\neq i}}^{n}\left|S_{jk}^{2x2}\right|\Gamma_L^j\Gamma_L^k - \sum_{\substack{j=1\\ k=j\\ l=k\\ j\neq k\neq l\neq i}}^{n}\left|S_{jkl}^{3x3}\right|\Gamma_L^j\Gamma_L^k\Gamma_L^l + \ldots \\ \ldots(-1)^{n-1}\left|S_{jkl\ldots n}^{(n-1)x(n-1)}\right|\Gamma_L^j\Gamma_L^k\Gamma_L^l\ldots\Gamma_L^n.\end{aligned} \tag{3.103}$$

The different summations in (3.103) can be split in terms which contain the coefficient Γ_L^q (i.e. those which contain the reflection coefficient of load connected at port q)

$$\begin{aligned}\Delta_i = 1 - S_{qq}\Gamma_L^q - \sum_{\substack{j=1\\ j\neq i\neq q}}^{n} S_{jj}\Gamma_L^j + \sum_{\substack{j=1\\ j\neq i\neq q}}^{n} \left|S_{jq}^{2x2}\right| \Gamma_L^j\Gamma_L^q + \sum_{\substack{j=1\\ k=j\\ j\neq k\neq i\neq q}}^{n} \left|S_{jk}^{2x2}\right| \Gamma_L^j\Gamma_L^k - \\ - \sum_{\substack{j=1\\ k=j\\ j\neq k\neq i\neq q}}^{n} \left|S_{jkq}^{3x3}\right| \Gamma_L^j\Gamma_L^k\Gamma_L^q - \sum_{\substack{j=1\\ k=j\\ l=k\\ j\neq k\neq l\neq i\neq q}}^{n} \left|S_{jkl}^{3x3}\right| \Gamma_L^j\Gamma_L^k\Gamma_L^l + \dots \\ \dots (-1)^{n-1} \left|S_{jkl\dots n}^{(n-1)x(n-1)}\right| \Gamma_L^j\Gamma_L^k\Gamma_L^l \dots \Gamma_L^q \dots \Gamma_L^n.\end{aligned} \tag{3.104}$$

Reordering the two kind of terms, Δ_i reads as follows

$$\begin{aligned}\Delta_i = 1 - \sum_{\substack{j=1\\ j\neq i\neq q}}^{n} S_{jj}\Gamma_L^j + \sum_{\substack{j=1\\ k=j\\ j\neq k\neq i\neq q}}^{n} \left|S_{jk}^{2x2}\right| \Gamma_L^j\Gamma_L^k - \sum_{\substack{j=1\\ k=j\\ l=k\\ j\neq k\neq l\neq i\neq q}}^{n} \left|S_{jkl}^{3x3}\right| \Gamma_L^j\Gamma_L^k\Gamma_L^l + \dots \\ -S_{qq}\Gamma_L^q + \sum_{\substack{j=1\\ j\neq i\neq q}}^{n} \left|S_{jq}^{2x2}\right| \Gamma_L^j\Gamma_L^q - \sum_{\substack{j=1\\ k=j\\ j\neq k\neq i\neq q}}^{n} \left|S_{jkq}^{3x3}\right| \Gamma_L^j\Gamma_L^k\Gamma_L^q + \dots \\ \dots (-1)^{n-1} \left|S_{jkl\dots n}^{(n-1)x(n-1)}\right| \Gamma_L^j\Gamma_L^k\Gamma_L^l \dots \Gamma_L^q \dots \Gamma_L^n.\end{aligned} \tag{3.105}$$

If Γ_L^q is factorized from (3.104), Δ_i is given by

$$\begin{aligned}\Delta_i = \left\{ 1 - \sum_{\substack{j=1\\ j\neq i\neq q}}^{n} S_{jj}\Gamma_L^j + \sum_{\substack{j=1\\ k=j\\ j\neq k\neq i\neq q}}^{n} \left|S_{jk}^{2x2}\right| \Gamma_L^j\Gamma_L^k - \sum_{\substack{j=1\\ k=j\\ l=k\\ j\neq k\neq l\neq i\neq q}}^{n} \left|S_{jkl}^{3x3}\right| \Gamma_L^j\Gamma_L^k\Gamma_L^l + \dots \right\} \cdot \\ \cdot \left\{ 1 - \Gamma_L^q\Gamma_{q\{i^*\}} \right\}.\end{aligned} \tag{3.106}$$

where $\Gamma_{q\{i^*\}}$ is the input reflection coefficient seen from port q but when port i equals the reference impedance i.e. Γ_L^i equals zero. The rest of the ports still keep connected to its respective impedances.

Therefore, if the sum term in (3.108) is named as $\Delta_{q\{i^*\}}$, transducer power gain can be written as follows

$$G_t = \frac{1-\left|\Gamma_S^i\right|^2}{\left|1-\Gamma_S^i\Gamma_i\right|^2}\frac{\left|\sum_k P_{1ik}\Delta_{1ik}\right|^2}{\left|\Delta_{q\{i^*\}}\right|^2}\frac{1-\left|\Gamma_L^q\right|^2}{\left|1-\Gamma_L^q\Gamma_{q\{i^*\}}\right|^2}. \tag{3.107}$$

Notice that (3.107) has been represented in a similar way as the classical transducer power gain in (1.7) for a two-port device. The first and third terms clearly represent the input and output mismatching degree. As in the two-port case, it is always possible to find a source and load impedance which minimize both factors. If the device is unconditionally stable, complex conjugate of input and differential output impedances correspond to such values. Likewise, the second term represents a gain.

However, the term $\Delta_{q\{i^*\}}$ can still be further developed. From (3.108), $\Delta_{q\{i^*\}}$ has the same form that Δ_i. Therefore, the same operation can be done but for a different port h. Thus, $\Delta_{q\{i^*\}}$ reads as

$$\begin{aligned}\Delta_{q\{i^*\}} = \Bigg\{ 1 - \sum_{\substack{j=1\\ j\neq i\neq q\neq h}}^{n} S_{jj}\Gamma_L^j + \sum_{\substack{j=1\\ k=j\\ j\neq k\neq i\neq q\neq h}}^{n} \left|S_{jk}^{2x2}\right|\Gamma_L^j\Gamma_L^k - \dots \\ - \sum_{\substack{j=1\\ k=j\\ l=k\\ j\neq k\neq l\neq i\neq q\neq h}}^{n} \left|S_{jkl}^{3x3}\right|\Gamma_L^j\Gamma_L^k\Gamma_L^l + \dots \Bigg\} \cdot \left\{ 1-\Gamma_L^h\Gamma_{h\{i^*,q^*\}} \right\},\end{aligned} \tag{3.108}$$

where Γ_L^h is the reflection coefficient of the load connected at port h and $\Gamma_{h\{i^*,q^*\}}$ is the input reflection coefficient seen from port h but when port i and q equal the reference impedance i.e. both equal zero. The process can be repeated till the last port. At the end, G_t can be written as

$$G_t = \frac{1-\left|\Gamma_S^i\right|^2}{\left|1-\Gamma_S^i\Gamma_i\right|^2}\left|\alpha_{iq}\right|^2\frac{1-\left|\Gamma_L^q\right|^2}{\left|1-\Gamma_L^q\Gamma_{q\{i^*\}}\right|^2}, \tag{3.109}$$

where $\left|\alpha_{iq}\right|^2$ is given by

$$\left|\alpha_{iq}\right|^2 = \frac{\left|\sum_k P_{1ik}\Delta_{1ik}\right|^2}{\left|1\text{-}\Gamma_L^h\Gamma_{h\{i^*,q^*\}}\right|^2\dots\left|1\text{-}\Gamma_L^nS_{nn}\right|^2\left|1\text{-}\Gamma_L^{(n\text{-}1)}\Gamma_{(n\text{-}1)\{i^*,q^*,\dots,(n\text{-}2)^*\}}\right|^2\dots\left|1\text{-}\Gamma_L^q\Gamma_{q\{i^*\}}\right|^2}. \tag{3.110}$$

Notice that the term $\Gamma_{(n)\{i^*,q^*,\dots,(n\text{-}1)^*\}}$ represents the input reflection coefficient from port n when the rest of other ports are connected to its respective reference

impedances. Thus, from an expression of the type of (3.60), when all the terms Γ_L equal zero, it is possible to see that $\Gamma_{(n)\{i^*,q^*,\ldots,(n\text{-}1)^*\}}$ is simply S_{nn}.

Likewise, the term $\left|\sum_k P_{1ik}\Delta_{1ik}\right|$ can be calculated but resulting an expression that unfortunately, can not be expressed in a similar way that (3.108).

Therefore, once (3.109) and (3.110) have been obtained, the design process for obtaining the power match of ports i and q goes, in general, through maximizing (3.110) meanwhile, Γ_i and Γ_q equal $\left(\Gamma_S^i\right)^*$ and $\left(\Gamma_L^q\right)^*$ respectively.

As an instance, the formalism for the case of the four-port device represented in Fig. 3.10 can be developed (the three-port case will be analyzed in Chapter 6). Thus, (3.109) is expressed as follows

$$G_t = \frac{\left(1-\left|\Gamma_S^d\right|^2\right)}{\left|1-\Gamma_{d1}\Gamma_S^d\right|^2}\left|\alpha_{21}\right|^2\frac{\left(1-\left|\Gamma_L^d\right|^2\right)}{\left|1-\Gamma_{d2}'\Gamma_L^d\right|^2}, \tag{3.111}$$

where

$$\begin{aligned}
\alpha_{21} &= \frac{S_{d2d1}-\left|B_{d1d2,c2c2}\right|\Gamma_S^c-\left|B_{d1d2,c1c1}\right|\Gamma_L^c+\left|A_{d1d2}\right|\Gamma_S^c\Gamma_L^c}{1-S_{c1c1}\Gamma_S^c-S_{c2c2}\Gamma_L^c+\left|B_{d1d1,d2d2}\right|\Gamma_S^c\Gamma_L^c}\\
\Gamma_{d2}' &= \frac{S_{d2d2}-\left|B_{d1d1,c1c1}\right|\Gamma_L^c-\left|B_{d1d1,c2c2}\right|\Gamma_S^c+\left|A_{d1d1}\right|\Gamma_S^c\Gamma_L^c}{1-S_{c1c1}\Gamma_S^c-S_{c2c2}\Gamma_L^c+\left|B_{d1d1,d2d2}\right|\Gamma_S^c\Gamma_L^c}.
\end{aligned} \tag{3.112}$$

It is possible to demonstrate that for a symmetric device where submatrix S_{DC} (S_{CD}) equals zero (1.7) is recovered. Thus,

$$\begin{aligned}
&\left|B_{d1d2,c2c2}\right| = S_{d2d1}S_{c1c1},\ \ \left|B_{d1d2,c1c1}\right| = S_{d2d1}S_{c2c2},\ \ \left|B_{d1d1,d2d2}\right| = \left|S_{CC}\right|\\
&\left|B_{d1d1,c1c1}\right| = S_{d2d2}S_{c2c2},\ \ \left|B_{d1d1,c2c2}\right| = S_{d2d2}S_{c1c1},\\
&\left|A_{d1d2}\right| = S_{d2d1}\left|S_{CC}\right|,\qquad \left|A_{d1d1}\right| = S_{d2d2}\left|S_{CC}\right|.
\end{aligned} \tag{3.113}$$

Coefficients (3.113) can be replaced in (3.111), that after some algebra reads as follows

$$G_t = \frac{\left(1-\left|\Gamma_S^d\right|^2\right)}{\left|1-\Gamma_d\Gamma_S^d\right|^2}\left|S_{d2d1}\right|^2\frac{\left(1-\left|\Gamma_L^d\right|^2\right)}{\left|1-S_{d2d2}\Gamma_L^d\right|^2}, \tag{3.114}$$

where Γ_{d1} is given by (3.54) and, as it has been demonstrated, reduces to (3.59) when the device is symmetric. Expressions obtained for a symmetric device coincides with Bockelman's in [1]. However, Bockelman obtained his expressions considering a ideal symmetric device and assuming similitude with the two-port device expressions.

Moreover, as Bockelman stated in his work, (3.114) is also obtained, when common-mode impedances Z_S^c and Z_L^c equal the common-mode reference impedance (i.e. Γ_S^c and Γ_L^c equal zero). Effectively, from (3.111), it can be demonstrated that (3.114) is also deduced in this case. However, notice that even though Bockelman stated such condition, he did it by simple intuition. Due to the fact that, Bockelman solved a pure differential device, and how it has been demonstrated, in this case, gain is irrespective of common-mode impedance; from Bockelman's formalism, the discussed statement can not be formally formulated.

3.7 Conclusions

Most of the formalism and methodologies commonly used with standard S-params has been extended to mixed-mode for the case of an n-port device. Thus, based on the work of Pirola and Ferrero, the generalized S-parameter matrix has been reformulated to account single-ended and mixed-mode ports but using Kurokawa's power waves definition. Then, based on this formalism, a new matrix expression of the input reflection coefficient of an n-port device has been found. The formula has been validated by solving a two-, three- and four-port device input(output) reflection coefficients. Likewise, the technique of SFG and Mason's rules have been used, for the first time, with generalized S-parameters. Reference impedance transformation has also been reformulated following Kurokawa's work. The new expression can be used for n-port device expressed in terms of $\mathscr{S}$ and has allowed to obtain the power matching condition for this kind of devices. As it has been stated, n-port conjugate matching is not the necessary condition to obtain maximum power but the input(output) conjugate port matching.

Based on the set of methodologies and tools, transducer power gain between two different ports has been obtained. The expression is formally equivalent to the classical two-port expression which contains the input(output) mismatching factors and the available gain factor. Unlike Bockelman theory, the developed theory allows the formal characterization of a general n-port device which can be symmetric or non-symmetric.

3.8 Acknowledgements

This work was supported in part by the Spanish Ministry of Innovation and Science (with support from the European Regional Development Fund) under contract TEC2010-21484; and with the support of the Department of University, Research and society of information of Government of Catalonia. T. Carrasco would like to thank Tom Myers from Qualcomm, Tech. for his warm hospitality during his visit to Qualcomm, QCT in San Diego, CA. And of course, I would like to thank Javier and Jose Maria for their huge support.

References

1. David E. Bockelman. *The Theory, measurement, and applications of mode specific scattering parameters with multiple modes of propagation*. PhD thesis, University of Florida, 1997.
2. A. Ferrero and M. Pirola. Generalized mixed-mode s-parameters. *Microwave Theory and Techniques, IEEE Transactions on*, 54(1):458 –463, jan. 2006.
3. S.J. Mason. Feedback theory-some properties of signal flow graphs. *Proceedings of the IRE*, 41(9):1144–1156, 1953.
4. S.J. Mason. Feedback theory-further properties of signal flow graphs. *Proceedings of the IRE*, 44(7):920–926, 1956.
5. K. Kurokawa. Power waves and the scattering matrix. *Microwave Theory and Techniques, IEEE Transactions on*, 13(2):194–202, 1965.
6. Dylan F. Williams, Senior Member, and Bradley K. Alpert. A general waveguide circuit theory. *J. Res. Natl. Inst. Stand. Technol*, 97:533–562, 1992.
7. Tomas Carrasco Carrillo, Javier Sieiro Cordoba, Aitor Osorio Marti, and Jose Maria Lopez-Villegas. A full integrated single-ended-to-differential low-noise amplifier. In *XXI Conference on Design of Circuits and Integrated Systems*, 2006.
8. W. Fan, A. Lu, L.L. Wai, and B.K. Lok. Mixed-mode s-parameter characterization of differential structures. In *Electronics Packaging Technology, 2003 5th Conference (EPTC 2003)*, pages 533 – 537, dec. 2003.
9. Hailong Zhu, Y.C.A. Ko, and T.T. Ye. Impedance measurement for balanced uhf rfid tag antennas. In *Radio and Wireless Symposium (RWS), 2010 IEEE*, pages 128 –131, jan. 2010.
10. Liguo Sun, Yinchao Chen, Kunquan Sun, and Wentao Wu. Analysis of differential balun circuits. *Signals Systems and Electronics (ISSSE), 2010 International Symposium on*, 1:1 –4, sept. 2010.
11. D.E. Bockelman and W.R. Eisenstadt. Combined differential and common-mode scattering parameters: theory and simulation. *Microwave Theory and Techniques, IEEE Transactions on*, 43(7):1530 –1539, jul 1995.
12. Yinchao Chen and Shuhui Yang. Mixed mode s-parameters analysis for differential networks in integrated circuits. In *Physical and Failure Analysis of Integrated Circuits, 2009. IPFA 2009. 16th IEEE International Symposium on the*, pages 268 –273, july 2009.
13. Kathleen D. Cebulka and Marialuisa N. McAllister. Transmittance matrices and flowgraph reduction. *Mathematical Modelling*, 6(5):389 – 400, 1985.
14. N. Schwerg. Symbolical analysis of rf-network problems using masons rule. *RADIOENGINEERING*, 21:892–897, 2012.
15. M. Neitola and T. Rahkonen. A fully automated flowgraph analysis tool for matlab. *Circuit Theory and Design, 2005. Proceedings of the 2005 European Conference on*, 1:I/185–I/188 vol. 1, 2005.
16. Skyworks Application Note. *"Matching Differential Port Device"*. Skyworks Solutions, Inc., October 2009.
17. Stephane Wloczysiak. *Match The Ports Of Differential Devices*. Materion, February 2010.
18. A.T. De Hoop. The n-port receiving antenna and its equivalent electrical network. Technical report, hilips Research Reports, 1975.

Part II
CAD tools for optimizing the design of inductors

It is not quiet difficult to recognize that our day life has changed drastically since the invention of the transistor. However, the transistor by itself has not been the driving force beneath the change, but its surprisingly scaling down. Predicted in 1965 by Gordon E. Moore, the typical geometrical feature of a MOS transistor, e.g. its gate, is reduced by a half every 18 months [1]. Nowadays, such dimension is 32nm that translates to a 1.170 billion of transistors in a Intel i7970 processor [2]. In this way, more and more functionalities can be integrated in a single chip. Such astonishing number of elements connected each other opens a more interesting question: how does an engineering team manage the design of actual ICs? The answer must be found in the Electronic Design Automation (EDA) arena.

Generally speaking, an EDA tool is any software program that assists the electronic designer in his/her tasks related to the development of electronic systems, either integrated or hybrid. Starting from the concept up to the end of a product, the designer (or team) must rationalize all tasks in a proper way to minimize the time to market constraint. The result is a design flow diagram that serves as a guideline at the different abstraction levels of the electronic design [3]. From the point of view of the design flow, EDA tools can be classified in two groups: platforms and specific tools. In one hand, platforms allow the management of a design flow by integrating the different specific tools at the different levels and enabling the introduction of future developed custom tools. Commercial examples are the Design Framework (dfwII) from Cadence, or Advanced Design System (ADS) from Agilent Technologies. With no doubt, this sector of the market is owned by big vendors. On the other hand, specific tools solve one specific task as it can be the entry of an schematic, the drawing of a layout, the simulation of a circuit, the checking of the design rules for fabrication or the extraction of parasitics, among others. The development of such tools are not only constrained to EDA vendors, but to research centers facing the new challenges in the microelectronic field.

In some way, the paradigm of EDA is to obtain a tool able to translate a system specifications into silicon just via a simple 'click'. Meanwhile the digital design is approaching this picture, the analog and analog-mixed design are quite far away. Moreover, the picture in the design of RF hybrid and integrated circuits is even closer to a handcrafted process due to the lack of advanced EDA tools. Commonly, it is necessary to predict the behavior of passive components (e.g. inductors, transformers,..) by using physical simulators (that are a side part of an EDA platform) from the beginning of a project. Therefore, the electronic designer changes its role to an electromagnetic engineer. Driven by the his/her expertise (or guru's black magic), many iterations must be performed between the different processes of the design flow that directly translates to a larger time to market and error prone design. This slow electromagnetic simulation process can be considered as the bottleneck in the design of RF systems.

Taking into account the previous picture, the field of EDA RF design shows many challenging opportunities for the development of specific tools, mainly related to the synthesis of passive components. Starting from a circuit parameter description such as a capacitance or an inductance value, the synthesis and electromagnetic evaluation of the component should be transparent to the user. In this way, she/he can focus

more on the electronic design itself for improving the yield of the product. This is the pursuit goal in this work through the detailed explanation of an analysis and synthesis tool for passive components. Thereby, in Chapter 4 an 'ab initio' technique for the meshing of planar radiofrequency and microwave circuits is described. This technique speeds up this common step in the synthesis of such components. Moreover, the technique is used in Chapter 5, where a simple bisection algorithm for the synthesis of compact planar inductors in LTCC technology is presented. The final algorithm is applied to the development of an inductor library for a LTCC process technology which last few minutes on a single CPU node.

References

1. G.E. Moore. Progress in digital integrated electronics. In *Electron Devices Meeting, 1975 International*, volume 21, pages 11–13, 1975.
2. H. Lakdawala, M. Schaecher, Chang tsung Fu, R. Limaye, J. Duster, Yulin Tan, A. Balankutty, E. Alpman, Chun Lee, S. Suzuki, B. Carlton, Hyung Seok Kim, M. Verhelst, S. Pellerano, Tong Kim, D. Srivastava, S. Venkatesan, Hyung jin Lee, P. Vandervoorn, J. Rizk, Chia-Hong Jan, K. Soumyanath, and S. Ramamurthy. 32nm x86 os-compliant pc on-chip with dual-core atom; processor and rf wifi transceiver. In *Solid-State Circuits Conference Digest of Technical Papers (ISSCC), 2012 IEEE International*, pages 62–64, 2012.
3. D. Leenaerts, G. Gielen, and R.A. Rutenbar. Cad solutions and outstanding challenges for mixed-signal and rf ic design. In *Computer Aided Design, 2001. ICCAD 2001. IEEE/ACM International Conference on*, pages 270–277, 2001.

Chapter 4
Ab initio adaptive meshing for planar passive component modeling

Abstract An ab initio technique for the meshing of planar radiofrequency and microwave circuits is described in this work. It is based on the analytical study of the current crowding phenomena that takes place inside the component. By using the mutual coupling inductive terms between metal strips, the ratio of the AC resistance due to proximity effects over the DC resistance can be evaluated for each metal strip. In such evaluation, it is not required an explicit solution of currents and charges at any part of the circuit. Then, the number of mesh cells assigned to a given metal strip depends on the value of the ratio. This technique is applied to the computation of losses in high Q inductors implemented in a Low Temperature Co-fired Ceramics Technology.

4.1 Introduction

This chapter is a review of the paper with the same title published in the conference *EuMC*[1].

System in Package (SiP) methodology enables the implementation of smart mobile communication systems where RF, analog and digital signals must coexist. To tackle the SiP design process, a correct combination of the available tools must be provided to designers in a well suited design flow [1]. Concerning RF and microwave planar circuits which can be found in RFICs and hybrid circuits, one of the most important features in SiP design flows is the introduction of electromagnetic (EM) field solvers. With them, passive components (e. g., coupled based transmission line components, inductors, transformers, etc) can be synthesized with the help of optimization algorithms. However, due to the number of iterations needed for the convergence of the algorithm into a realizable layout, the use of general pur-

[1] Sieiro, J. and Lopez-Villegas, J.M. and Vidal, M.N. and Osorio, J.A. and Carrasco, T. and Ahyoune, S., "Ab initio adaptive meshing for planar passive component modeling", Microwave Conference (EuMC), 2012 42nd European, 2012 International Conference on, 2012.

pose field simulators can be prohibitive in terms of computation time and resources because, at each iteration step, a new geometry must be formed and evaluated.

Nonetheless, computation speed up can be afforded by trading generality vs specialization of a particular method. One of the most amenable numerical methods for the development of fast solvers is the Partial Equivalent Electrical Circuit (PEEC), firstly introduced by Ruehli [2]. Specialization can take place at different parts of the method. Many excellent research works can be found in the literature [3, 4] addressing this challenge.

In the synthesis arena, fast computation translates into a mesh reduction of the numerical model without compromising accuracy. As instance, in the evaluation of high Q inductors, losses are mainly dominated by metal losses; thus, meshing errors become evident in the calculation of eddy currents distribution. This is specially remarkable when low loss substrates are used, a fact quite normal in nowadays technologies. Assuming an $O\left(N^2\right)$ solution time for planar solvers being, N the number of cells, the benefits of this mesh reduction are clear. One of the most popular techniques, due to its simplicity, is the use of edge-mesh elements which are based on a skin depth criteria [5]. A step further has been the development of higher order basis functions [6] and [7] that takes as a reference the high frequency current distribution of a stripline. From a topological point of view, both methods are similar because they only treat the geometry and physical phenomena locally.

In this work, we present a meshing technique that takes into account, at first order, the physical phenomena that takes place inside the whole component. The mesh is generated in three steps: (1) a coarse initial mesh, named DC mesh, is formed where the main coupling mechanisms between different device parts are accounted for; (2) for each cell of such mesh, an estimation of the current crowding phenomena is computed as the ratio of the equivalent AC resistance due to proximity effects, $R_{AC_{crowding}}$ over the DC resistance, R_{DC}; (3) the final mesh is build up by dividing each metal strip according to its associated DC mesh cell resistances ratio. It is important stressing that step (2) does not require the solution of the DC mesh (no matrix inversion is performed).

The paper is organized as follows. In Section 4.2, a planar inductor is selected to show that current redistribution depends on the metal strip location. Therefore, a simple analytical model is proposed to derive the $R_{AC_{crowding}}$ over R_{DC} ratio. In Section 4.3, the meshing algorithm is explained. As a practical case, the technique is verified against experimental data of high Q inductors implemented in a LTCC technology in Section 4.4. To final with, Section 4.5 concludes the work.

4.2 Current Crowding in Planar Circuits

Fig. 4.1 shows a sketch of a spiral inductor that is feed with an AC current connected between its input ports. Due to the magnetic flux density AC variations, induced currents will be generated over the conducting metal-strips of the device. This phenomenon is not only related to inductors, but to any other kind of planar component

based on metal strips, such as transformers and coupled transmission lines. Taking as a reference one of the metal strips, the contribution to the induced currents can be split in two main components: (1) related to the own magnetic flux field generated by the current passing through the metal strip, named *own-field* eddy currents; (2) associated to the magnetic flux field generated by the remaining metal strips over the given metal-strip, named *external-field* eddy currents.

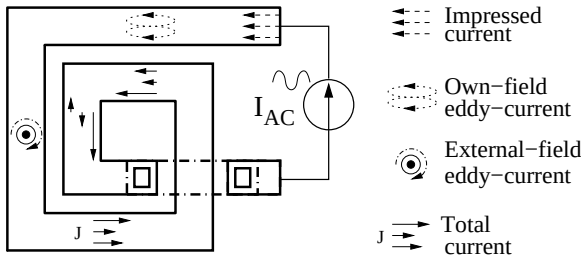

Fig. 4.1 Current crowding phenomena in an inductor.

The own-field eddy-currents distribution is a double mirrored symmetric loop having the center of symmetry located at the longitudinal axis of the metal strip. Any metal strip of the device will induce the same kind of own-field eddy-current distribution pattern independently of its location. For the external-field eddy-currents, the current density distribution is a single loop and, most important, it depends on the location of the metal strip in the layout of the component; i.e., the total current density distribution will be different for each metal strip of the device. Therefore, unless the EM behavior of the device is solved, it cannot be known a priori the shape of the total current distribution, $\boldsymbol{J}$, a fact that imposes an uncertainty on the number of cells to be selected for the mesh.

Actually, EDA softwares leave the responsibility of the mesh discretization to the user, though as an electromagnetic engineer. Tools that are closer to the electronic engineer try to automatize the generation of the mesh, letting few meshing parameters to be tune by the user. Among them, the most popular is the edge mesh option, that tries to compute the current distribution using a discretization based on a skin depth criteria or, equivalently, to the own-field eddy-current. Cells are pushed to the edges of the metal strip where the magnitude of $\boldsymbol{J}$ is higher. However, Fig. 4.2 shows an example where such scheme fails. It represents an axial cut of a 4 turns circular inductor evaluated at 1 GHz. Notice that each turn has a different current distribution pattern. Obviously, this fact points out that the mesh used for each turn should be adapted accordingly.

In the former discussion, one can be worried about $\boldsymbol{J}$ along the thickness of the strip. Due to the planar nature of the circuit, the external magnetic flux is perpendicular to the plane where the strips are placed; consequently, no external-field eddy-current can be build in the thickness-width plane of the strip. Thus the dependence of $\boldsymbol{J}$ in the direction of the thickness is associated to the pattern generated by the own-field eddy-currents.

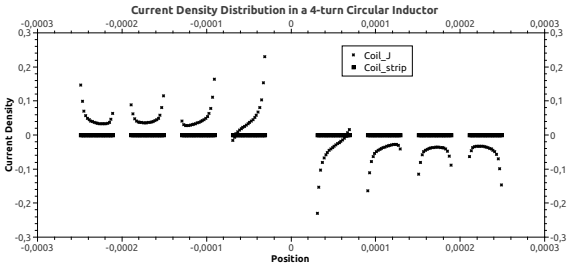

Fig. 4.2 Current density distribution of a circular inductor.

Having centered our interest on the external-field current distribution, Fig. 4.3a shows a simple mesh model of a strip section formed by two equal cells. An external magnetic field $B_{ext_{1,2}}$, generated by the rest of the circuit, transverses the strip in its length-width plane. As a consequence, a current ΔI is generated in each cell having opposite signs. Whereas superposition holds, ΔI is added to the impressed current I. Using PEEC, an equivalent electrical model of the mesh has been sketched in Fig. 4.3b. L is the autoinductance of each cell; R is its resistance value, which is twice the DC resistance value of the strip, named R_{DC} ; M is the inductive coupling between both strips. The remaining strips of the component are represented by their total autoinductance $L_e xt$ and resistance $R_{DC_{ext}}$. The inductive coupling between the external strips and the actual mesh cells is modeled by means of $M_{ext_{1,2}}$. The former circuit catch up the effect of the AC resistance. Notice that no ΔI is generated if there is no external coupling, nor AC excitation ($\omega = 0$), or if both couplings are equivalent. ($M_{ext_1} = M_{ext_2}$). This last condition can be better understood using a system of three coupled transmission lines, as the one shown in Fig. 4.4. If each conductor is driven with a current source of equal value, coupling factors M_{AB} and M_{AC} are equal by symmetry. Looking at the external magnetic field passing through the center conductor A, it is easy to see that it cancels out; thus no crowding effect is generated by the external field.

Now, the power loss in the metal strip of Fig. 4.3a can be calculated straight forward. Applying KVL to the mesh defined by the current ΔI in Fig. 4.3b, the ratio $\frac{\Delta I}{I}$ is given by

$$\frac{\Delta I}{I} = \frac{1}{2} \frac{j\omega \Delta M_{ext}}{4R_{DC} + j2\omega (L - M)}, \tag{4.1}$$

where it has been used the fact that $R = 2R_{DC}$, and $\Delta M_{ext} = (M_{ext_1} - M_{ext_2})$. From (4.1), the power loss is

$$P_{loss} = \frac{1}{2} |\Delta I| 4R_{DC} = \frac{1}{2} |I| R_{DC} \frac{\omega^2 \left(\frac{\Delta M_{ext}}{2R_{DC}}\right)^2}{1 + \omega^2 \left(\frac{L-M}{2R_{DC}}\right)^2}, \tag{4.2}$$

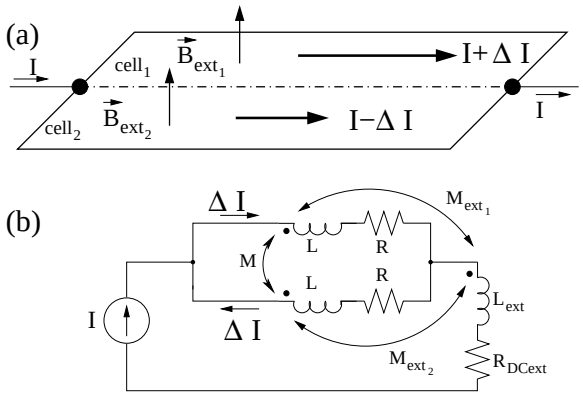

Fig. 4.3 (a) Simple mesh of a metal strip; (b) equivalent circuit model.

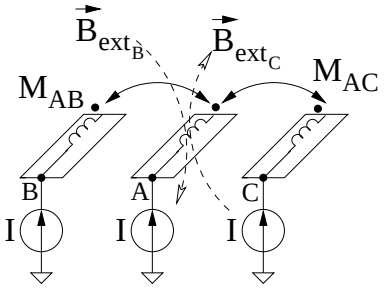

Fig. 4.4 Inductive coupling for three transmission lines.

and the ratio of the AC resistance due to the current crowding over the DC resistance can be expressed as follows

$$\frac{R_{AC_{crowding}}}{R_{DC}} = \frac{\omega^2 \left(\frac{\Delta M_{ext}}{2R_{DC}}\right)^2}{1+\omega^2 \left(\frac{L-M}{2R_{DC}}\right)^2}. \tag{4.3}$$

Notice that (4.3) can be evaluated without the knowledge of the actual current distribution inside the strip. It is only necessary to know the circuit parameters which are easily obtained if a PEEC method is chosen. It is worth noting the frequency behavior of (4.3). At low frequency, $R_{AC_{crowding}}$ rises at 40 dB/dec and, assuming $\Delta M_{ext} >> (L-M)$ in inductors, it equates the value of R_{DC} at $\omega = \frac{R_{DC}}{\Delta M_{ext}}$. Thus, each metal strip of the inductor will achieve this value at different frequencies. At higher frequencies, the double pole at $\omega = \frac{2R_{DC}}{(L-M)}$ saturates the AC loss term. This saturation must be seen as a limitation of the model (only two cells are used). Actually, one should expect a transition to a skin effect behavior, i.e. losses should increase as the square root of ω.

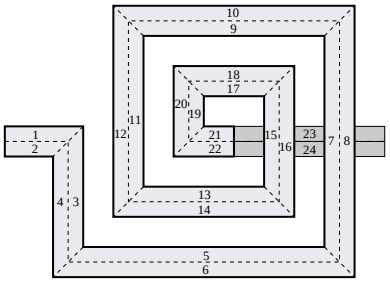

Fig. 4.5 DC mesh of the inductor for inductive coupling evaluation.

4.3 Meshing Algorithm

From (4.3), the idea underneath the meshing algorithm is quite simple. Metal strips having a lager ratio value will have more mesh divisions than those having a lower value. Ideally, if the ratio is found to be zero only one cell division should be necessary. However, this can be only true for the particular case $\omega = 0$. Otherwise, it is necessary to pick up the influence of the own-field eddy currents and the number of divisions across the width will be set to a minimum of three. Be aware that it is not possible to describe the effect of the own-field just with two divisions.

The algorithm is divided in three steps as follows. Firstly, starting from a mesh having two cell divisions across the width of each metal strip of the device, a first computation of the partial inductances and DC resistances is performed and recorded in an inductance matrix L_{ij} and a resistance array R_{DC_i}. To distinguish this mesh from the one to be obtained, it is named the DC mesh because no information about ω is supplied. The coupling capacitance terms are not taken into account because they are not related directly with current crowding effect, i.e. a quasi-static magnetic modeling of the device is performed as it can be deduced from the circuit in Fig. 4.3b. For this reason, it is not necessary to split long metal strips in submultiples of the wavelength, i.e. no delay effects are considered at this step in the meshing process.

Secondly, using a correlative numbering of the cell divisions as shown in Fig. 4.5, the values of ΔM_{ext}, L and M of the metal strip to be used in (4.3) i are given by

$$\Delta M_{ext_{strip}} = \sum_{j=1;j\neq\{i,i+1\}}^{2N} \left(L_{2i-1,j} - L_{2i,j}\right)$$

$$L_i = L_{2i,2i} \tag{4.4}$$

$$M_i = L_{2i,2i+1}$$

where N is the number of metal strips. Notice that the index i runs over metal strips and not over cell divisions. Selecting the frequency of interest ω, (4.3) is evaluated for each metal strip i using the values found in (4.4) and the corresponding R_{DC_i}. Now, the crowding effect has been quantified without solving explicitly the expected value of the current at any of the metal strips.

Thirdly, the final mesh of the model is built up. Fix the maximum number of cells for the model as a multiple of N. Notice that the minimum choice should be $3N$ in order to predict the effect of the own-field; a reasonable value could be $6N$ for a medium size inductor. Make a histogram of the ratio values obtained in the previous step and assign the number of cell divisions across the width for each metal-strip. A ratio value close to zero points out that there is no crowding effect due to the external-field (ω or $\frac{\Delta M_{ext}}{2R_{DC}}$ are almost negligible), thus only three cell divisions are required. When assigning larger values, it is important to use an odd number of divisions. Once the divisions across the width of each metal strip has been completed, divide the metal strips along its length using a wavelength criteria, e.g. the length of the cells should not be longer than $\lambda/20$ being λ the wavelength. To pick up effects such as the self resonant frequency of the inductor (SRF), it is worth mentioning that the adapted mesh is solved using both electric and magnetic couplings between mesh cells.

Fig. 4.6 shows an example of the mesh obtained for a five turns symmetrical square inductor at 1 GHz. Notice that internal turns are densely mesh because crowding effects are much more severe. Of course, cells do not need to be equally distributed along the width. However, a distribution based on a skin effect value can overestimate losses in the device.

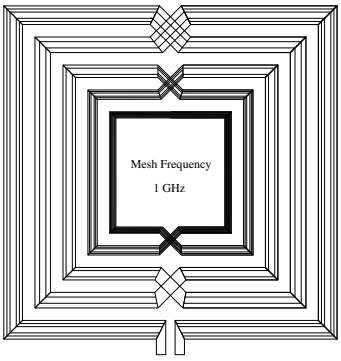

Fig. 4.6 Ab initio adaptive mesh of an inductor.

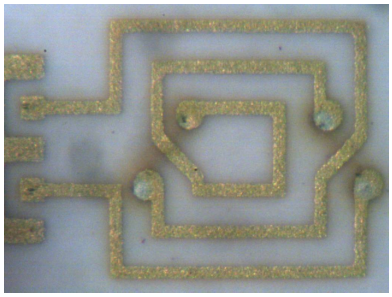

Fig. 4.7 Inductor implemented in LTCC technology.

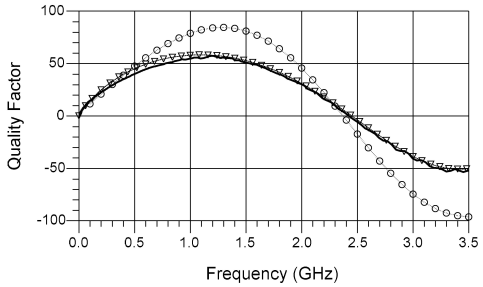

Fig. 4.8 Behavior of the Quality factor of the inductor: (solid) experimental data; ($\bigtriangledown$) adaptive mesh simulation; ($\circ$) edge-mesh

4.4 Evaluation of High Q Inductors

The former procedure has been applied to evaluation of the quality factor of a high Q inductor implemented in a LTCC technology using 6 dielectric layers. Each layer has a thickness about 90 μm after firing and is characterized by a relative permittivity of 6. Metal strips are made with Au having a post-firing thickness of 4 μm. In Fig. 4.7, it is shown a picture of the planar inductors fabricated with this technology.

The selected inductor for testing the meshing technique is a symmetric square type having three turns, a metal width of 150 μm, and a spacing between turns of 350 μm. It has been characterized using GSGSG-500 μm pitch differential coplanar probe. A SOLT calibration technique has been used to remove the influence of the measurement test set-up. Fig. 4.8 shows the comparison of the experimental data (solid line) with the simulation data using the proposed technique ($\bigtriangledown$). In addition, it has been included the simulation data from a method of moments field solver that uses the edge-mesh technique ($\circ$). Clearly, the technique presented is this work can evaluate the losses in the component with a higher accuracy.The time required for the evaluation of 251 points in frequency is about 2.5 s on a Intel ® T7500 processor.

4.5 Conclusions

This work has shown the feasibility of an ab initio adaptive meshing technique for planar RF and microwave circuits which is accurate enough to account for the losses in high Q planar devices. The mesh is generated in three steps: (1) assuming a quasi-static magnetic behavior, all inductive coupling terms between metal strips are computed; (2) an estimation of the current crowding phenomena is computed using equation (4.3); (3) the number of cell divisions across the width of a metal strip is assigned accordingly. To take into account the own-field current distribution, a minimum of three divisions is always forced. Additionally, an analytic model of the current crowding phenomena based on circuit parameters has been developed.

References

1. J. Park, J. Hartung, H. Dudek, "Complete front-to-back RF SiP design implementation flow", *Proceedings of the 57th Electronic Components and Technology Conference*, pp. 986-991, 2007.
2. A.E. Ruehli, "Equivalent circuit models for three-dimensional multiconductor systems", *IEEE Trans. Microwave Theory Tech.*, vol. 22. no. 3, pp. 216-221, 1974. 2000.
3. M. Kamon, M.J. Tsuk, J.K White, "FASTHENRY: a multipole-accelerated 3-D inductance extraction program", *IEEE Trans. Microw. Theory Tech.*, vol. 42. no. 9, pp. 1750-1758, 1994.
4. M. Niknejad, "Analysis, simulation and applications of passives devices on conductive substrates", Ph.D. dissertation, University of California at Berkeley, 2000.
5. D. De Zutter, J. Sercu, T. Dhaene, J. De Geest, F.J. Demuynck, S. Hammadi, C.P. Huang, "Recent Trends in the Integration of Circuit Optimization and Full-Wave Electromagnetic Analysis",*IEEE Trans. Microw. Theory Tech.*, vol. 52. no. 1, pp. 245-256, 2004.
6. M. Liu, T. Yu, W. Dai, "Fast 3-D inductance extraction in lossy multi-layer substrate", *IEEE/ACM International Conference on Computer Aided Design*, Mar. 2005, pp. 248254.
7. J.C. Rautio, "A conformal mesh for efficient planar electromagnetic analysis",*IEEE Trans. Microw. Theory Tech.*, vol. 52. no. 1, pp. 257-264, 2004.

Chapter 5
Synthesis of compact planar inductors in LTCC technology

Abstract A simple bisection algorithm for the synthesis of compact planar inductors in LTCC technology is presented in this work. It is based on a set of heuristic rules obtained from the study of the electromagnetic behavior of these planar devices. By using a bisection method, the number of iterations is kept moderately low. In order to speed up analysis at each step, a fast planar electromagnetic solver is used which is based, once again, on the knowledge of the synthesized component. The algorithm is applied to the development of an inductor library for a LTCC process technology which last few minutes on a single CPU node.

5.1 Introduction

This chapter is a review of the paper with the same title published in *SMACD*[1] and awarded with the best paper award[2].

In the last years, there has been an increasing interest for the development of RF electronic design automation (EDA) tools boosted by the growing demand for wireless applications. The paradigm is the translation of system specifications into an integrated or hybrid technology just via a single mouse 'click'. Whereas EDA tools in digital design are mature enough to handle a billion transistor circuit, they are in their infancy in the RF/analog arena. Currently, the design flow diagram followed by most EDA platforms is formed by two iterative procedures [1], both using time-consuming electromagnetic (EM) simulators. The first one is related to the synthesis of passive components, whereas the second is set to pick up the EM couplings of dis-

[1] International conference on synthesis, modeling, analysis and simulation methods and applications to circuit design.

[2] Sieiro, J. and Lopez-Villegas, J.M. and Osorio, J.A. and Carrasco, T. and Vidal, M.N. and Ahyoune, S., "Synthesis of compact planar inductors in LTCC technology", Synthesis, Modeling, Analysis and Simulation Methods and Applications to Circuit Design (SMACD), 2012 International Conference on, 2012.

tant parts of the circuit. Clearly, the synthesis loop is recognized as the bottle-neck of the RF design process.

First works towards the synthesis of passive components were related to inductors. By introducing the knowledge of their EM behavior and supported on EM solvers, tapered inductor geometry optimization was developed in [2]. Its main advantage is a fast convergence because the searching process is driven deterministically. However, for a successful application of this algorithm, the designer must have EM expertise. For this reason, different automation tools have been proposed [3]-[7]. Their common point is the definition of the synthesis as a complex multi-objective optimization problem. Most methodologies are based on selecting best individuals from a population [3] which implies a large number of EM simulations. For reducing the number of iterations, an expert system rule-set has been proposed in [4]. Nieuwoudt and Massoud [5] introduce the use of Pareto-optimal surfaces, firstly developed in mixed-signal synthesis [6]. Improvements of this methodology is found in [7].

As it has been pointed out in [7], the challenge of all such methodologies is to obtain an optimum trade-off between efficiency and accuracy. Efficiency is related to the number of iterations needed in the optimization method and the time required for analysis at each iteration step. High accuracy demands the use of EM solvers which opposes to efficiency. Although the previous multi-objective optimization methods have shown a good performance, efficiency can be improved by far, without compromising accuracy, if knowledge related to the component is employed. This is the guideline followed in this work. Instead of pursuing a general purpose synthesis tool that can handle several objectives, a specialized one is developed. The EM behavior of the component, its technology implementation and its targeted application are used in order to simplify both analysis and synthesis procedures. This alternative must be understood as a second type of trade-off, i.e. generality vs specialization of the tool. To show the actual improvement in efficiency, the targeted application is devoted to the synthesis of a library of compact inductors requiring a minimum area implemented in a low temperature co-fired ceramic (LTCC) technology. These components can be used to build filters, RF chokes or any other basic RF building blocks in heterogeneous integrated systems.

In Section 5.2, basic parameters and figures of merit describing the EM behavior of the inductor and Q factor requirements related to circuit application are reviewed. Using information knowledge about inductors, improvements in the EM solver are highlighted in Section 5.3. Section 5.4 shows the synthesis algorithmic procedure applied to compact inductor topologies. Concluding remarks are presented in Section 5.5.

5.2 Inductor Basic Parameters

In circuit theory, an inductor is a lumped device able to store an amount of magnetic energy. The inductor is supposed to be ideal: no loss, linear behavior and infinite fre-

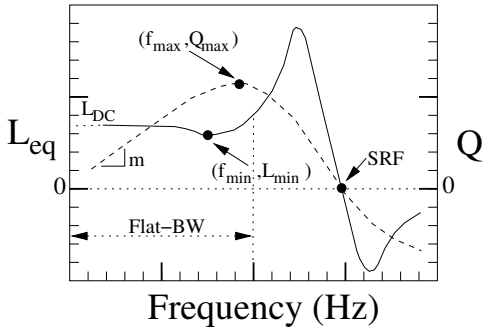

Fig. 5.1 Main parameters and figures of merit for L_{eq} (solid) and Q (dashed).

quency range of use. Actual implementations are far away from this picture. Fig. 5.1 shows the effects of parasitics on the equivalent inductance value (solid line) and on the quality factor (dashed line) over a wide frequency range (up to the self resonance) for a linear inductor. The next parameters can be defined that collects the most important features of the previous plots:

L_{eq} is the inductor equivalent inductance defined as

$$L_{eq} = \frac{imag\,(Z_L)}{j\omega}, \tag{5.1}$$

being Z_L the differential impedance of the inductor.
Q is the quality factor defined as

$$Q = \frac{imag\,(Z_L)}{real\,(Z_L)}. \tag{5.2}$$

L_{DC} is the extrapolated L_{eq} value at DC; currently, it is associated to the ideal behavior of the component.
SRF is the frequency at which L_{eq} and Q are null; from this frequency value, the inductor behaves as a capacitor.
(f_{min}, L_{min}) is the local minimum of L_{eq} that can exist before SRF due to the current redistribution in metallizations and substrate.
$Flat-BW$ is the frequency range at which the condition $L_{DC} > L_{eq}(\omega) > L_{min}$ holds.
R_{DC} is equivalent resistance value accounting for losses at the DC limit. It can be extracted from the slope m of Q at very low frequency.
(f_{max}, Q_{max}) indicates the point where Q peaks and it is related to high frequency losses.

Another non-electrical characteristic (of utmost importance in integrated technologies) is the total area A used for the implementation of the inductor. L_{eq}, Q and

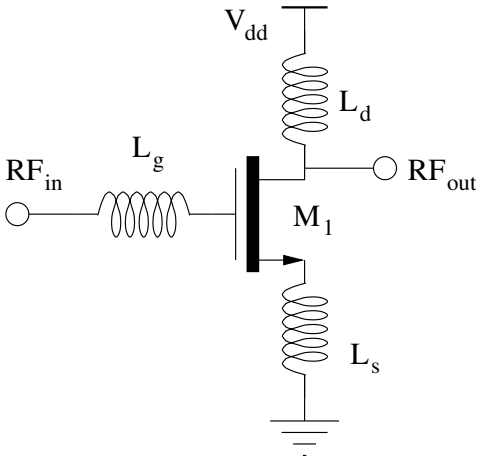

Fig. 5.2 Schematic of a single-ended LNA with source degeneration.

A are the main parameters used by a designer for the selection of an inductor. To gain a deeper insight on the problem related to the synthesis of inductors, Fig. 5.2 shows a typical configuration of a single ended Low Noise Amplifier (LNA) based on a inductor degenerated common source topology (for differential topologies, the passives can be substituted with transformers). To simultaneously match noise and gain, the circuit has three inductors, each having an specific function:

- L_s provides a way to set the real part of the minimum noise impedance equal to input impedance, but without increasing the overall noise figure of the circuit and neither decreasing to much the gain. L_s must be a low inductance and high-Q inductor.
- L_g cancels out the capacitive input of the LNA. However, taking into account the final application, it can be a high-Q or medium-Q inductor. For example, if electrostatic discharge (ESD) is a concern, a medium-Q inductor should be chosen; if noise figure is the main concern, a high-Q inductor must be selected. The inductance value spans over a wide range because it depends on the selected dimensions of active devices.
- L_d provides the voltage gain as it actuates as a current source for AC. Typically, it must have a large inductance value for increasing the gain. In low-power applications, a high-Q inductor could be a good choice; however, stability issues and output matching can require the use of a lower Q inductor.

Starting from the specifications of the LNA application, the designer must found a suitable combination of requirements for L_s, L_g and L_d. In fact, if multi-objective optimization methodology is employed, it should be applied to the whole LNA design [8]. Otherwise, the designer can be trapped in a trial and error process at the schematic level of the LNA. Deterministic methods, if accurate and fast enough, can provide a framework where the synthesis is transparent to the user. The passive com-

ponent can be inserted as any other component inside the circuit schematic. From this point of view, the designer is completely focused on the circuit design itself. Such scenario can be affordable with the introduction of additional weak restrictions of the technology. In heterogeneous integration or packaging platforms for RF building parts, the implementation of inductors can be restricted to a minimum area without a large penalty on Q, i.e. such inductors should not be though as low Q (Q values above 50 have been reported in many LTCC technologies).

5.3 EM Fast Solver

Analysis is at the core of any synthesis methodology and its performance impacts on the accuracy and efficiency of the tool. When dealing with planar components, 2.5-D solvers are preferred because it is only necessary to mesh the source region. Substrate effects are collected by numerical computation of its Green's function. Most available EM solvers are though as general purpose allowing the analysis of radiation and propagation phenomena in any kind of multi-layered substrate configuration. However, for the analysis of inductors and other passive components in LTCC technologies, many simplifications can be done at different levels of the solver in order to speed the computation time, but without loosing accuracy.

5.3.1 Solution space and mesh reduction

As far as conductive regions are involved in the implementation of passive components, the solution space is formed by the current $\boldsymbol{J}$ and charge distribution ρ. These four unknown components at each mesh cell can be reduced to only two by assuming two considerations. First, metal strips are considered infinitely thin; thus the z component of $\boldsymbol{J}$ can be dismissed. For via modeling, a lumped equivalent model is used. Second, the main component of the current density vector is parallel to the voltage gradient applied at DC. As shown in Fig. 5.3, only the current component along the length of the metal strip needs to be evaluated. From a mesh point of view, the number of divisions across the width of a metal strip region can be estimated a priori. Using a simple lumped model formed by two cells along its longitudinal axes, the ratio of the losses due to the current crowding over the DC losses is given by

$$\frac{R_{AC}}{R_{DC}} = \frac{\omega^2 \left(\frac{M_{ext}}{2R_{DC}}\right)^2}{1+\omega^2 \left(\frac{L-M}{2R_{DC}}\right)^2}, \tag{5.3}$$

where L the autoinductance of each cell, M is the inductive coupling between both cells, M_{ext} is the coupling of any external circuit on to the metal strip, R_{DC} is the

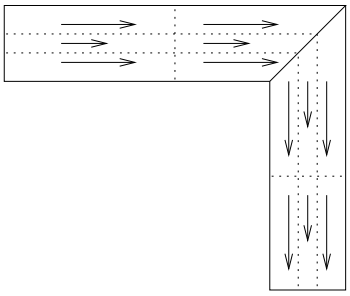

Fig. 5.3 Component order reduction of the current density distribution.

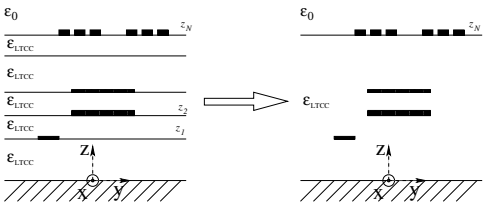

Fig. 5.4 LTCC substrate definition for Green's function computation.

resistance value of the metal strip, and ω stands for the angular frequency of interest. In this way, it is possible to reduce the overall number of cells without compromising the accuracy in the determination of losses in metal regions.

5.3.2 Green's function computation

One simplification made in many field solvers in the computation of the substrate Green's function is to dismiss the influence of any retarded signal. With this assumption, no radiation effects are considered which is the case in many passive components analysis. Therefore, the scalar and vector potential can be decoupled.

Nevertheless, a major reduction in computation time can be afforded if only a subset of multi-layered substrates is considered (which covers most hybrid technologies). Experienced EM designers know that an increase in the number of layers substrate definition increases considerably the time required for the analysis of a given layout. In Fig. 5.4, a sketch of a typical LTCC substrate is depicted. If all layers are of the same material, which is usually the case, it is possible to accelerate the computation of Green's function by just computing analytically two functions for all the substrate. Strictly speaking, it is necessary to find four functions. However, by virtue of the Lorentz reciprocity theorem, the role of point charge source and observation point (i.e. the point where the potential is calculated) can be reversed.

The procedure for the calculation of Green's function analitycally is based on a Hankel's transform that allows to find a series expansion in terms of a set of dis-

tributed image charges. The main advantage of this procedure is that the series can be truncated according to the relative distance between mesh cells. In addition, it is possible to evaluate the error of the truncation. As an example, the scalar potential Green's function of the multi-layered substrate shown in Fig. 5.4 for a point charge located at $z = z_N$ (boundary between LTCC and air) is given by

$$4\pi\varepsilon G_I(r,z) = \left[\frac{1}{\sqrt{r^2+(z-z_N)^2}} - \frac{1}{\sqrt{r^2+(z+z_N)^2}}\right] + \\ + \sum_{i=1}^{\infty}(-k)^i \left[\frac{1}{\sqrt{r^2+(z-z_N(1+2i))^2}} - \right. \\ \left. - \frac{1}{\sqrt{r^2+(z+z_N(1+2i))^2}}\right] \tag{5.4}$$

where r and z are the coordinates of the observation point, $k = \frac{\varepsilon_{LTCC}-\varepsilon_{air}}{\varepsilon_{LTCC}+\varepsilon_{air}}$ and $\varepsilon = \frac{\varepsilon_{LTCC}+\varepsilon_{air}}{2}$, ε_{LTCC} and ε_{air} are the relative permittivities of LTCC substrate and air, respectively. Notice that if both materials have the same permittivity, the second term in (5.4) cancels out, i.e. $k = 0$. With this Green's function expression, the coefficients of the circuit matrix are calculated directly.

5.4 Compact Inductor Synthesis

Thanks to the fast analysis tool, it is possible to synthesize compact inductors in a quite straight forward way. The flux diagram is shown in Fig. 5.5. The starting point is the electrical data specified by the user, i.e. the required L_{eq} at frequency ω_0, and available area A. From the point of view of the design rules, a compact inductor must use minimum geometry features (metal width and separation between metals). The searching algorithm is based on a double loop. The first one finds the minimum number of turns for synthesizing the required L_{eq}. By modifying the central hole of the inductor, the second loop is implemented as a bisection method. The initial interval of the bisection method is $[L_{N_1}, L_{N_2}]$, being $(L_{N_1} < L_{eq})$ the inductor obtained from the first loop iteration and L_{N_2} is an inductor with the property $(L_{N_2} > L_{eq})$ and the same number of turns of L_{N_1}. The parameter tol measures the difference between the required and actual synthesized value.

The algorithm detects non-realizable inductors. At the level of the first loop, if $(L_N > L_{eq})$ for $N = 1$, the inductor is not realizable because L_N is the smallest inductor that can be printed in the technology. Once the second loop has found the geometry of the inductor, it must be analyzed in a wide frequency range in order

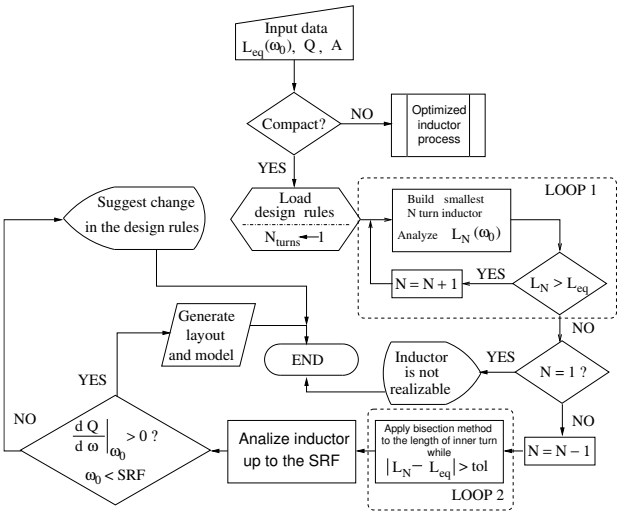

Fig. 5.5 Synthesis algorithm for compact inductors.

to check that the synthesized inductor has its L_{eq} value inside the flat bandwidth region. Notice that before SRF one can find two frequency points with the same L_{eq} value. If the algorithm has been trapped in the closest frequency to SRF, the solution is not valid. This fact can be detected with two signatures:

1. ω_0 is below SRF.
2. The slope of the Q factor at ω_0 is positive.

Since smaller inductors do have higher SRF, the inductor is not realizable if both conditions are not met. Remind that the algorithm has done the search from the smallest inductor. Sometimes, when the first condition is met but not the second, it is still possible to find an inductor by increasing a little bit the separation between metal strips, thus capacitive couplings are minimized without changing too much the inductance value. This possibility is suggested to the user; but the algorithm does not compute it because a change on the design rules should be perform (the user must be aware of such change). Using the previous procedure, Fig. 5.6 shows the length side of the square area required for the implementation of an inductor versus its equivalent inductance value, computed at 100 MHz. 20 inductors, ranging from 1 nH to 20 nH, have been synthesized in less than 100 seconds using an Intel T7500 processor at 2.2 GHz and Linux OS platform.

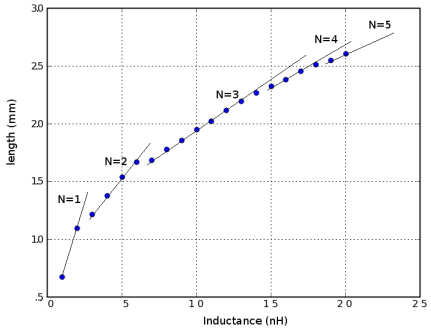

Fig. 5.6 Side of square area vs ranging from 1nH to 20nH.

5.5 Conclusions

A bisection algorithm for the synthesis of compact planar inductors in LTCC technology has been proposed. Thanks to the use of fast EM solvers and heuristic rules a library set of 20 inductors has been obtained in less than 100 seconds.

References

1. D. Leenaerts, G. Gielen and R.A. Rutenbar, "CAD solutions and outstanding challenges for mixed-signal and RF IC design", *Proc. IEEE/ACM Int. Conf. Computer Aided Design*, pp. 270-277, 2001.
2. J.M. Lopez-Villegas, J. Samitier, C. Cane, P. Losantos, "Improvement of the quality factor of RF integrated inductors by layout optimization", *IEEE Trans. Microwave Theory Tech.*, vol. 48, pp. 7683, Jan. 2000.
3. S. Mukherjee, B. Mutnury, S. Dalmia, M. Swaminathan, "Layout-level synthesis of RF inductors and filters in LCP substrates for Wi-Fi applications", *IEEE Trans. Microw. Theory Tech.*, vol. 53, no. 6, pp. 2196-2210, Jun. 2005.
4. S. Bantas, P. Zampoukis, "Expert-system based integrated inductor synthesis and optimization", U.S. Patent 2010/0088657 A1, Apr. 8, 2010.
5. A. Nieuwoudt, Y. Massoud, "Variability-aware multilevel integrated spiral inductor synthesis",*IEEE Trans. Comput.-Aided Design Integr. Circuits Syst.*, vol. 25, no. 12, pp. 2613-2625, Dec. 2006.
6. T. Eeckelaert, T. McConaghy, G. Gielen, "Efficient multiobjective synthesis of analog circuits using hierarchical Pareto-optimal performance hypersurfaces", *in Proc. Des., Autom. and Test Eur. Conf. and Exhib.*, Mar. 2005, pp. 248254.
7. B. Liu, D. Zhao, G. Gielen, "Synthesis of Integrated Passive Components for High-Frequency RF ICs Based on Evolutionary Computation and Machine Learning Techniques",*IEEE Trans. Comput.-Aided Design Integr. Circuits Syst.*, vol. 30, no. 10, pp. 1458-1468, Oct. 2011.
8. C. Sanchez-Lopez et al., "A bottom-up approach to the systematic design of LNAs using evolutionary optimization", *XIth Int. Workshop on Symbolic and Numerical Methods, Modeling and Applications to Circuit Design (SM2ACD)*, Nov. 2010.

Part III
Practical case - Design of a single-ended-to-differential low noise amplifier

Chapter 6
CMOS single-ended-to-differential low noise amplifier

Abstract In this chapter the design of a low-power single-ended-to-differential low noise amplifier (LNA) is explained based on the theory developed on the previous chapters. The circuit has been designed and optimized to be part of a receiver that follows IEEE 802.15.4 standard, thus LNA performances are based on a complete system characterization rather than in a 50 Ω setup. In order to minimize power consumption, active loads and currents mirrors have been replaced by optimized inductors and transformers. The LNA has been implemented using a 0.35 µm RFCMOS technology. Measured performances are a noise figure of 4.3 dB, a power gain of 21 dB, and a phase balance of $180°\pm1°$. Regarding non-linear behavior, the obtained 1 dB-compression point is -9.5 dBm and intermodulation intercept point is -3 dBm, meanwhile dissipating 6 mA from 1.5 V supply voltage.

6.1 Introduction

This chapter is an extension of the paper with the same title published in DCIS06[1] and later selected to be published in a special edition of *Integration, the VLSI journal* of Elsevier[1]. Now, some explanations have been reviewed and complemented more accordingly with the developed theory in the previous chapters.

In a typical radio receiver, low-noise amplifier (LNA) is one of the key components because it tends to dominate the sensitivity and noise figure (NF) of the whole system [2]. This sensitivity is directly related to both active and passive devices available in a given technology. Thus, the chosen technology will have a high impact on the final specs that could be achievable. However, the specifications of the communication standard and product cost as well as small size, level of integration, power consumption are additional constraints that will complicate the technology selection process. Actually, in high performance applications, LNA noise figures

[1] Conference on Design of Circuits and Integrated Systems. Barcelona, 22-24 November 2006

below 2 dB have been demonstrated [3, 4, 5] using integrated technologies such as SiGe, GaAs or improved CMOS (micromachining, SOI, thick metal $> 4\mu$m, etc.).

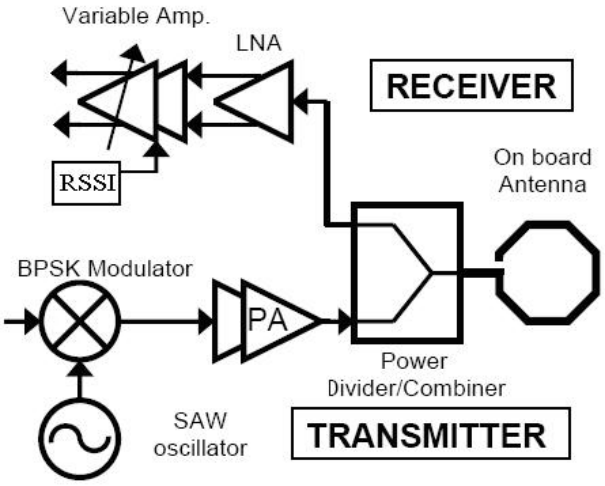

Fig. 6.1 Input and output stage of the transceiver.

Nonetheless there are applications where the system specifications are relaxed, e.g. in wireless sensor networks, enabling the use of conventional CMOS processes. The LNA proposed in this work is a part of the RF front-end receiver, shown in Fig. 6.1, of a reduced functional device (RFD) intended to work in compliance with the IEEE802.15.4 low-frequency band (European 868-868.6 MHz) [6]. The key characteristic of the standard is its protocol simplicity and flexibility providing a reliable data transfer (20 Kbps in European 868.3 MHz band) in a short-range operation (typically within a range of 10 m). A summary of the most important specifications of the standard is shown in Table 6.1.

Table 6.1 IEEE 802.15.4 standard specifications.

Quantity	Value
Sensitivity	-92 dBm
BER	6.2510^{-5}
Max. Power Input	-20 dBm
Channel bandwidth	600 KHz

Due to the final application, i.e. a wireless sensor network, the RFD units must be tiny, dissipate a small amount of power, and have a very low final cost. Taking

into account such constraints, RFCMOS 0.35 μm is a good technology option for the implementation of a complete transceiver of the RFD unit.

Once the framework has been established, the designer must face three challenges. First, the choice of a communication system architecture that will have a strong influence on the possible circuit topologies of the LNA for achieving the specifications of the standard. Second, the design should identify and apply the best design methodologies and strategies for achieving a low-voltage low-power (LVLP) circuit. And third, once the technology has been fixed, the LNA performance depends strongly on the quality of the passive components; therefore, the designer has to be able to evaluate their behavior using full-wave electromagnetic simulators.

In this work, the selected transceiver architecture uses one single-ended antenna for both transmission and reception paths that are split using an external switch, as shown in Fig. 6.1. To minimize the effects of the common-mode noise, e.g. digital switching noise, the received signal must be processed differentially. Therefore, this assumption points out the need of a single-ended-to-differential LNA design. Commonly, out of chip passive BalUn has been used to convert single-ended signals to differential signals. Unfortunately, it introduces losses increasing the system noise figure. To avoid these mentioned drawbacks, an active topology is preferred in this work. Moreover, to compensate the dynamic range of the complete system without increasing the total power consumption, a fully differential variable gain amplifier has been connected to the LNA output. With this selected architecture, the system specifications are translated into the LNA block as a maximum NF of 7 dB, a minimum gain of 18 dB, and an input intercept point to the third harmonic (IIP3) of -10 dBm. Of course, the LNA must dissipate the lower power consumption. In order to accomplish this last request, the supply voltage has been reduced to 1.5 V, considerably lower than the standard value of 3.3 V for a 0.35 μm technology where nominal threshold voltages are around 0.5 V. This voltage reduction supposes a clear penalty for the designer who has to reduce the possible number of stacked transistors, with the corresponding reduction of some of the basic LNA performances, e.g., gain, NF, or reverse isolation, among others.

To avoid this drawback, for the first time the substitution of resistive or active loads, as well as current mirrors by optimized on-chip inductors and transformers [7] is proposed. Considering this framework, RF CMOS accurate models for such inductors and transformers are not always available. Therefore, the designer has to be able to evaluate the performance of these integrated passive using full-wave electromagnetic simulators, particularly if layout optimization techniques are used. This disadvantage becomes a benefit, due to the fact that the designer can obtain the best component for each application. In the work presented hereafter, the benefits translate in achieving the best resonance tank for a specific frequency, the exact inductance value and the higher quality factor Q for a degeneration inductor beyond the inductor library supplied by the foundry manufacturer. Moreover, each inductance of the LNA has been designed to obtain the best performance depending on its specific application, i.e., as a load, RF chock, AC current source, input/output matching or source degeneration. Actually, the use of the optimized component [8] allows a complete monolithic integration of a compliance solution. In addition, in order to

reduce simulation time, synthesis tools developed in Chapter 4 and Chapter 5 have been used as a first synthesis step.

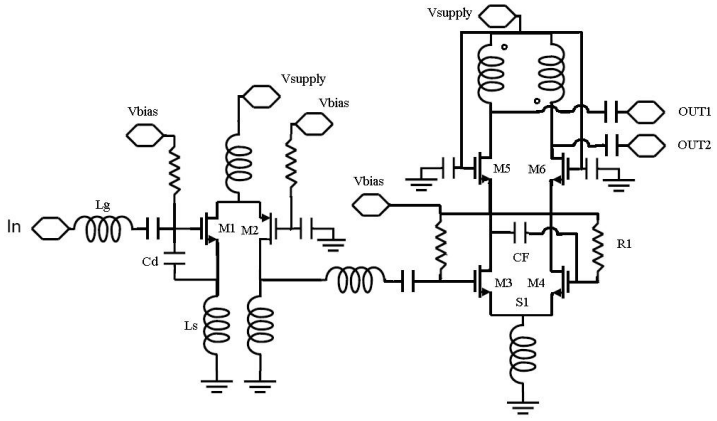

Fig. 6.2 Schematic of a Single Ended to Differential Low Noise Amplifier.

The schematic of the proposed LNA is shown in Fig. 6.2. Since, it is based on a three-port device, the basic expressions for the analysis of amplifiers in terms of S-parameters is developed, for the first time, in Section 6.2. Such expressions represent the exact mathematical formalism without any approximation. As can be seen in Fig. 6.2, the first stage is based on a folded cascode topology [9]. This topology has to main advantages. First, it allows a low-power dissipation using a low-voltage supply. And second, as it will be explained in Section 6.3, using power constraint simultaneous noise and input-matching impedance design technique (PCSNIM), the best trade-off between power match and noise figure can be achieved. Regarding the second stage, it is based on a differential cascode structure that supports the single-ended-to-differential conversion [10]. Thus, the analysis of this topology is explained in Section 6.4. As a complete monolithic solution, Section 6.5 presents the LNA characterization process, measurements are compared with simulations showing the initial proposed performances. Finally, Section 6.6 exposes the conclusions of the work.

6.2 Design of a three-port LNA using mixed-mode S-parameters

The theory developed in Chapter 3 is applied to the design of a single-ended to differential low noise amplifier. Notice that, though these methods are typically applied to active devices, e.g. the design of amplifiers, they are equally valid for the use with passive networks. Moreover, the expressions obtained extend the current theory to solve a general case, where the device can be a non-symmetric device. Nonetheless, the general solution is continuously compared with the classical two-

port techniques. Thus, it is demonstrated that the traditional two-port expressions are recovered, if circuit is ideally symmetric. Likewise it was done in Chapter 3, it is necessary to obtain the transducer power gain, constant gain circles, and stability circles. These concepts have to be redefined, and similar expression to the classical ones can be found in terms of mixed-mode S-parameters. However, the noise figure is out of the scope of this thesis, and it will be considered that, since the three-port device has a unique input port, existing theory is valid. Moreover, as it has been already mentioned, dual expressions can be obtained for common-mode in the case that the device is used for a common-mode purpose.

Thereby, Fig. 6.3 shows a three-port device topologically represented. Thus, a single-ended source launches a single-ended signal which is transformed to a differential(common)-mode signal by the amplifier. In the case of an ideal amplifier, no common-mode is generated and design expressions are irrespective of the common-mode port. In this ideal case, classical expressions can be simply re-written in terms of input-output S-parameters matrix (i.e. in our case S_{1-d} submatrix). However, in a real case, component mismatching, or simply the design configuration can introduce asymmetry. In this case, the simplified assumption is not valid and the exact mathematical development, deduced in Chapter 3, has to be used. It is important to mention that, regarding to Fig. 6.3, for our specific case, each physical port is referenced to 50 Ω. Thereby, the reference input impedance is 50 Ω. Meanwhile, differential and common-mode reference impedances are 100 Ω and 25 Ω respectively.

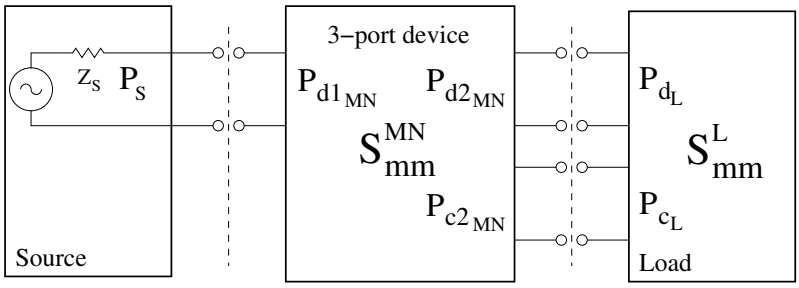

Fig. 6.3 Topological connection of a three-port device.

To start with, in the design of amplifiers, transducer power gain is the parameter that better describes the gain of a device. The most general expression can be derived if Fig. 6.3 is represented by means of signal flow graphs. In the case of a three-port device, the SGF is represented in Fig. 6.4. As it has been previously shown, the transducer power gain is defined as the power delivered to the differential load over the power available in the source. The ratios b_d/b_s and a_d/b_s can be found by applying Mason's rules. After properly arranging, they read as follows

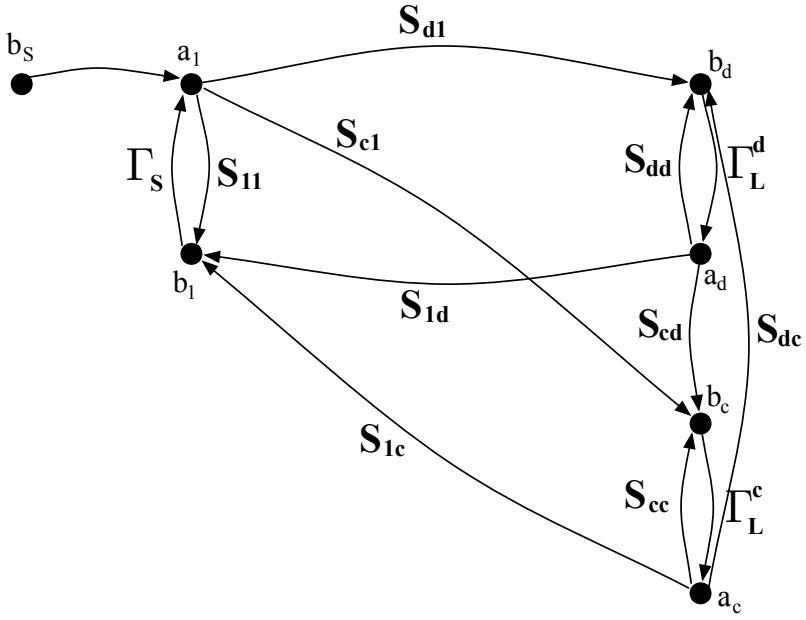

Fig. 6.4 Signal flow graph for a 3-port device in mixed-mode S-parameters.

$$\begin{aligned}\frac{b_d}{b_s} &= \frac{S_{d1} - \left|A_{1,d}\right| \Gamma_L^c}{\left[1 - S_{dd}\Gamma_L^d - S_{cc}\Gamma_L^c + |S_{mm}|\Gamma_L^d\Gamma_L^c\right]\left[1 - \Gamma_s\Gamma_1\right]} \\ \frac{a_d}{b_s} &= \frac{S_{d1} - \left|A_{1,d}\right| \Gamma_L^c}{\left[1 - S_{dd}\Gamma_L^d - S_{cc}\Gamma_L^c + |S_{mm}|\Gamma_L^d\Gamma_L^c\right]\left[1 - \Gamma_s\Gamma_1\right]}\Gamma_L^d,\end{aligned} \tag{6.1}$$

where $\left|A_{1,d}\right|$ equals $S_{d1}S_{cc} - S_{dc}S_{c1}$. Thus, transducer power gain is calculated using the next expression

$$G_t = \left(1 - |\Gamma_s|^2\right)\left(\left|\frac{b_d}{b_s}\right|^2 - \left|\frac{a_d}{b_s}\right|^2\right). \tag{6.2}$$

Replacing (6.1) in (6.2) and after some algebra, G_t reads as follows

$$G_t = \frac{1 - |\Gamma_s|^2}{|1 - \Gamma_s\Gamma_1|^2}\left|\frac{S_{d1} - \left|A_{1,d}\right|\Gamma_L^c}{1 - S_{cc}\Gamma_L^c}\right|^2 \frac{1 - \left|\Gamma_L^d\right|^2}{\left|1 - \Gamma_d'\Gamma_L^d\right|^2}, \tag{6.3}$$

where Γ_1, already found in (3.37), is rewritten here

$$\Gamma_1 = \frac{S_{11} - |S_{1-d}|\Gamma_L^d - |S_{1-c}|\Gamma_L^c + |S|\Gamma_L^d\Gamma_L^c}{1 - S_{dd}\Gamma_L^d - S_{cc}\Gamma_L^c + |S_{mm}|\Gamma_L^d\Gamma_L^c}. \tag{6.4}$$

The co-factors $|S_{1-d}|$, $|S_{1-c}|$, $|S_{mm}|$ and $|S|$ correspond to the determinants of the next matrices

$$\begin{aligned} |S_{1-d}| &= det\left|\begin{pmatrix} S_{11} & S_{1d} \\ S_{d1} & S_{dd} \end{pmatrix}\right|, \quad |S_{mm}| = det\left|\begin{pmatrix} S_{dd} & S_{dc} \\ S_{cd} & S_{cc} \end{pmatrix}\right| \\ |S_{1-c}| &= det\left|\begin{pmatrix} S_{11} & S_{1c} \\ S_{c1} & S_{cc} \end{pmatrix}\right|, \quad |S| = det\left|\begin{pmatrix} S_{11} & S_{1d} & S_{1c} \\ S_{d1} & S_{dd} & S_{dc} \\ S_{c1} & S_{cd} & S_{cc} \end{pmatrix}\right|. \end{aligned} \tag{6.5}$$

Meanwhile, the reflection coefficient Γ_d' in the third term of (6.3) corresponds to the differential output reflection coefficient but when input port is connected to the reference impedance Z_0 (i.e. Γ_S equals zero). In this way, from (3.39) which read as

$$\Gamma_d = \frac{S_{dd} - |S_{1-d}|\Gamma_L^1 - |S_{mm}|\Gamma_L^c + |S|\Gamma_L^1\Gamma_L^c}{1 - S_{11}\Gamma_L^1 - S_{cc}\Gamma_L^c + |S_{1-c}|\Gamma_L^1\Gamma_L^c}, \tag{6.6}$$

when Γ_S equal zero, it results as follows

$$\Gamma_d' = \frac{S_{dd} - |S_{mm}|\Gamma_L^c}{1 - S_{cc}\Gamma_L^c}. \tag{6.7}$$

Notice that (6.3) is formed by three differentiated terms, similarly to the classical two-port expression in (1.7). The first and third terms clearly represent the input and output mismatching degree. As in the two-port case, it is always possible to find a source and load impedance which minimize both factors. If the device is unconditionally stable, complex conjugate of input and differential output impedances correspond to such values. Likewise, the second term represents a gain. Again, it can be seen that, if there is no power flowing into or from the common-mode port (i.e. S_{dc} or S_{c1} equal zero), $|A_{1,d}|$ equals $S_{d1}S_{cc}$, and this term becomes a constant term S_{d1}, equivalent to the two-port case S_{21}. In general, the gain term will have a maximum value that will be a function of Γ_L^c i.e. the impedance which is connected at the common-mode port. Let's name the gain term as g_t

$$g_t = \left|\frac{S_{d1} - |A_{1,d}|\Gamma_L^c}{1 - S_{cc}\Gamma_L^c}\right|^2. \tag{6.8}$$

As it can be seen, g_t is a bilinear transformation. As it is demonstrated in Appendix B, (6.8) is an holomorphic function and it satisfies the *maximum modulus principle*. Thereby, the maximum of g_t is obtained for a value of Γ_L^c which satisfies the relation $|\Gamma_L^c| = 1$ or equivalently, when a pure reactance is connected in the common-mode node. However, as it is mentioned in Appendix B, the *maximum modulus principle* does not provide the optimum phase of Γ_L^c and it has to be found by geometrical means.

Therefore, from (6.8), (A.7) and (A.10), G_0 and R_0 are given by

$$G_0 = S_{d1} + \frac{S_{dc}S_{c1}S_{cc}^*}{1-|S_{cc}|^2}, \;\; R_0 = \frac{|S_{dc}S_{c1}|}{\left|1-|S_{cc}|^2\right|} \tag{6.9}$$

Once, G_0 and R_0 are found, the maximum gain is given by

$$|G_{max}| = |G_0| + R_0, \;\; \phi\left(G_0\right) = tan^{-1}\left(\frac{Im\{G_0\}}{Re\{G_0\}}\right) \tag{6.10}$$

Once G_{max} is obtained as $|G_{max}|\,e^{j\phi(G_{max})}$, it can be replaced in the inverse transformation

$$\Gamma_{L,max}^c = \frac{G_{max} - S_{d1}}{S_{cc}G_{max} - \left|A_{1,d}\right|} \tag{6.11}$$

Therefore, when (6.11) is connected to the common-node, g_t reaches the maximum value. Of course a different criteria than the maximum gain can be chosen. The synthesis of a reactance can imply a large inductance at expenses of area cost. In this case, it can be preferable to leave to common-mode port shunted or opened. Also notice that, at the end of the day, common-mode signal is pushed back to differential mode. Thereby, if there is an external common-mode noise source in the system, it is being converted to differential increasing the output noise figure. In this case, the tuning of Γ_L^c if noise is correlated, or simply a Γ_L^c matched, implies that common-mode power will be dismissed or dissipated in Z_L^c instead of appearing at the differential output.

Besides, it can be notice that when the device is symmetric, $|S_{1-c}|$ equals $S_{11}S_{cc}$, $|S_{mm}|$ equals $S_{dd}S_{cc}$, and $|S|$ can be kept as a function of $|S_{1-d}|$; thus, $|S|$ equals $S_{cc}\,|S_{1-d}|$. Replacing these co-factors in G_t

$$G_t = \frac{1-|\Gamma_s|^2}{|1-\Gamma_s\Gamma_1|^2}|S_{d1}|^2\,\frac{1-\left|\Gamma_L^d\right|^2}{\left|1-S_{dd}\Gamma_L^d\right|^2}, \tag{6.12}$$

where

$$\Gamma_1 = \frac{S_{11} - |S_{1-d}|\Gamma_L^d}{1-S_{dd}\Gamma_L^d}. \tag{6.13}$$

As it has been already mentioned, (6.12) and (6.13) are equivalent to the classical two-port device expressions but for submatrix S_{1-d}. Notice that, when the device is symmetric, both expressions are irrespective of the common-mode port as actually, it was expected.

After the choice of Γ_L^c, the key is to achieve the maximum power gain through the choice of source and load impedances. Meanwhile, the stability analysis of the device is conducted. Both of these methods form the foundations of RF amplifier design for traditional two-port devices. These fundamental design methods can be applied to ideal differential circuits by substituting the appropriate mixed-mode S-parameters in the traditional expressions. However, in a real case where the device

is not perfectly symmetric, some correction factors need to be added. Following the traditional development, it was seen in Chapter 3 that, it is expected that maximum power gain occurs when the input and differential output ports are simultaneously conjugate match. As in the two-port theory, the condition of simultaneous conjugate power match is possible only when the device is unconditionally stable. Thereby, applying conjugate power match to the input and the differential output ports, the next relation are obtained

$$\begin{aligned}\Gamma_s^* = \Gamma_1 &= \frac{S_{11} - |S_{1-c}|\,\Gamma_L^c - (|S_{1-d}| - |S|\,\Gamma_L^c)\,\Gamma_L^d}{1 - S_{cc}\Gamma_L^c - (S_{dd} - |S_{mm}|\,\Gamma_L^c)\,\Gamma_L^d} \\ \Gamma_L = \Gamma_d^* &= \left(\frac{S_{dd} - |S_{mm}|\,\Gamma_L^c - (|S_{1-d}| - |S|\,\Gamma_L^c)\,\Gamma_L^1}{1 - S_{cc}\Gamma_L^c - (S_{11} - |S_{1-c}|\,\Gamma_L^c)\,\Gamma_L^1}\right)^* .\end{aligned} \tag{6.14}$$

Reflection coefficients have been properly expressed in order to be able to write them as follows

$$\begin{aligned}\Gamma_s^* = \Gamma_1 &= \frac{a - b\Gamma_L^d}{c - d\Gamma_L^d} = \frac{a/c - b/c\Gamma_L^d}{1 - d/c\Gamma_L^d} = \frac{a' - b'\Gamma_L^d}{1 - d'\Gamma_L^d} \\ \Gamma_L = \Gamma_d^* &= \frac{d^* - b^*\Gamma_1^*}{c^* - a^*\Gamma_1^*} = \frac{d'^* - b'^*\Gamma_s^*}{1 - a'^*\Gamma_s^*}\end{aligned} \tag{6.15}$$

$$\begin{aligned}a &= S_{11} - |S_{1-c}|\,\Gamma_L^c \quad b = |S_{1-d}| - |S|\,\Gamma_L^c \\ c &= 1 - S_{cc}\Gamma_L^c \qquad d = S_{dd} - |S_{mm}|\,\Gamma_L^c\end{aligned} \tag{6.16}$$

Notice that (6.14) depends on Γ_L^c which, as it has been previously mentioned, has to be purely reactive to maximize g_t in (6.3). Also, it is important to notice that (6.15) have been expressed as the two-port equations in Section 1.4.3. Then, equations (1.12)-(1.15) can be used from now.

Substituting Γ_s^* into Γ_L^d, it is possible to demonstrate that

$$\begin{aligned}\Gamma_s &= \frac{1}{2B_1}\left[A_1 \pm \left(A_1^2 - 4\,|B_1|^2\right)^{1/2}\right] \\ \Gamma_L^d &= \frac{1}{2B_2}\left[A_2 \pm \left(A_2^2 - 4\,|B_2|^2\right)^{1/2}\right],\end{aligned} \tag{6.17}$$

where

$$
\begin{aligned}
A_1 &= 1+\left|\frac{a}{c}\right|^2-\left|\frac{d}{c}\right|^2-\left|\frac{b}{c}\right|^2 \\
A_2 &= 1+\left|\frac{d}{c}\right|^2-\left|\frac{a}{c}\right|^2-\left|\frac{b}{c}\right|^2 \\
B_1 &= \frac{a}{c}-\frac{b}{c}\frac{d^*}{c^*} \\
B_2 &= \frac{d}{c}-\frac{b}{c}\frac{a^*}{c^*}.
\end{aligned}
\tag{6.18}
$$

Expressions found are equivalent to the two-port case; however, it is interesting to write them together in order to see the existing correction factors

$$
\begin{aligned}
A_1 &= 1+|S_{11}|^2-|S_{22}|^2-|\Delta|^2 \\
A_1^{mm} &= 1+\left|\frac{S_{11}-|S_{1-c}|\Gamma_L^c}{1-S_{cc}\Gamma_L^c}\right|^2-\left|\frac{S_{dd}-|S_{mm}|\Gamma_L^c}{1-S_{cc}\Gamma_L^c}\right|^2-\left|\frac{S_{1-d}-|S|\Gamma_L^c}{1-S_{cc}\Gamma_L^c}\right|^2 \\
B_1 &= S_{11}-\Delta S_{22}^* \\
B_1^{mm} &= \frac{S_{11}-|S_{1-c}|\Gamma_L^c}{1-S_{cc}\Gamma_L^c}-\frac{|S_{1-d}|-|S|\Gamma_L^c}{1-S_{cc}\Gamma_L^c}\left[\frac{S_{dd}-|S_{mm}|\Gamma_L^c}{1-S_{cc}\Gamma_L^c}\right]^*.
\end{aligned}
\tag{6.19}
$$

where the new expressions have been identified by the superscript *mm*. Notice that expressions found perfectly match the two-port expressions but for a correction factor which is mostly related with how power is reflected back with the common-mode port. Likewise, most of the properties that can be demonstrated for a two-port device, also apply to our case since expressions are equivalent. Thus, we won't analyze the whole theory since it is equivalent to the two-port theory [11]. However, it is interesting to analyze some of most relevant points. Thereby, it is well known that the sign in (6.17) must be chosen in order to accomplish stability conditions i.e. $\Gamma_1 \leq 1$ and $\Gamma_d \leq 1$. Thus, it can be seen that for an absolutely stable device the next condition is required $|A_2| > 2|B_2|$. It is this condition which leads to the choice of sign to be used in (6.17) and to the stability factor, K, that now reads as follows

$$K=\frac{1-\left|\dfrac{S_{11}-|S_{1-c}|\Gamma_L^c}{1-S_{cc}\Gamma_L^c}\right|^2-\left|\dfrac{S_{dd}-|S_{mm}|\Gamma_L^c}{1-S_{cc}\Gamma_L^c}\right|^2+\left|\dfrac{|S_{1-d}|-|S|\Gamma_L^c}{1-S_{cc}\Gamma_L^c}\right|^2}{2\left|\dfrac{S_{11}-|S_{1-c}|\Gamma_L^c}{1-S_{cc}\Gamma_L^c}\dfrac{S_{dd}-|S_{mm}|\Gamma_L^c}{1-S_{cc}\Gamma_L^c}-\dfrac{S_{1-d}-|S|\Gamma_L^c}{1-S_{cc}\Gamma_L^c}\right|}>1. \quad (6.20)$$

In order to define stability circles, stability conditions $\Gamma_1 \leq 1$ and $\Gamma_d \leq 1$ have to be developed. Thus, from (6.15), it can be written

$$\begin{aligned}|\Gamma_1|&=\left|\frac{a/c-b/c\Gamma_L^d}{1-d/c\Gamma_L^d}\right|<1 \text{ for all } \left|\Gamma_L^d\right|<1\\ |\Gamma_d|&=\left|\frac{d/c-b/c\Gamma_1}{1-a/c\Gamma_1}\right|<1 \text{ for all } |\Gamma_s|<1.\end{aligned} \quad (6.21)$$

When these conditions hold, conjugate impedance matching can be used. In general, we find that $|\Gamma_1|<1$ for only a restricted set of values for Γ_L^d and $|\Gamma_d|<1$ for only a restricted set of values for the source impedance Z_s. In this circumstances the device is said to be conditionally stable. Then, values of Γ_L^d that result in $|\Gamma_1|<1$ are called stable ones. The corresponding region of the Smith chart is the stable region. The boundary between stables values of Γ_L^d and unstable one is the circle in the Γ_L^d plane that correspond to the mapping of the circle $|\Gamma_1|<1$ in the Γ_1 plane. From (6.15), we can write the bilineal transformation

$$\Gamma_1=\frac{b/c\Gamma_L^d-a/c}{d/c\Gamma_L^d-1}. \quad (6.22)$$

It corresponds to a circle which center and radius that read as follows

$$\begin{aligned}\Gamma_{LC}^d&=\frac{\dfrac{S_{11}-|S_{1-c}|\Gamma_L^c}{1-S_{cc}\Gamma_L^c}\left(\dfrac{|S_{1-d}|-|S|\Gamma_L^c}{1-S_{cc}\Gamma_L^c}\right)^*-\left(\dfrac{S_{dd}-|S_{mm}|\Gamma_L^c}{1-S_{cc}\Gamma_L^c}\right)^*}{\left|\dfrac{|S_{1-d}|-|S|\Gamma_L^c}{1-S_{cc}\Gamma_L^c}\right|^2-\left|\dfrac{S_{dd}-|S_{mm}|\Gamma_L^c}{1-S_{cc}\Gamma_L^c}\right|^2}\\ R_{LC}^d&=\frac{\left|\dfrac{|S_{1-d}|-|S|\Gamma_L^c}{1-S_{cc}\Gamma_L^c}-\dfrac{S_{11}-|S_{1-c}|\Gamma_L^c}{1-S_{cc}\Gamma_L^c}\dfrac{S_{dd}-|S_{mm}|\Gamma_L^c}{1-S_{cc}\Gamma_L^c}\right|}{\left|\dfrac{|S_{1-d}|-|S|\Gamma_L^c}{1-S_{cc}\Gamma_L^c}\right|^2-\left|\dfrac{S_{dd}-|S_{mm}|\Gamma_L^c}{1-S_{cc}\Gamma_L^c}\right|^2}\end{aligned} \quad (6.23)$$

The source stability circle is the circle of source reflection coefficient Γ_s values that make $|\Gamma_d|$ equals to one. By direct analogy with the derivation of (6.24), it can be found that the center for the source stability circle in the Γ_s plane is given by

$$\begin{aligned}
\Gamma_{SC}^1 &= \frac{\dfrac{S_{dd}-|S_{mm}|\Gamma_L^c}{1-S_{cc}\Gamma_L^c}\left(\dfrac{|S_{1-d}|-|S|\Gamma_L^c}{1-S_{cc}\Gamma_L^c}\right)^* - \left(\dfrac{S_{11}-|S_{1-c}|\Gamma_L^c}{1-S_{cc}\Gamma_L^c}\right)^*}{\left|\dfrac{|S_{1-d}|-|S|\Gamma_L^c}{1-S_{cc}\Gamma_L^c}\right|^2 - \left|\dfrac{S_{11}-|S_{1-d}|\Gamma_L^c}{1-S_{cc}\Gamma_L^c}\right|^2} \\
R_{SC}^1 &= \frac{\left|\dfrac{|S_{1-d}|-|S|\Gamma_L^c}{1-S_{cc}\Gamma_L^c} - \dfrac{S_{11}-|S_{1-c}|\Gamma_L^c}{1-S_{cc}\Gamma_L^c}\dfrac{S_{dd}-|S_{mm}|\Gamma_L^c}{1-S_{cc}\Gamma_L^c}\right|}{\left|\dfrac{|S_{1-d}|-|S|\Gamma_L^c}{1-S_{cc}\Gamma_L^c}\right|^2 - \left|\dfrac{S_{11}-|S_{1-d}|\Gamma_L^c}{1-S_{cc}\Gamma_L^c}\right|^2}.
\end{aligned} \tag{6.24}$$

At this point constant power gain circles can also be obtained. Thus, remember that, transducer power gain is not the only interesting gain definition. As it was shown in Section 1.4.3, power gain G_p defined as in (1.6) leads to power gain circles. Unlike transducer power gain, G_p is defined as the power delivered in the load against power going into amplifier input. Thereby, if Fig. 6.4 is represented as Fig. 3.5 where Γ_d is replaced with Γ_1 and it represents the input reflection coefficient of the three-port device (6.4), the power going into the amplifier can be easily found by simply inspection and by means of (3.61). Thus, the signal in nodes b_1 and a_1 are given by

$$\frac{b_1}{b_s} = \frac{1}{1-\Gamma_1\Gamma_S} \tag{6.25}$$

and

$$\frac{a_1}{b_s} = \frac{\Gamma_1}{1-\Gamma_1\Gamma_S}. \tag{6.26}$$

Once b_1 and a_1 are obtained, it is possible to calculate the power into the amplifier

$$P_{in} = \left|\frac{a_1}{b_s}\right|^2 - \left|\frac{b_1}{b_s}\right|^2 = \frac{\left(1-|\Gamma_{in}|^2\right)}{|1-\Gamma_{in}\Gamma_S|^2}. \tag{6.27}$$

Then, from (6.1), power gain reads as following

$$G_p = \frac{P_{del}}{P_{in}} = \frac{\left(1-\left|\Gamma_L^d\right|^2\right)}{\left(1-|\Gamma_1|^2\right)\left|1-\Gamma_d'\Gamma_L^d\right|^2}\left|\frac{S_{d1}-\left|A_{1,d}\right|\Gamma_L^c}{1-S_{cc}\Gamma_L^c}\right|^2. \tag{6.28}$$

Replacing Γ_1 expressed as in (6.22), into (6.28), the term $1-|\Gamma_1|^2$ is given by

$$1-|\Gamma_1|^2=\frac{\left|1-d/c\Gamma_L^d\right|^2-\left|a/c-b/c\Gamma_L^d\right|^2}{\left|1-d/c\Gamma_L^d\right|^2}. \tag{6.29}$$

Therefore, if one realizes from (6.16) that the coefficient d/c equals Γ' i.e.

$$d/c=\frac{S_{dd}-|S_{mm}|\Gamma_L^c}{1-S_{cc}\Gamma_L^c}=\Gamma', \tag{6.30}$$

G_p results as follows

$$G_p=\frac{\left(1-\left|\Gamma_L^d\right|^2\right)}{\left(\left|1-\frac{d}{c}\Gamma_L^d\right|^2-\left|\frac{a}{c}-\frac{b}{c}\Gamma_L^d\right|^2\right)}\left|\frac{S_{d1}-\left|A_{1,d}\right|\Gamma_L^c}{1-S_{cc}\Gamma_L^c}\right|^2. \tag{6.31}$$

Term $\left|1-d/c\Gamma_L^d\right|^2$ can be written as $\left(1-d/c\Gamma_L^d\right)\left(1-d^*/c^*\left(\Gamma_L^d\right)^*\right)$, and similar $\left|a/c-b/c\Gamma_L^d\right|^2$ to obtain after some algebra G_p as

$$G_p=\frac{\left(1-\left|\Gamma_L^d\right|^2\right)}{1-\left|\frac{a}{c}\right|^2+\left|\Gamma_L^d\right|^2\left(\left|\frac{d}{c}\right|^2-\left|\frac{b}{c}\right|^2\right)-2Re\left\{\Gamma_L^d\left(\frac{d}{c}-\frac{b}{c}\frac{a^*}{c^*}\right)\right\}}\left|\frac{S_{d1}-\left|A_{1,d}\right|\Gamma_L^c}{1-S_{cc}\Gamma_L^c}\right|^2. \tag{6.32}$$

Defining the normalized power gain $\mathscr{G}_t$ as G_p/g_t and after writing $\left|\Gamma_L^d\right|^2$ as $\Gamma_L^d\left(\Gamma_L^d\right)^*$ and $2Re\{Z\}$ as $Z+Z^*$, power gain circles can be written as

$$\Gamma_L^d\left(\Gamma_L^d\right)^*-\left[\frac{\mathscr{G}_p\left(\frac{d}{c}-\frac{b}{c}\frac{a^*}{c^*}\right)\Gamma_L^d+\mathscr{G}_p\left(\frac{d^*}{c^*}-\frac{b^*}{c^*}\frac{a}{c}\right)\left(\Gamma_L^d\right)^*-\left(1-\left|\frac{a}{c}\right|^2\right)\mathscr{G}_p+1}{\left(\left|\frac{d}{c}\right|^2-\left|\frac{b}{c}\right|^2\right)\mathscr{G}_p+1}\right]=0 \tag{6.33}$$

At this point, (6.33) can be easily recognize as a circle in plane Γ_L^d, where center and radius are given by the next expressions

$$\Gamma_{L\mathscr{G}_p} = \frac{\left(\frac{d^*}{c^*} - \frac{b^* a}{c^* c}\right)\mathscr{G}_p}{\left(\left|\frac{d}{c}\right|^2 - \left|\frac{b}{c}\right|^2\right)\mathscr{G}_p + 1}$$

$$R_{L\mathscr{G}_p} = \frac{\left(1 - 2K\mathscr{G}_p\left|\frac{ad}{cc} - \frac{b}{c}\right| + \mathscr{G}_p^2\left|\frac{ad}{cc} - \frac{b}{c}\right|^2\right)^{1/2}}{\left|\left(\left|\frac{d}{c}\right|^2 - \left|\frac{b}{c}\right|^2\right)\mathscr{G}_p + 1\right|} \tag{6.34}$$

All these expressions can be introduced in a circuit simulator. In our case, a template has been generated for Advance Design System from Agilent.

Even though, expressions found are the fundamental theory for the power match of a device, as most of the time, a direct translation to circuit parameters is difficult and sometimes impossible. Therefore, most of designer's work consists on finding out which circuit parameters relate to the expressions found.

6.3 First stage: single-ended LNA

The key point in the design of a LNA consists in the determination of suitable trade-offs between the different circuit specs such as NF, gain, linearity, impedance matching,and power dissipation. Over the years, there have appeared several design techniques for optimizing such trade-offs. To name a few representatives, one can find the classical noise matching (CNM) technique, the simultaneous noise and input matching (SNIM) at any specified amount of power dissipation technique, the power-constrained noise optimization (PCNO) technique, and the PCSNIM technique [12].

For the design of the first stage, the PCSNIM has been selected. The PCSNIM basically consist in SNIM, but the topology includes a feedback capacitor C_d in addition to the well-known source degeneration inductor L_S. This is shown in Fig. 6.5 where a folded cascode topology is presented in detail. The inclusion of the feedback capacitor adds a new degree of freedom that allows the inclusion of the power constraint in the design. As it has been reported in [12], the LNA performance parameters are given by

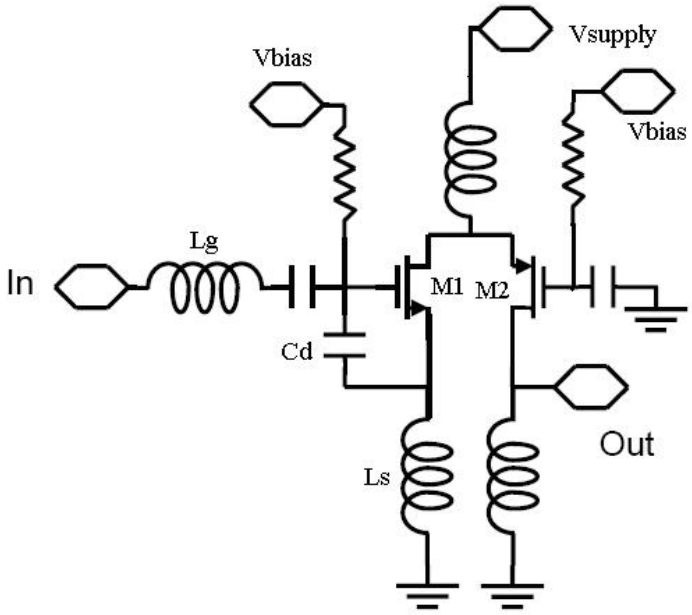

Fig. 6.5 Schematic of a Folded Cascode LNA adapted to apply PCSNIM technique.

$$Z_{opt} = \frac{\alpha\sqrt{\frac{\delta}{5\gamma\left(1-|c|^2\right)}} + \left(j\frac{C_t}{C_{gs}} + \alpha\,|c|\sqrt{\frac{\delta}{5\gamma}}\right)}{\omega C_{gs}\left(\frac{\alpha^2\delta}{5\gamma\left(1-|c|^2\right)} + \left(\frac{C_t}{C_{gs}} + \alpha\,|c|\sqrt{\frac{\delta}{5\gamma}}\right)^2\right)} - sL_s \tag{6.35}$$

$$F_{min} = 1 + \frac{2\omega\sqrt{\gamma\delta\left(1-|c|^2\right)}}{\omega_T\sqrt{5}} \tag{6.36}$$

$$Z_{in} = sL_s + \frac{1}{sC_t} + \frac{g_m L_s}{C_t} \tag{6.37}$$

And the condition that allows Simultaneous Noise and Input Matching is

$$Z_{opt} = Z_{in}^* \tag{6.38}$$

From (6.35), (6.36) and (6.37), the conditions that satisfy (6.38) and the matching with the source impedance are as follows

$$Re\left[Z_{opt}\right] = Re\left[Z_S\right] \tag{6.39}$$

$$Im[Z_{opt}] = Im[Z_S] \tag{6.40}$$

$$Re[Z_{in}] = Re[Z_S] \tag{6.41}$$

All the parameter definitions are summarized in Table 6.2.

Table 6.2 Parameter definitions.

Parameter name	Definition
Z_{opt}	Optimum noise impedance
F_{min}	Minimum noise factor
Z_{in}	Input impedance
ω_T	Cut-off frequency
g_m	Transconductance
C_{gs}	Gate-source capacitance
C_t	$C_{gs} + C_d$
α	$\frac{g_m}{g_{d0}}$
g_{d0}	Drain-source conductance
γ	Experimental parameter related to the channel thermal noise current, for short-channel transistors it can be greater than 2
δ	Experimental parameter related to the channel noise current. For short-channel transistors it can be greater than 2
C	Noise correlation coefficient

The design parameters that can make (6.39), (6.40), (6.41) to be satisfied simultaneously are: V_{GS}, W_1 the width of $M1$, L_S, and C_d. Since there are three equations and four unknowns, (6.39), (6.40) and (6.41) can be solved for an arbitrary value by fixing the value of one of the design parameters. Therefore, in the PCSNIM LNA design technique, by the addition of an extra capacitor, the SNIM can be achieved at any level of power dissipation. The optimization is limited by the input impedance prescript. In order to adapt to the desired impedance, it is necessary to add and input inductance L_g. The qualitative description of the PCSNIM design process would be as follows

1. Choose the transistor size W_1 and V_{GS1} based on the power constraint P_D and minimum noise figure F_{min}.
2. Choose the additional capacitance C_d, as well as the degeneration inductance L_S to satisfy (6.39) and (6.40) simultaneously. The value of C_d should be selected considering the compromise between the size of L_S and the available power gain. Too much L_S can lead to the increase in NF_{min}, while large C_d leads to the gain reduction due to the degradation of the effective cutoff frequency of the composite transistor (transistor including C_d).

3. If there exists any mismatch between Z_{in} and Z_s^*, L_g is selected to provide impedance matching. The different components values that allow a PCSNIM are also limited by inductors size.

If the inductors area exceeds the expected values, it is necessary to relax the gain, noise and power constraints. Furthermore, due to the folded cascode capacity to diminish the supply voltage, the folding of the common-gate transistor helps to extend the cutoff frequency of the common-source transistor. Moreover, the parasitic capacitance at the drain node of the common-source transistor can easily be eliminated by the resonance with the RF choke inductor. In Fig. 6.5, the size of M_1 is 800 µm and M_2 is 280 µm. Selecting a V_{GS} of 0.65 V, the current for this LNA stage is of 2.96 mA, from a supply voltage of 1.5 V. The value of the degeneration inductor is 3 nH. In order to adapt the impedance input to the antenna impedance of 50 Ω, L_g is designed with a value of 25 nH.

The inductor quality factor Q represents an important characteristic that directly effects LNA power and noise performance. For instance, when it is used to match different stages or to degenerate a transistor, it adds actually a voltage noise source to the node where the inductor is connected with a value proportional to 1/Q. In the case of a RF choke or load, the inductor is designed to resonate out; therefore, the Q affects directly to the maximum allowable impedance. To illustrate these cases, Fig. 6.6 shows, in red,the impedance and quality factor of an optimized layout inductor of 25 nH using a different strip width at each turn [13]. The optimization has been performed using, as a first design step, the synthesis tool developed in Chapter 5. Once, a optimum geometry is found in seconds, it is re-optimized with MoMentum, an EM simulator from Agilent Technologies. In this way, it can be obtained the highest Q in the shortest time. To compare with, impedance and Q of the biggest inductor supplied by the manufacturer, with an inductance of 13 nH, have been traced in blue on the same plot. Additionally, both inductors have been resonated at 868.35 MHz with an ideal capacitance. Improvement obtained using the inductor optimization procedure is easily observed: the impedance at resonance has been boosted by a factor of three. Therefore, for a fixed gain value of the LNA, the solution using the optimized inductor will have a power consumption three times lower than the one using the standard inductor library. Also, Fig. 6.7 shows in red the inductance and quality factor for an inductor of 3 nH optimized to obtain the maximum quality factor at 868.35 MHz. Meanwhile, the respective inductor provided by the foundry is represented in blue. The synthesis process by means of the tools developed in Part II and an EM simulator allows to improve the desired characteristics of the passive component and to obtain larger values than the provided by the foundry. Specially in this case, where the foundry provides an inductance library with a maximum value of 13.3 nH that at 868.35 MHz can sometimes be short.

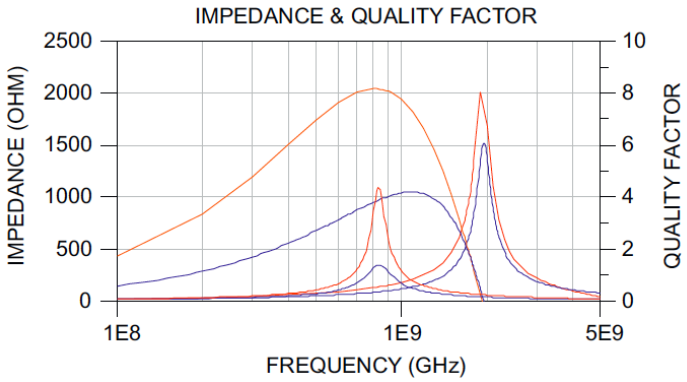

Fig. 6.6 In red, impedance and quality factor synthesized with Part II tools and MoMentum for a 25 nH inductance. In blue, impedance and quality factor for the maximum inductor available in technology Hit Kit, 13 nH.

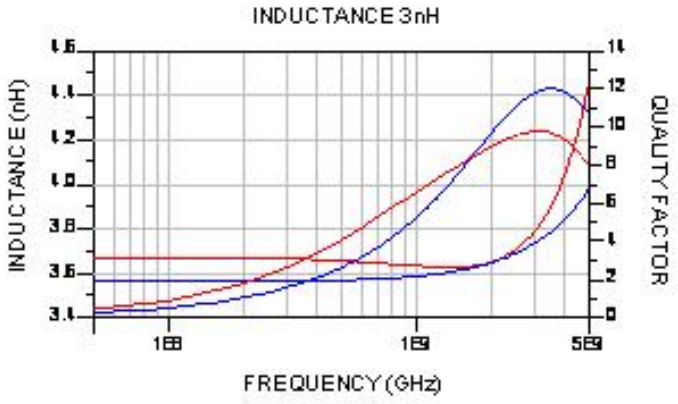

Fig. 6.7 In red, inductance and quality factor a 3 nH inductance available in technology Hit Kit. In blue, inductance and quality factor for a 3 nH synthesized with Part II tools and MoMentum.

6.4 Second stage: design of an active BalUn

In conventional CMOS receiver architectures, the conversion of the single-ended signal from the antenna to a differential signal at the input of LNA is performed by means of an off-chip passive BalUn. The disadvantage of this scheme is that the overall receiver NF is degraded by the insertion loss of the BalUn. In addition, the cost of the receiver grows due to the need of an extra off chip component. An alternative to this solution is to implement the conversion using an integrated active BalUn. This option provides an additional gain to LNA, desensitizing the overall NF of the system with respect to the NF of the next stages. Furthermore, by means

of the active BalUn, the matching of the gain in the differential branches and the phase unbalance over a larger bandwidth are enhanced compared to passive structures. Seeing the different advantages of an active BalUn compared with a passive one, the second stage of the proposed LNA is formed by a differential cascode configuration, where the input signal is copied from one branch to the other through a bypass capacitor as can be seen in Fig. 6.8. Thus, the feedback circuit consists on the components R_1 and C_F. The resistor R_1 plays two roles: it keeps DC bias of $M4$, while it senses the signal feedback from $M3$ drain. Likewise, C_F provides a DC blocking function and copies the RF signal [14].

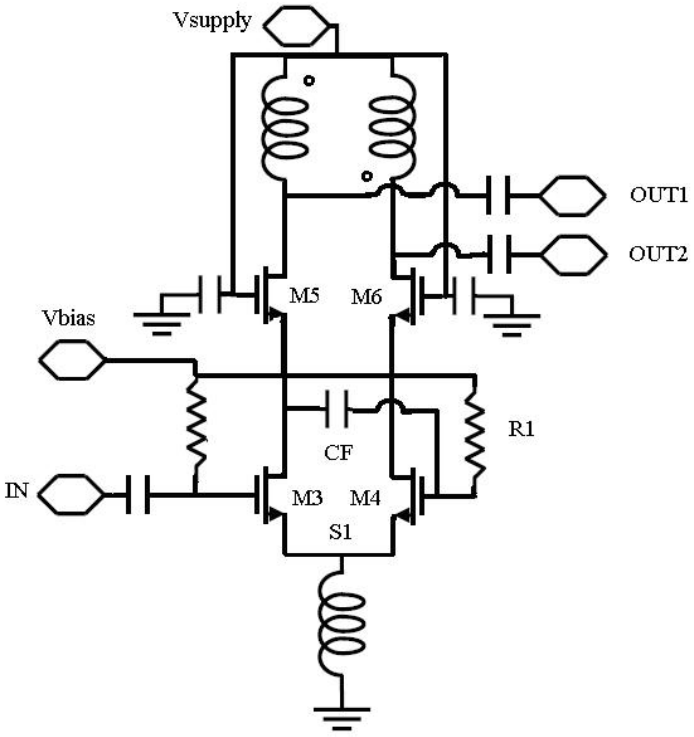

Fig. 6.8 Schematic of the active BalUn.

Ideally, this circuit provides equal amplitude (or gain) and 180° phase difference. However, due to the finite impedance at node S_1 caused by parasitics at high frequency, the gain matching and phase balanced are degraded. In this kind of topologies, an active device is often used as a current source, however the voltage drop across the drain and source makes it difficult to implement at low power supply. For that reason, the active current source has been replaced by an inductor to increase the impedance of node S_1 at the desired high frequencies. Fig. 6.9 shows the im-

provement in the phase balance when an inductor is used compared with a current source.

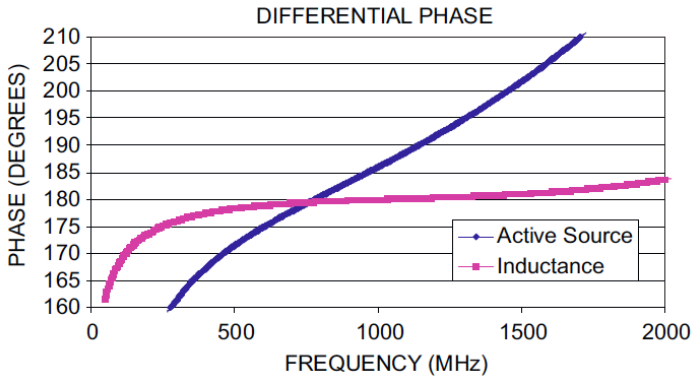

Fig. 6.9 Phase unbalance comparative. In pink when an inductor is used, meanwhile in blue when a tail transistor is used.

The topology represented in Fig. 6.8 requires the use of a differential transformer at the drain of the cascode pair transistors $M5$ and $M6$. The use of a transformer allows to reduce voltage supply and provides a higher impedance than any other passive or active load, specially if it is properly designed to resonate at 868 MHz. Thus, from the differential signal point of view, it generates a large impedance and, at the same time, it presents a notch for common-mode signal. The transformer has been optimized varying the width of each turn [15] using the former layout optimization procedure that has been used for inductors. Summarizing the component used in Fig. 6.8, the size of $M3$ and $M4$ is 1200 µm. Moreover, selecting a V_{GS} of 0.65 V, the current consumption for this LNA stage is 2.71 mA drawn from a power supply voltage of 1.5 V. The value for C_F is 1 pF.

Gain and phase imbalance, as well as the final mixed-mode behavior, is strongly dependent on device mismatch and layout symmetry. Thereby, with the intention of reducing any transistor mismatches, common-centroid topologies have been implemented. Therefore, in the design of the folded cascode, a square ABBA configuration has been employed. Furthermore, in the case of the differential pair, the centroid interdigitation shown in Fig. 6.10 has been designed [16]. Likewise, all capacitors, inductors and transformers have been designed keeping symmetry as much as possible. The final implementation is shown in Fig. 6.11. Taking into account both stages and pads, the total die area is 3 mm^2.

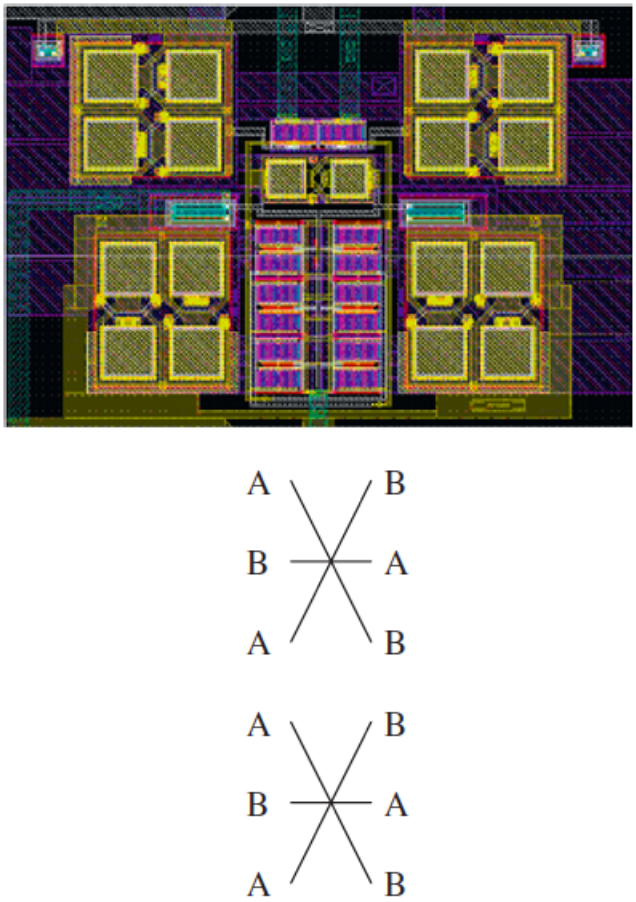

Fig. 6.10 Doubled centroid interdigitation topology for the differential pair in the active BalUn. layout and scheme.

6.5 Experimental results

The LNA has been implemented using a 0.35 μm RFCMOS process from Austrian Micro System. This technology contemplates the possibility of using four metal levels where the top level layer is a quite thick metal of 2.8 μm thickness and 10 mΩ/sq. The circuit is accessed on wafer by using a CASCADE Microtech ACP40-GSG probe for the single-ended input and an ACP40-GSGSG probe for the differential output. Then, a four-port ENA RF network analyzer [17] from Agilent Technologies has been used for the small signal characterization. Notice that, probes have been de-embedded using a three-port SOLT calibration technique with a LRMM differential substrate and home-made calibration files which allows single-ended to differential

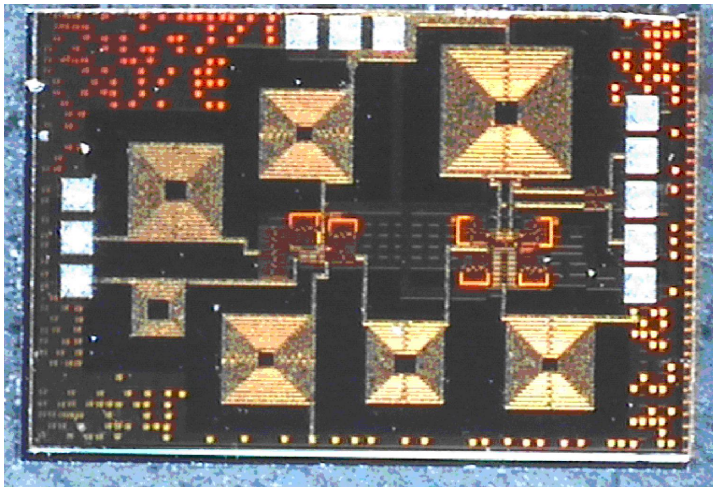

Fig. 6.11 Single-ended-to-differential LNA silicon implementation.

calibration. In addition, test structures (open and short) have been fabricated in order to remove the effect of the pads. It must be kept in mind that, the LNA design has been optimized to be matched with the previous and next transceiver stages which do not match instrumentation source and load impedances, i.e. 50 Ω.

With the referred set-up, a single-ended to differential gain of 21 dB has been measured and represented with the simulated gain in Fig. 6.12, while dissipating 5.8 mA from a 1.5 V voltage supply. Notice that the simulated gain is 1 dB lower than the measured one. This is due to the fact that, the actual quality factor of the fabricated inductors and transformers are better than the simulated ones. It is a common practice that foundries grow thicker top metal layers to assure expectations.

In Fig. 6.13, the measured difference of the phase between the two output branches has been plotted from 650 to 950 MHz showing an excellent performance of $180^{\circ} \pm 1^{\circ}$in the whole frequency range.

One of the main features of the proposed circuit is the rejection of the common-mode signal at the output. Thanks to the active BalUn high symmetry, a differential broad band response is assured at the output meanwhile, there an effective rejection of the common-mode. In this kind of structure, the CMRR can be defined as the differential gain S_{d2P1} divided by common-mode gain S_{c2P1}, and it represents a signal level unbalance. As shown in Fig. 6.14, a CMRR of -33 dB has been measured. Notice that measure shows a weird behavior at the minimum value. The reason can come from the difficulty on an accurate calibration to measure the very low level of common-mode signal. It has to be note that simulation shows a rejection of almost 50 dB between S_{d2P1} gain and S_{c2P1}.

In order to measure Noise Figure, a HP8970B noise figure meter has been used. Since, noise figure meter is a single-ended equipment, LNA differential output has to be transformed to single-ended. For this purpose, a rat-race circuit has been de-

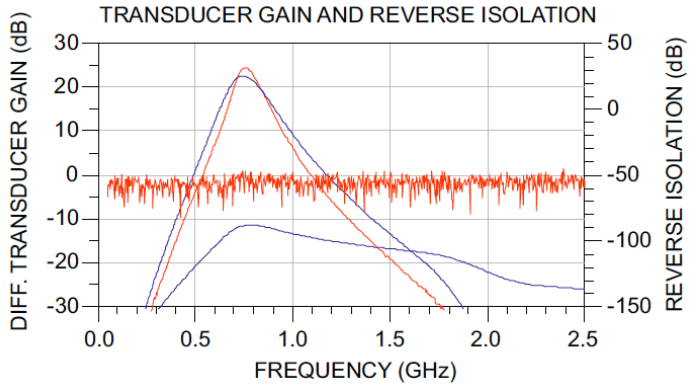

Fig. 6.12 Differential transducer power gain and reverse isolation. Measure is in red and simulation is in blue.

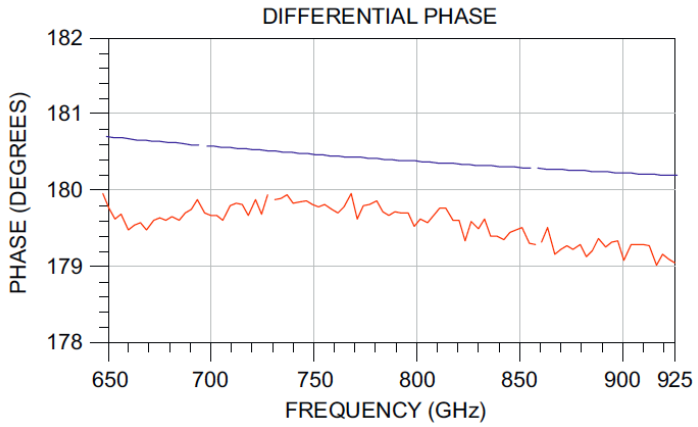

Fig. 6.13 Differential Phase. Measure in red and Simulation in blue.

signed and fabricated in a PCB technology. Noise of this component is theoretically calculated based on its measured losses. Finally, LNA NF is calculated based on Friis' noise figure equation. Fig. 6.15 shows the simulated and measured Noise Figure over 50 Ω. At the frequency of interest, the NF measured is 5.0 dB, whereas the simulated one is 4.7 dB. Even though, there are lower NF reported values, as shown in Table 6.3, such designs do not include the input gate matching inductor integrated on chip.

The non-linear behavior of the LNA has been characterized through the measurements of the 1 dB-compression point (P1dB) and the third order input referred interception point (IIP3). Keeping in mind that the IEEE802.15.4 establishes only one channel in the European 868 MHz band, the 1 dB-CP represents a better figure of merit. Both outputs of the LNA have been combined out of chip by means of a

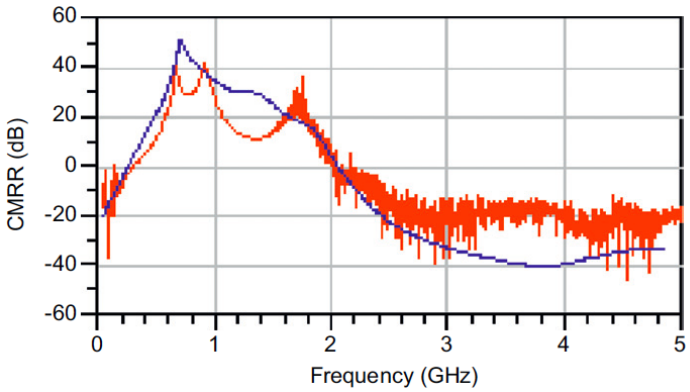

Fig. 6.14 CMRR Common-Mode Rejection Ratio. Measure in red and Simulation in blue.

Table 6.3 Performance comparison for 900MHz LNAs in CMOS technology.

Quantity	[18]	[19]	[12]	This work
GAIN (dB)	20	17.5	12	21
NF (dB)	3.2	2	1.35	4.3
S_{11} (dB)	-12	-10	-18	-9.5
S_{22} (dB)	n.a.	-15	n.a.	-9.8
1dB-CP (dBm)	-4	-15	-15	-9.5
IIP3 (dBm)	8	-6	-4	-3.0
Power Dissipation (mW)	27	22	2	9

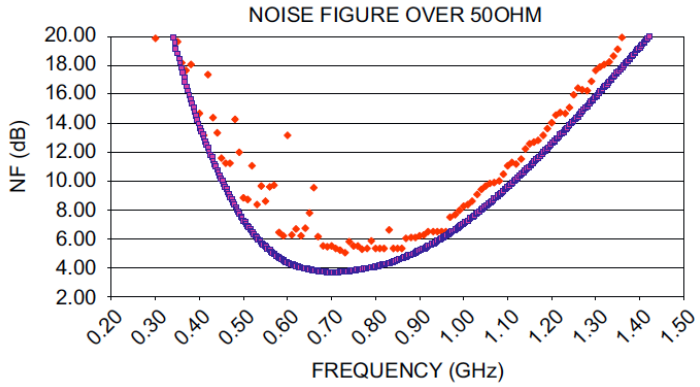

Fig. 6.15 Noise Figure measured and simulated over 50Ω. Measure in red and Simulation in blue.

rat-race device. Fig. 6.16 shows the obtained result. At a value of -9.5 dBm of the input power, the differential gain falls by 1 dB. For measuring the IIP3 value, two signals have been combined using one hybrid coupler at the input of the LNA. The signals have been separated 1 MHz in frequency. At the same time, both outputs of

the LNA have been combined in a single-ended signal. Fig. 6.17 shows a measured IIP3 value of -3 dBm. Theoretically, an IIP3 value 9 dB greater than 1dB-CP value is expected.

In order to summarize the resulting performance of the proposed LNA, Table 6.3 shows a comparison with other state-of-the-art 900 MHz LNAs in CMOS technologies. Notice that this work is the only one which provides a complete monolithic solution, integrating all inductors on chip. For equivalent gain and IIP3 conditions in [18, 19], the power consumption has been reduced by half due to the use of optimized inductors, while still keeping a good noise performance. Although [12] shows a lower NF and power consumption, it must be kept in mind that only the source degeneration inductor has been integrated; consequently the LNA performance depends mainly on the external components.

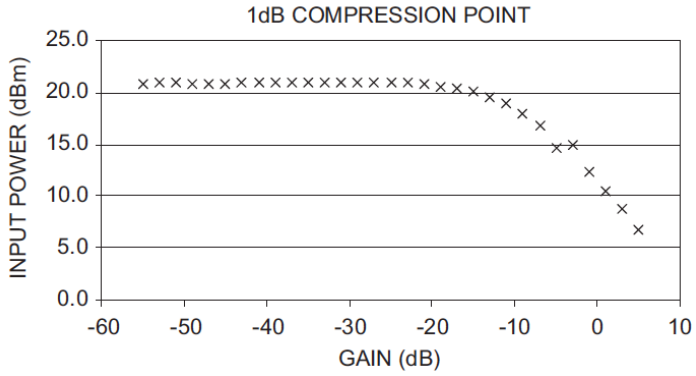

Fig. 6.16 Compression Point -1dB.

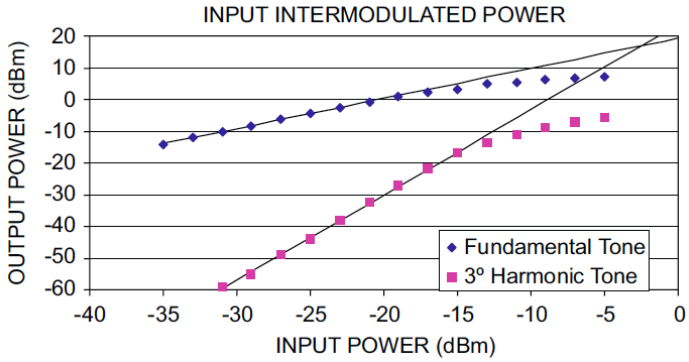

Fig. 6.17 IIP3 measured.

6.6 Conclusion

In this work, a low-power single-ended-to-differential LNA for IEEE 802.15.4 application has been implemented in a conventional 0.35 µm RF CMOS process. The LNA has been designed based on a more general re-formulation of the classical S-parameter expressions for the design of RF amplifiers. This theory which extends Bockelman's theory, represents the exact mathematical formalism and it is irrespective of the symmetry of the device. Moreover, in order to enhance LNA performances, the substitution of current mirrors as well as resistive and active loads, by optimized on-chip inductors and transformers has been proposed for the first time. Thereby, it has been proved that the replacement of the current mirrors by optimized inductors allows a supply voltage reduction of $\left(V_{th,nmos} + |V_{th,pmos}|\right)$ value. In addition, the use of optimized load transformers and RF chocks has enabled the decrease of the polarization current by a factor of three for a fixed LNA gain value. Moreover, the behavior of the symmetric inverter transformer as a load in the active BalUn presents a notch for the common-mode signal resulting. Thus, the phase balance is better than 1° in a large frequency range. All these improvements translate to the figures of merit of the designed LNA as follows: a NF of 4.3 dB, power gain of 21 dB, and a balance of $180^\circ \pm 1^\circ$, while dissipating 6 mA from a voltage supply of 1.5 V.

6.7 Acknowledgements

I would like to thank to José Gabriel Macéas and Dr. Ángel Diéguez for their invaluable help. Also, I would like to thank to Agilent Technologies for equipment support. This research was funded by the Spanish Government under project TEC2007-67247-C02-02.

References

1. Tomas Carrasco Carrillo, Jose Gabriel Macias-Montero, Aitor Osorio Marti, Javier Sieiro Cordoba, and Jose Maria Lopez-Villegas. Cmos single-ended-to-differential low-noise amplifier. *Integration, the VLSI Journal*, 42(3):304 – 311, 2009. ¡ce:title¿Special Section on DCIS2006¡/ce:title¿.
2. Behzad Razavi. *Rf Microelectronics*. Prentice Hall, 1998.
3. K.B. Niclas. Noise in broad-band gaas mesfet amplifiers with parallel feedback. *Microwave Theory and Techniques, IEEE Transactions on*, 30(1):63 –70, jan. 1982.
4. J.J. Kucera and U. Lott. Low-power silicon bjt lna for 1.9 ghz. *Microwave and Guided Wave Letters, IEEE*, 8(3):136 –137, mar 1998.
5. C.S. Kim, M. Park, C.H. Kim, H.K. Yu, Yu.K. Lee, D.Y. Kim, and H. Cho. Thick metal cmos technology on high resistivity substrate for monolithic 980 mhz and 1.9 ghz cmos lnas. *IEEE MTT-S Digest*, 2:573 –576 vol.2, 1999.
6. IEEE. *IEEE Std 802.15.1-2002*.

7. J.M. Lopez-Villegas, J. Samitier, C. Cane, P. Losantos, and J. Bausells. Improvement of the quality factor of rf integrated inductors by layout optimization. *Microwave Theory and Techniques, IEEE Transactions on*, 48(1):76 –83, jan 2000.
8. J.J. Zhou and D.J. Allstot. Monolithic transformers and their application in a differential cmos rf low-noise amplifier. *Solid-State Circuits, IEEE Journal of*, 33(12):2020 –2027, dec 1998.
9. M.N. El-Gamal, K.H. Lee, and T.K. Tsang. Very low-voltage (0.8v) cmos receiver frontend for 5 ghz rf applications. *Circuits, Devices and Systems, IEE Proceedings -*, 149(56):355 – 362, oct/dec 2002.
10. H. Ma, S.J. Fang, F. Lin, and H. Nakamura. Novel active differential phase splitters in rfic for wireless applications. *IEEE Trans. Microwaves Theory Tech.*, pages 51 –54, jun 1998.
11. Robert E. Collin. *Foundations for Microwave Engineering*. Wiley-IEEE Press, 2 edition, December 2000.
12. Trung-Kien Nguyen, Chung-Hwan Kim, Gook-Ju Ihm, Moon-Su Yang, and Sang-Gug Lee. Cmos low-noise amplifier design optimization techniques. *Microwave Theory and Techniques, IEEE Transactions on*, 52(5):1433 – 1442, may 2004.
13. Javier Sieiro Cordoba. *Modelling of Integrated Passive Components for RFICs:Application to VCOs Design*. PhD thesis, Universidad de Barcelona, 2001.
14. M.K. Raja, T.T.C. Boon, K.N. Kumar, and Wong Sheng Jau. A fully integrated variable gain 5.75-ghz lna with on chip active balun for wlan. *IEEE Radio Frequency Integrated Circuits Symposium*, pages 439 – 442, june 2003.
15. Josep Cabanillas Costa. *Analysis of Integrated Transformers and Its Application to RFIC Design*. PhD thesis, . Universidad de Barcelona, 2002.
16. Alan Hastins. *The Art of Analog Layout*. Tom Robbins, 2005.
17. Agilent. *On-Wafer Balanced Component Measurement Using the ENA RF Network Analyzer with the Cascade Microtech Probing System*. Agilent. Product Note E5070/71-3.
18. A. Rofougaran, J.Y.-C. Chang, M. Rofougaran, and A.A. Abidi. A 1 ghz cmos rf front-end ic for a direct-conversion wireless receiver. *Solid-State Circuits, IEEE Journal of*, 31(7):880 –889, jul 1996.
19. F. Gatta, E. Sacchi, F. Svelto, P. Vilmercati, and R. Castello. A 2-db noise figure 900-mhz differential cmos lna. *Solid-State Circuits, IEEE Journal of*, 36(10):1444 –1452, oct 2001.

Chapter 7
Conclusions

Scattering parameter theory represents the cornerstone of radio- and micro-wave frequency theory. They are used to characterize the physical and electrical behavior of every linear frequency dependent device. Thereby, S-parameters have been broadly used in fields like electrical engineering, electronics engineering, and communication systems design, and especially for microwave engineering.

Unlike standard S-parameters, mixed-mode S-parameters have been a sensitive issue, easy prey for polemic and misunderstanding. Thereby, in Chapter 2 the theory of mixed-mode scattering parameters has been extended not only to symmetrical devices, but to non-symmetrical or actual devices, finding a general expression for $\Gamma_d(\Gamma_c)$ that resembles the well-known expressions of $\Gamma_{in}(\Gamma_{out})$ for a single-ended two-port device. It has also been shown that the former particular cases of the driving of a two-port device are reduced to the application of a short, open and matched mixed-mode load conditions on the general expression of $\Gamma_d(\Gamma_c)$. Moreover, such definitions allow to obtain $Z_d(Z_c)$ in terms of S_{mm}. An analytic connection between scattering-parameters description in both versions, through the use of S-parameters and S_{mm}, and lumped elements description has naturally been used toward the attainment of these expressions.

Using the correct definitions for $\Gamma_d(\Gamma_c)$, the power match concept has been revisited: *in actual n-port devices having mixed-mode ports, the loading condition of the complementary driven and loaded ports must be reactive, instead of complex conjugate*. This statement should not be a surprise since it is not the device itself but the application that forces the necessary conditions for power match. Strictly speaking, the classical concept of power matching in single-ended amplifier design does not hold for mixed-mode amplifier design. For arriving to this point and based on Kurokawa's and Ferrero-Pirola's works, generalized S-parameters formalism has been extended beyond its current state of the art as well as, for the first time, signal flow graphs and Mason's rules have been applied to the analysis of generalized S-parameters. New low entropic expressions have been developed for the computation of port impedance, port impedance transformation, transducer/available gain power relationships and mismatching circles. It has been also shown that the devel-

oped theory is a super-set of all the current Bockelman's mixed-mode S-parameters theory by applying the convenient symmetry conditions.

Since another of the current RF bottlenecks discussed in Chapter 2.1 is the synthesis of passive components, in Part II a tool for the fast synthesis of planar inductors has been presented. In this way, in Chapter 4, it has been shown the feasibility of an 'ab initio' adaptive meshing technique for planar RF and microwave circuits which is accurate enough to account for the losses in high Q planar devices. The mesh is generated in three steps: (1) assuming a quasi-static magnetic behavior, all inductive coupling terms between metal strips are computed; (2) an estimation of the current crowding phenomena is computed using equation (4.3); (3) the number of cell divisions across the width of a metal strip is assigned accordingly. Additionally, an analytic model of the current crowding phenomena based on circuit parameters has been developed. Complementary, in Chapter 5 a bisection algorithm for the synthesis of compact planar inductors in LTCC technology has been proposed. Thanks to the use of fast EM solvers and heuristic rules a library set of 20 inductors has been obtained in less than 100 seconds.

Finally in Part III, the methods and tools developed in this thesis are used in the analysis of a low-power single-ended-to-differential LNA for IEEE 802.15.4 application implemented in a conventional 0.35 μm RF CMOS process. In order to enhance LNA performance, the substitution of current mirrors as well as resistive and active loads, by optimized on-chip inductors and transformers has been proposed for the first time. Thus, the phase balance is better than 1° in a wide frequency range. All these improvements and the methods and tools developed lead to the next figures of merit of the designed LNA: a NF of 4.3 dB, power gain of 21 dB, a CMRR lower that 30 dB and a phase balance of $180^\circ \pm 1^\circ$, while dissipating 6 mA from supply a voltage of 1.5 V.

Appendix A
Bilinear transformation

A bilinear transformation is a mapping of the complex plane Z into a complex plane G which has the next general expression

$$G = \frac{AZ + B}{CZ + D}, \tag{A.1}$$

where A, B, C, D are also complex numbers. One of the main properties of a bilinear transformation is the fact that, a circle in Z-plane is mapped as a circle in plane G. Likewise, if a straight line is seen as a circle with an infinite radius, it is equally mapped as a circle in plane G. In this property resides the fundamentals of impedance transformation in Smith chart. Thus, consider the case represented in Fig. A.1, where two circles, which are related by (A.1), are represented in the Smith chart.

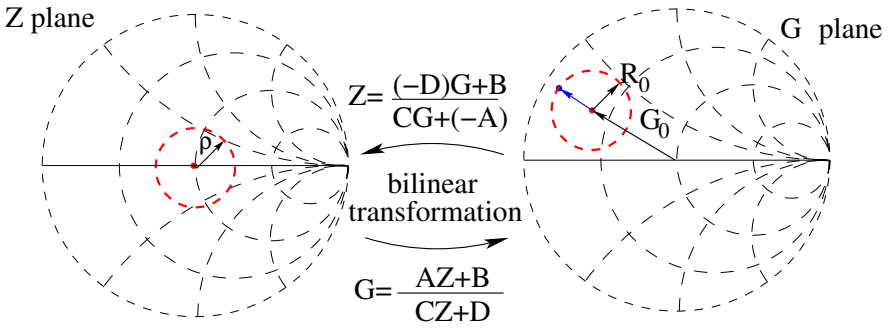

Fig. A.1 Bilinear transformation of a circle from Z-plane to G-plane in Smith chart.

In order to probe the mentioned property, the circle represented in the plane Z is described by the next expression

$$ZZ^* - \rho^2 = 0, \tag{A.2}$$

where ρ is the radius of the circle. By applying the transformation represented in Fig. A.1 to (A.2), the next equality can be written

$$\frac{(-D)\,G+B}{CG+(-A)}\frac{(-D^*)\,G^*+B^*}{C^*G^*+(-A^*)}-\rho^2=0. \tag{A.3}$$

This expression can be developed and arranged, resulting as follows

$$GG^*-\frac{\left(DB^*-\rho^2CA^*\right)}{(DD^*-\rho^2CC^*)}G-\frac{\left(D^*B-\rho^2C^*A\right)}{(DD^*-\rho^2CC^*)}G^*+\frac{BB^*-\rho^2AA^*}{(DD^*-\rho^2CC^*)}=0. \tag{A.4}$$

This expression represents a circle in plane G. Notice that, in general, a circle in plane G is described by the next expression

$$(G-G_0)\,(G^*-G_0^*)-R_0^2=0, \tag{A.5}$$

that can also be developed as follows

$$GG^*-GG_0^*-G_0G^*+G_0G_0^*-R_0^2=0. \tag{A.6}$$

Therefore, by comparison of (A.4) and (A.6), one realizes that effectively, a circle in plane Z is mapped as a circle in plane G. Moreover, it is interesting to obtain the radius R_0, and center position G_0, after the transformation. Thus, straightforward from the comparison, the new center position in plane G is given by

$$G_0=\frac{D^*B-\rho^2AC^*}{DD^*-\rho^2CC^*}. \tag{A.7}$$

In order to find the radius R_0, newly by comparison of the independent terms in (A.4) and (A.6), it can be written the next equality

$$GG_0^*-R_0^2=\frac{BB^*-\rho^2AA^*}{(DD^*-\rho^2CC^*)}, \tag{A.8}$$

which leads to

$$R_0^2=GG_0^*-\frac{BB^*-\rho^2AA^*}{(DD^*-\rho^2CC^*)}. \tag{A.9}$$

Replacing (A.7) into (A.9), and after some algebra, one can write R_0 as follows

$$R_0=\rho\frac{|AD-BC|}{\left||D|^2-\rho^2\,|C|^2\right|} \tag{A.10}$$

Appendix B
Maximum of the modulus of a bilinear transformation

The modulus of bilinear transformations is a reiterative term in gain expressions along this thesis. As instance, in the case of a three-port device, transducer gain depends on the square of the modulus of a bilinear transformation

$$g_t = \left| \frac{S_{d1} - \left|A_{1,d}\right| \Gamma_L^c}{1 - S_{cc}\Gamma_L^c} \right|^2 . \tag{B.1}$$

An interesting property of bilinear functions, that will be demonstrated in this appendix, is that they satisfy the *maximum modulus principle*. By means of this principle, the maximum of the modulus of a bilinear transformation, like (B.1), can be obtained. However, this principle is only applicable to holomorphic functions. Therefore, let demonstrate that a general bilinear transformation is a holomorphic function.

A holomorphic function is a complex-valued function of one or more complex variables that is complex differentiable in a neighborhood of every point in its domain. If a complex function $f(z) = u(x,y) + iv(x,y)$ is holomorphic, then u and v have first partial derivatives with respect to x and y, and satisfy the *Cauchy-Riemann* equations

$$\frac{\partial u}{\partial x} = \frac{\partial v}{\partial y} \; ; \; \frac{\partial u}{\partial y} = -\frac{\partial v}{\partial x}. \tag{B.2}$$

Thereby, consider the general bilinear transformation

$$G = \frac{AZ + B}{CZ + D}. \tag{B.3}$$

By simply inspection, it can be seen that a bilinear transformation has a residue in $z = -D/C$. Thereby, this point has to be removed from the analysis domain. After that, the expression can be simplified if B and D are factorized and the constant factor is neglected, since demonstration is based on derivative calculations. Thus, after renaming, it results as follows

$$G = \frac{aZ+1}{bZ+1} = \frac{a(x+yi)+1}{b(x+yi)+1}. \tag{B.4}$$

The bilinear transformation, G, can be written as $f(z) = u(x,y) + iv(x,y)$, where real and imaginary parts are given by

$$\begin{aligned} u(x,y) &= \frac{(ax+1)(bx+1)}{(bx+1)^2+b^2y^2} + \frac{ay^2b}{(bx+1)^2+b^2y^2} \\ v(x,y) &= \frac{ay(bx+1)}{(bx+1)^2+b^2y^2} - \frac{(ax+1)by}{(bx+1)^2+b^2y^2} \end{aligned} \tag{B.5}$$

.

In order to check if *Cauchy-Riemann* equations are satisfied, partial derivatives are calculated resulting as follows

$$\begin{aligned} \frac{\partial u}{\partial x} &= \frac{ab^2x^2+2abx+a-ab^2y^2-b^3x^2-2b^2x-b+b^3y^2}{(b^2x^2+2bx+1+b^2y^2)^2} \\ \frac{\partial v}{\partial y} &= \frac{ab^2x^2+2abx+a-ab^2y^2-b^3x^2-2b^2x-b+b^3y^2}{(b^2x^2+2bx+1+b^2y^2)^2} \\ \frac{\partial u}{\partial y} &= 2\frac{by\left(abx-b^2x-b+a\right)}{(b^2x^2+2bx+1+b^2y^2)^2} \\ \frac{\partial v}{\partial x} &= -2\frac{by\left(abx-b^2x-b+a\right)}{(b^2x^2+2bx+1+b^2y^2)^2} \end{aligned} \tag{B.6}$$

.

Effectively, from (B.6), it can be easily seen that *Cauchy-Riemann* equations are satisfied and a bilinear function is a holomorphic function in C-domain removing the residue $z = -D/C$.

Once it has been demonstrated that (B.3) is holomorphic, the *maximum modulus principle* is satisfied. Then, the *maximum modulus principle* reads as follows

Theorem B.1. *Let $U \subseteq C$ be a domain, and let f be an analytic function on U. Then if there is a point $z_0 \in U$ such that $|f(z_0)| \geq |f(z)|$ for all $z \in U$, then f is constant. The following slightly sharper version can also be formulated. Let $U \subseteq C$ be a domain, and let f be an analytic function on U. Then if there is a point $z_0 \in U$ at which $|f|$ has a local maximum, then f is constant.*

Furthermore, let $U \subseteq C$ be a bounded domain, and let f be a continuous function on the closed set $\overline{U}$ that is analytic on U. Then the maximum value of $|f|$ on $\overline{U}$ (which always exists) occurs on the boundary δU. In other words,

$$\max_{\overline{U}} |f| = \max_{\delta U} |f|$$

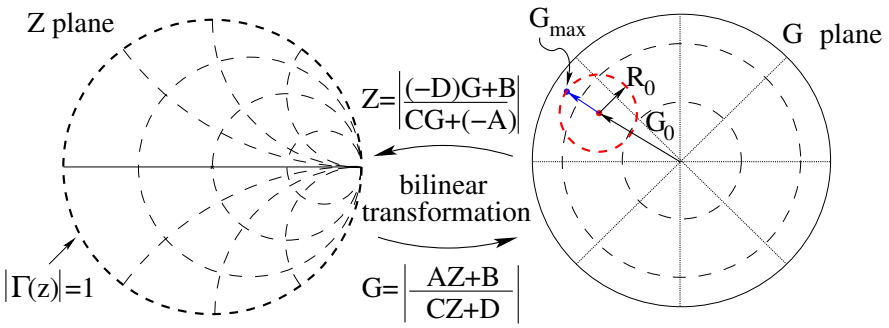

Fig. B.1 Bilinear transformation of a circle from plane Z to plane G in a Smith chart.

Therefore, based on the second part of Theorem B.1, the maximum of

$$G = \left| \frac{AZ+B}{CZ+D} \right|^2, \tag{B.7}$$

when Z is bounded, occurs for a value of Z located precisely on the boundary. This situation is represented in Fig. B.1. The maximum of the modulus of G can only fall on the boundary, at least G is a constant value. Since, a circle is transformed as a circle, the maximum corresponds to a value within a circle in the boundary of variable Z in Z-plane. Therefore, if Z-plane is the impedance plane in Smith chart, the maximum corresponds to a point which satisfy the condition $|\Gamma(Z)|$ equal to one. Unfortunately, Theorem B.1 does not give the phase of Z which results as the maximum. Phase is important, since it can be demonstrated that, the minimum value of the modulus of (B.3) also falls on the boundary. Thereby, the easiest way to obtain the corresponding phase, is by a geometrical approach. From Fig. B.1, it can be seen that the maximum modulus correspond to the point named as G_{max}. Since, (B.3) is a bilinear transformation, the center and radius of the corresponding circle in plane G are given by expression in Appendix A i.e. (A.7) and (A.10). Therefore, the maximum G_{max} is given by

$$|G_{max}| = |G_0| + R_0, \quad \phi(G_{max}) = tan^{-1}\left(\frac{Im\{G_0\}}{Re\{G_0\}} \right). \tag{B.8}$$

Once G_{max} is obtained as $|G_{max}| e^{j\phi(G_{max})}$, it can be replaced in the inverse transformation and Z_{max} results as follows

$$Z_{max} = \frac{(-D)G_{max}+B}{CG_{max}+(-A)}. \tag{B.9}$$